NATIONAL TECHNICAL UNIVERSITY OF ATHENS
SCHOOL OF RURAL, SURVEYING & GEOINFORMATICS ENGINEERING
Remote Sensing Laboratory

TIME SERIES METHODS FOR SYNTHETIC APERTURE RADAR DATA TO MONITOR GROUND DEFORMATION, SOIL MOISTURE AND FLOODWATER

Doctoral Dissertation

Kleanthis Karamvasis

Supervisor: Prof. Vassilia Karathanassi

Athens, December 2022

ΕΘΝΙΚΟ ΜΕΤΣΟΒΙΟ ΠΟΛΥΤΕΧΝΕΙΟ
ΣΧΟΛΗ ΑΓΡΟΝΟΜΩΝ & ΤΟΠΟΓΡΑΦΩΝ ΜΗΧΑΝΙΚΩΝ –
ΜΗΧΑΝΙΚΩΝ ΓΕΩΠΛΗΡΟΦΟΡΙΚΗΣ
Εργαστήριο Τηλεπισκόπησης

ΜΕΘΟΔΟΙ ΑΝΑΛΥΣΗΣ ΧΡΟΝΟΣΕΙΡΩΝ ΔΕΔΟΜΕΝΩΝ ΡΑΝΤΑΡ ΣΥΝΘΕΤΙΚΟΥ ΑΝΟΙΓΜΑΤΟΣ ΓΙΑ ΤΗΝ ΠΑΡΑΚΟΛΟΥΘΗΣΗ ΕΔΑΦΙΚΩΝ ΠΑΡΑΜΟΡΦΩΣΕΩΝ, ΕΔΑΦΙΚΗΣ ΥΓΡΑΣΙΑΣ ΚΑΙ ΠΛΗΜΜΥΡΙΣΜΕΝΩΝ ΕΚΤΑΣΕΩΝ

Διδακτορική Διατριβή

Κλεάνθης Καραμβάσης

Επιβλέπουσα: Καθ. Βασιλεία Καραθανάση

Αθήνα, Δεκέμβριος 2022

Committee

Advisory Committee

Vassilia Karathanassi
Professor, National Technical University of Athens, Supervisor

Dimitrios Paradisis
 Professor, National Technical University of Athens

Dimitris Argialas
Professor, National Technical University of Athens

Examination Committee

Vassilia Karathanassi
Professor, National Technical University of Athens, Supervisor

Dimitrios Paradisis
 Professor, National Technical University of Athens

Dimitris Argialas
Professor, National Technical University of Athens

Konstantinos Karantzalos
Associate Professor, National Technical University of Athens

Issaak Parcharidis
Professor, Harokopio University

Ioannis Papoutsis
Researcher, National Observatory of Athens

Panayiotis Frangos
Professor, National Technical University of Athens

Abstract

Climate change is a major challenge of our time. Adapting to climate action is an economic and environmental imperative. In order to enhance our climate resilience, we need to improve our understanding of climate change impacts. Some of the most important impacts are temperature increase, more severe storms, increased drought and warming and increasing ocean. Many of these impacts are interrelated and have many associated causes. An essential need is to better understand the interdependencies between climate change cause/effect variables.

Earth observation data have a unique role for improving understanding of climate change, due to the fact that they enable monitoring at several spatiotemporal scales with global coverage. Remote sensing technology can improve climate change modelling but it also has some limitations. For example, multispectral and hyperspectral sensors can provide data only during the day with no cloud coverage. On the contrary, SAR datasets can provide consistent data flows day and night. The unprecedented increased volume of SAR/InSAR data can enable approaches that can hugely benefit climate change adaptation actions. This dissertation contributes to enhancing the role of time series of SAR/InSAR data for three climate change related topics.

The first topic is the study of TSInSAR methodologies that estimate ground deformations, as well as ground deformation relationships with natural agents. Ground deformation is an essential climate change variable which is connected to a) increasing groundwater extraction due to increasing droughts; b) permafrost thawing due to increasing temperature and c) increased flood/sinking risk over coastal regions. A thorough analysis of several TSInSAR methodologies for ground deformation is presented. First, an accuracy assessment of the vertical component of ground deformation which was estimated from multiple orbit TSInSAR results is presented. Then, a detailed performance analysis of several TSInSAR methodologies is provided. Next, a wavelet-based methodological approach able to capture the relationships between driving factors and ground deformation is developed. Finally, a description of the developed software package (INTERFERON) for ground deformation estimation from InSAR data is provided.

The second topic of this dissertation is the soil moisture estimation from InSAR time series. Soil moisture is an essential climate variable which is mainly used for drought monitoring. Climate change is expected to increase the probability of longer, intense, and frequent droughts over the world. An innovative methodological approach with its open-source implementation (INSAR4SM), able to capture surface soil moisture information over arid regions is introduced. A remarkable accuracy (RSME~0.035 m3/m3) of volumetric surface soil moisture estimations over an arid region in California, USA at high spatial resolution (250 m) was achieved.

The third topic of this dissertation is floodwater mapping and monitoring by exploiting SAR time series data. Flooding is one of the most impacting environmental hazards that causes huge economic damages. Climate change is expected to increase flood events mainly due to extreme precipitation events. A methodological framework for unsupervised floodwater mapping and monitoring using Sentinel-1 time series is proposed. Its robust performance (OA~ 0.97, Kappa score~ 0.77) was demonstrated over several investigated flood cases around the world by the EMS, Copernicus service. An open-source toolbox (FLOMPY) implements the proposed methodological framework and two case studies that utilize FLOMPY`s floodwater maps are presented. The first is related to flood damage assessment on agricultural regions and the second is a sensitivity analysis of a coupled 1D/2D hydrodynamic model. Both case studies

highlighted the FLOMPY`s significant contribution to tackle scientific and socioeconomic issues related to increasing flood events due to climate change.

Εκτεταμένη Περίληψη (Abstract in Greek)

Η κλιματική αλλαγή είναι μια μεγάλη πρόκληση της εποχής μας. Οι δράσεις για την προσαρμογή μας στη κλιματική αλλαγή είναι επιτακτική ανάγκη. Προκειμένου να ενισχύσουμε την ανθεκτικότητα και την προσαρμοστικότητα μας στην κλιματική αλλαγή, πρέπει να κατανοήσουμε σε βάθος τις δυσμενείς επιπτώσεις της στο περιβάλλον και στην οικονομία. Μερικές από τις πιο σημαντικές επιπτώσεις είναι η αύξηση της θερμοκρασίας, τα έντονα καιρικά φαινόμενα (π.χ. καταιγίδες), η αυξημένη ξηρασία και η αύξηση της στάθμης της θάλασσας. Πολλές από αυτές τις επιπτώσεις είναι αλληλένδετες και σχετίζονται με μια πληθώρα παραγόντων. Η έρευνα για την καλύτερη κατανόηση των μηχανισμών, σχέσεων και αλληλεξαρτήσεων μεταξύ των αιτιών και των επιπτώσεων της κλιματικής αλλαγής είναι πλέον ουσιαστική ανάγκη.

Τα δεδομένα παρατήρησης γης παίζουν μοναδικό ρόλο στη βελτίωση της κατανόησης της κλιματικής αλλαγής, διότι επιτρέπουν την συνεχή καταγραφή πληροφορίας σε υψηλές χωρικές αναλύσεις με παγκόσμια κάλυψη. Ενώ η τηλεπισκόπηση μπορεί να βελτιώσει σε μεγάλο βαθμό τη μοντελοποίηση της κλιματικής αλλαγής, έχει ορισμένους περιορισμούς που πρέπει να συνυπολογιστούν. Για παράδειγμα, οι πολυφασματικοί και υπερφασματικοί δέκτες μπορούν να παρέχουν δεδομένα μόνο κατά τη διάρκεια της ημέρας όταν δεν υπάρχει νεφοκάλυψη. Αντίθετα, οι δέκτες ραντάρ συνθετικού ανοίγματος μπορούν να παρέχουν δεδομένα και κατά τη διάρκεια της νύχτας ανεξαρτήτως καιρικών συνθηκών. Η πρόσφατη ραγδαία αύξηση του όγκου των δεδομένων ραντάρ συνθετικού ανοίγματος επιτρέπει την ανάπτυξη νέων μεθοδολογιών που παλαιότερα δεν ήταν δυνατή. Στη συγκεκριμένη διδακτορική διατριβή παρουσιάζεται η διερεύνηση των δυνατοτήτων υπαρχουσών μεθοδολογιών και η ανάπτυξη νέων μεθοδολογιών και λογισμικών πακέτων που αξιοποιούν χρονοσειρές δεδομένων ραντάρ συνθετικού ανοίγματος για τρεις θεματικές ενότητες, οι οποίες σχετίζονται με την κλιματική αλλαγή. Αυτές είναι οι παραμορφώσεις εδάφους, η εδαφική υγρασία και οι πλημμύρες.

Πρώτα, αξιολογούνται οι μεθοδολογίες εκτίμησης των εδαφικών παραμορφώσεων από δεδομένα ραντάρ συνθετικού ανοίγματος και στη συνέχεια διερευνώνται οι φυσικοί παράγοντες που τις προξενούν. Η παραμόρφωση του εδάφους είναι μια βασική μεταβλητή της κλιματικής αλλαγής που συνδέεται με α) την αύξηση της άντλησης υπόγειων υδάτων λόγω της αυξανόμενης ξηρασίας β) την απόψυξη του εδαφικού στρώματος που ήταν μόνιμα σε παγετό, λόγω της αύξησης της θερμοκρασίας και γ) τον κίνδυνο βύθισης παράκτιων περιοχών και επομένως αύξησης των πλημμυρικών γεγονότων. Παρουσιάζεται μια διεξοδική ανάλυση και αξιολόγηση αρκετών μεθοδολογιών επεξεργασίας χρονοσειρών ραντάρ συνθετικού ανοίγματος για την εκτίμηση παραμορφώσεων εδάφους. Στη συνέχεια, διερευνάται η ακρίβεια της εκτίμησης της κατακόρυφης συνιστώσας της παραμόρφωσης του εδάφους που υπολογίστηκε από δεδομένα ραντάρ συνθετικού ανοίγματος πολλαπλών τροχών. Έπειτα αναπτύσσεται μια μεθοδολογική προσέγγιση βασισμένη σε κυματίδια (wavelets) για την εξέταση της συσχέτισης μεταξύ παραγόντων (αιτιών) της

παραμόρφωσης και της παραμόρφωσης εδάφους. Τέλος, περιγράφεται το πακέτο λογισμικού INTERFERON που αναπτύχθηκε για την εκτίμηση της παραμόρφωσης του εδάφους από χρονοσειρές συμβολομετρικών δεδομένων ραντάρ συνθετικού ανοίγματος.

Η δεύτερη θεματική ενότητα της παρούσας διδακτορικής διατριβής είναι η εκτίμηση της εδαφικής υγρασίας από συμβολομετρικά δεδομένα ραντάρ συνθετικού ανοίγματος. Η υγρασία του εδάφους είναι μια βασική κλιματική μεταβλητή που χρησιμοποιείται κυρίως για την παρακολούθηση της ξηρασίας. Η κλιματική αλλαγή αναμένεται να αυξήσει την πιθανότητα για μεγαλύτερες, έντονες και πιο συχνές ξηρασίες σε όλο τον κόσμο. Στην παρούσα διατριβή, προτείνεται μια καινοτόμος μεθοδολογική προσέγγιση, η οποία υλοποιήθηκε με την ανάπτυξη του λογισμικού πακέτου ανοιχτού κώδικα INSAR4SM, για την εκτίμηση της επιφανειακής υγρασίας του εδάφους σε ερημικές περιοχές. Παρουσιάζεται η εφαρμογή της σε μια ξηρή περιοχή στην Καλιφόρνια των ΗΠΑ όπου η ογκομετρική επιφανειακή υγρασία εκτιμήθηκε σε υψηλή χωρική ανάλυση (250 m) με αξιοσημείωτη ακρίβεια (RMSE ~ 0.035 m^3/m^3).

Η τρίτη θεματική ενότητα αυτής της διδακτορικής διατριβής είναι η χαρτογράφηση και η παρακολούθηση των πλημμυρισμένων εκτάσεων αξιοποιώντας χρονοσειρές δεδομένων ραντάρ συνθετικού ανοίγματος. Οι πλημμύρες είναι ένας από τους πιο σημαντικούς περιβαλλοντικούς κινδύνους που προκαλεί τεράστιες οικονομικές ζημιές. Η κλιματική αλλαγή αναμένεται να αυξήσει τα φαινόμενα πλημμύρας κυρίως λόγω ακραίων βροχοπτώσεων. Στην παρούσα διατριβή προτείνεται ένα καινοτόμο μεθοδολογικό πλαίσιο για μη επιβλεπόμενη χαρτογράφηση και παρακολούθηση πλημμυρισμένων εκτάσεων χρησιμοποιώντας χρονοσειρές δεδομένων Sentinel-1. Η ακρίβεια της μεθόδου (OA~ 0.97, Kappa score~ 0.77) υπολογίστηκε εξετάζοντας πολλά πλημμυρικά επεισόδια σε όλο τον κόσμο, τα οποία έχουν μελετηθεί από την υπηρεσία EMS COPERNICUS. Το μεθοδολογικό πλαίσιο υλοποιήθηκε στο πακέτο λογισμικού ανοιχτού κώδικα FLOMPY. Επιπροσθέτως, παρουσιάζονται δύο περιπτώσεις οι οποίες αξιοποιούν την εξαγόμενη από το FLOMPY πληροφορία για τις πλημμυρισμένες εκτάσεις. Η πρώτη περίπτωση σχετίζεται με την εκτίμηση των ζημιών από πλημμύρες σε γεωργικές περιοχές και η δεύτερη είναι μια ανάλυση ευαισθησίας ενός συζευγμένου υδροδυναμικού μοντέλου. Και στις δύο περιπτώσεις αποδεικνύεται η σημαντική συμβολή του FLOMPY σε τεχνικά και κοινωνικό-οικονομικά θέματα που προκύπτουν από την κλιματική αλλαγή.

Acknowledgements

Σας ευχαριστώ

LIST OF ABBREVIATIONS

AOI	Area of Interest
CLC	CORINE Land Cover
DEM	Digital Elevation Model
DS	Distributed Scatterer
EMS	Emergency Management Service
EO	Earth Observation
ESA	European Space Agency
GNSS	Global Navigation Satellite System
InSAR	Interferometric Synthetic Aperture Radar
IW	Interferometric Wide swath
LOS	Line of Sight
km/m	kilometer/meter
NASA	National Aeronautics and Space Administration
NDVI	Normalized Difference Vegetation Index
NTUA	National Technical University of Athens
OA	Overall Accuracy
PS	Permanent/Persistence Scatterer
RSLab	Remote Sensing Laboratory of NTUA
RMSE	Root Mean Square Error
S-1/2	Sentinel-1/2
SAR	Synthetic Aperture Radar
SBAS	Small Baseline Subset method
SRTM	Shuttle Radar Topography Mission
TSInSAR	Time Series Interferometric Synthetic Aperture Radar

Table of Contents

1   INTRODUCTION

This doctoral dissertation deals with the subject of exploiting SAR and InSAR satellite data for estimating ground deformation, soil moisture and for monitoring floodwater. The overall work crosses boundaries between earth observation, remote sensing and data science disciplines to identify tools and gain unique insights into the dissertation`s subject. This chapter aims to provide a brief introduction highlighting the current challenges, the motivation, the objectives and the scientific contributions conducted during the dissertation. A detailed description of the contributions of this work are presented in the subsequent chapters.

1.1   Current Scientific Challenges and Motivation

Climate change is not a future problem, it is a major challenge of our time [1]. The need for climate action is an undeniable fact for reducing our risks from the harmful effects of climate change. Adapting to climate change poses challenges on whether and how to adapt activities, systems and sectors to a continuously changing climate [2]. Moreover, as the frequency of climate-related extremes is increasing more economic, social and environmental losses can be caused. Modelling of climate change impacts is a crucial step for adaptation planning for a more resilient tomorrow.

The main impacts of climate change are temperature increase, more severe storms, increased drought, warming and increasing ocean, health risks, hunger, poverty, and biodiversity loss [3]. Many of these impacts are interrelated and have many associated causes. There is an unmet need to better understand the interdependencies between climate change cause/effect variables [4]. Data related to climate risk and losses are crucial to push the frontiers of climate change knowledge [5]. Continuous monitoring, reporting and evaluation is also essential for a systemic climate change adaptation [1]. Finally, it is important to speed up adaptation at a local and global level in order to ensure international climate resilience.

Earth observation data have been used for improving understanding of climate change. Remote sensing enables monitoring at several spatiotemporal scales with global coverage [6]. Exploiting remote sensing big data in conjunction with climate models and conventional observations, improved climate projections and revealed new climate-related insights. However, remote sensing data uncertainties pose challenges for extracting robust information [7]. These uncertainties can be related to biases in sensors and/or retrieval algorithms. There is a need for building systems that make better use of remote sensing data in climate change adaptation actions. In the next paragraphs, we provide a brief description to some of the climate change topics where the use of remote sensing can be beneficial.

Ground deformation is related to several climate change impacts. As we already described, water scarcity can intensify the groundwater depletion and cause ground subsidence. This may cause serious damages in buildings, cultural heritage assets, infrastructures, etc. with severe economic and social impact. Another example is that the warming and the temperature fluctuations can cause land degradation over permafrost regions [13]. Land degradation leads to increased risks to infrastructure and affects the water and carbon cycle by altering the soil freeze-thaw state. Temperature fluctuations are reflected as ground deformation mainly due to the freezing and thawing of the permafrost layer close to the ground surface [14]. Another climate change impact is related to the sea level rise. In many densely populated coastal areas, occurring ground subsidence can increase coastal flood events and magnify the impact of sea level rise which will put a lot of regions below relative sea level. Last, but not least, ground deformation is an indicator for many anthropogenic activities that are connected to climate change. One of the most important ones is mining which is currently responsible for 4 to 7 percent of greenhouse-gas emissions globally [15]. Ground deformation monitoring over a mining region is an essential need [16] during operation and also during sustainable transformation process [17] to minimize its climate impact. The sparsity of ground equipment is considered a huge limitation for understanding and modelling ground deformation dynamics. TSInSAR remote sensing technology using SAR data can make a huge impact by providing invaluable ground deformation estimations [19]. Moreover, the increasing number of SAR satellites and the unprecedented increasing volume of InSAR data offer huge potential for methodological improvements and are important motivation factors for this dissertation.

Climate change increases the probability of longer, intense and frequent droughts over the world [8]. Droughts are caused by high evaporation due to temperature warming and by water sparsity due to less precipitation. Increased precipitation variability due to climate change can also lead to longer periods of droughts. Droughts are directly connected with groundwater [9] usually over agricultural regions. A conjunctive analysis is required to better understand the interconnections between drought and groundwater to create a better water management plan. For drought monitoring, soil moisture is considered one the most essential variables [10]. Due to the limited number of ground soil moisture stations, satellite derived soil moisture information is considered an excellent alternative for soil moisture monitoring. For groundwater monitoring, due to the sparsity of water-level data and in-situ ground deformation observations, remotely sensed ground deformation can be used alternatively [11]. TSInSAR technology can provide accurate ground deformation estimations at high spatiotemporal scales which can be used to track groundwater fluctuations [12].

Flooding is one of the most impacting environmental hazard that causes huge economic damages [20]. The climate-related changes in temporal distribution and intensity of precipitation events is expected to increase flood risk [21]. To mitigate the flood casualties, remote sensing can provide invaluable data that

can be used for flood monitoring and forecasting. Especially SAR sensors which are able to provide data under all-weather conditions, day and night, have an essential role in flood monitoring [22]. The big volume of SAR data with high spatiotemporal resolution offer huge potential for methodological improvements in order to provide accurate floodwater monitoring solutions.

1.2 Objectives

The main objectives of this thesis are outlined as follows:

Objective 1: <u>Assess the performance, interpretability and potential of TSInSAR methodologies for ground deformation estimation.</u> This objective can be divided into accuracy assessment of vertical ground deformation from multiple track TSInSAR results; comparison methodology based on the results produced from different TSInSAR methodologies; discussion of advantages, limitations and critical factors that are related to the performance of several TSInSAR approaches and development of a methodology for the identification of the driving factors of ground deformation which will help the interpretation of TSInSAR estimations.

Objective 2: <u>Development of a methodology for soil moisture estimation using InSAR observations.</u> This objective can be divided into a) review of the existing soil moisture estimation approaches that exploit InSAR observations; b) innovative methodological workflow and c) real world application to demonstrate the performance of the proposed methodology.

Objective 3: <u>Development of a methodological framework for floodwater monitoring using SAR datasets.</u> This objective can be thought of as a) development of an unsupervised methodological framework for floodwater monitoring/mapping using SAR datasets and b) development of real world applications that address problems related to flood modelling and flood disaster assessment.

Objective 4: <u>Release developed research code as open-source software.</u> This objective is inspired by the FAIR (Findability, Accessibility, Interoperability, and Reusability) data principles.

1.3 Scientific publications and software

Most of the work in the framework of this doctoral dissertation has been disseminated through a number of scientific publications and published scientific software as listed below.

<u>Journals</u>

- **Karamvasis, K.**, & Karathanassi, V. (2020). Performance Analysis of Open Source Time Series InSAR Methods for Deformation Monitoring over a Broader Mining Region. Remote Sensing, 12(9), 1380.
- **Karamvasis, K.**, & Karathanassi, V. (2021). FLOMPY: An Open-Source Toolbox for Floodwater Mapping Using Sentinel-1 Intensity Time Series. Water, 13(21), 2943.
- **Karamvasis, K.**, & Karathanassi, V. (2022). Soil moisture estimation from Sentinel-1 interferometric observations over arid regions. Computers and Geosciences. (under review)

Author Contributions: For all the journal articles, I came up with the idea, designed the methodology, implemented all the source code, conducted all experiments and prepared the original manuscript draft. The manuscripts were revised and edited by Prof. Vassilia Karathanassi.

Conferences

- **Karamvasis, K.,** & Karathanassi, V. (2019). Multi-track N-SBAS Sentinel-1 Interferometry focused on opencast mine monitoring: The case study of the Ptolemaida-Florina coal mine in Greece. 4th Joint International Symposium on Deformation Monitoring, Athens Greece.

  Author Contributions: I came up with the idea, designed the methodology, implemented all the source code, conducted all experiments and prepared the original manuscript draft. The manuscript was revised and edited by Prof. Vassilia Karathanassi.
- **Karamvasis, K.**, & Karathanassi, V. (2021). Exploring Driving Factors of Ground Deformation Using Wavelet Analysis Case Study of Kastoria Lake. FRINGE 2021, ESA, online event.

  Author Contributions: I came up with the idea, designed the methodology, implemented all the source code, conducted all experiments and prepared the original manuscript draft. The manuscript was revised and edited by Prof. Vassilia Karathanassi.
- Gounari 0., Falagas A., **Karamvasis K**., Tsironis V., Karathanassi V., Karantzalos K. (2022): Floodwater Mapping & Extraction of Flood-Affected Agricultural Fields. Living Planet Symposium Bonn 23-27 May 2022.

  Author Contributions: I came up with the idea, designed the methodology and implemented the source code related to floodwater mapping from SAR data. Olympia Gounari implemented the source code related to rule-based crop delineation and conducted the experiment over the region of interest. Vasileios Tsironis implemented the U-Net architecture for crop delineation. Alexandros Falagas implemented the preprocessing scheme of Sentinel-2 data. I and

Alexandros Falagas integrated the developed functionalities into the initial software. The manuscript was revised and edited by Prof. Vassilia Karathanassi and Prof. Konstantinos Karantzalos.

- Zotou I., **Karamvasis K**., Karathanassi V., Tsihrintzis V. (2022): Sensitivity of a coupled 1D/2D model in input parameter variation exploiting Sentinel-1-derived flood map. 7th IAHR Europe Congress. September 7-9, 2022.

    Author Contributions: My main contribution in this work is the extraction of flood map extraction from Sentinel-1 data. Ioanna Zotou came up with the idea, designed the methodology, conducted the experiments and prepared the original manuscript draft. The manuscript was revised and edited by Prof. Vassilia Karathanassi and Prof. Vassilios Tsihrintzis.

Scientific software

- **IN**terferometric **T**ime s**ER**ies **F**or d**E**fo**R**mati**ON** (**INTERFERON**) In-house software (2018 - 2022): Permanent and Distributed scatterer interferometry for ground deformation estimation: (will be released under GPLv3 license)
- **FLO**od **M**apping **PY**thon toolbox (**FLOMPY**) GPLv3 license (2021-2022): https://github.com/rslab-ntua/FLOMPY
- **I**nterferometric **S**ynthetic **A**perture **R**adar **for S**oil **M**oisture estimation (**INSAR4SM**) GPLv3 license (2022): https://github.com/rslab-ntua/InSAR4SM

1.4   Thesis Roadmap

The following chapters in this dissertation are briefly summarized below: Chapter 2 constitutes of the work related to ground deformation estimation from TSInSAR methodologies. In Chapter 3, we introduce a methodological pipeline for estimating soil moisture from InSAR observables (interferometric coherence and phase closure) over arid regions. In Chapter 4, the work related to floodwater mapping using multitemporal SAR observations is presented. Finally, in Chapter 5 we provide concluding remarks and suggestions for future work.
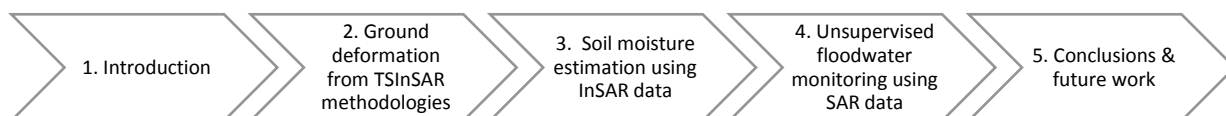

Figure 1.1 Thesis Roadmap

2 GROUND DEFORMATION ESTIMATION FROM TSINSAR METHODOLOGIES

In Chapter 2, the work related to ground deformation estimation using TSInSAR methodologies is presented. In section 2.1, we provide an introduction and specific research questions that we will try to answer. Next, in section 2.2, the main theoretical concepts of several TSInSAR algorithmic approaches are described. In section 2.3, three case studies using TSInSAR approaches are presented. In the first case study, a multi-track TSInSAR approach able to estimate vertical and horizontal over a mining region is presented. In the second case study, a performance comparison between three TSInSAR open source implementations over an extended mining region is presented. In the third case study, a wavelet-based approach to explore the connections of five potential driving factors (surface soil moisture, precipitation, lake water area variations, NDVI and ground temperature) with ground deformation results from TSInSAR is presented. In section 4, a brief description of the in-house software package Interferon is provided. In Section 5, the conclusions regarding TSInSAR studies for ground deformation estimation are presented.

2.1 Introduction

Ground deformation information can be acquired from various techniques. Traditional ground-based methods such as leveling and GNSS (Global Navigation Satellite System) are widely used and considered the most accurate and well-developed methods [23]. However, for extended areas, the aforementioned techniques are labor-intensive and limited in spatial coverage and density. By contrast, TSInSAR can obtain surface deformation along the LOS exploiting the phase information of the SAR images acquired at different times.

TSInSAR techniques were proven to be powerful tools and have gained increasing attention because they can provide at all-times, all-weather deformation information in a wide area. This is related to the recent advances in terms of the temporal/spatial resolution and coverage of satellite data, the processing chains and the increase of the computational capabilities (parallel processing, cloud computing) [24]. A lot of TSInSAR techniques have been developed and widely applied in many fields such as earthquake displacement [25], volcanic activity [26], groundwater/gas extraction [18], landslides instability [27], [28], urban subsidence [29], and mining activity [30]. A brief summary of the most important TSInSAR methods is presented in the next paragraphs.

The oldest and first group of TSInSAR approaches focuses on a subset of points (called measurement points) that have high phase stability and are referenced as persistent scatterer (PS) methods [31]–[34]. PS methodologies extract the measurement points from a single-master network interferograms and can achieve even submillimeter accuracy [35]. The main selection strategies of the measurement points are

based on their phase variation in time [31] or on the correlation of their phase variation in space [34]. Many applications of PS methods can be found for urban environments. An open-source implementation of a PS methodology is provided by Stamps toolbox [34], [36].

The second group of TSInSAR approaches focuses on exploiting a redundant network of multi-master interferograms that have small temporal and spatial baselines. These approaches are referred to as Small BAseline Subset (SBAS) methods [37]. The network of the SBAS methods consists of unwrapped interferograms that can be fully-connected or form isolated clusters over time. Fully-connected networks are inverted using least square estimation or L1-norm minimizations [38]. Non-fully connected networks are inverted/solved using singular value decomposition or a regularization constraint to obtain physically sound solutions [37], [39]. Open source implementations of SBAS methodologies are provided in several software packages, such as GMTSAR [40], Giant [41], Stamps [36], MSBAS [42], Pyrate [43] and, Mintpy [44].

The third group of TSInSAR approaches exploits all the possible interferograms of a given set of SLC acquisitions [45]–[47]. Similar to the aforementioned techniques, the goal of the network inversion is to obtain optimal and noise-limited phases of the given SAR acquisitions. Maximum likelihood estimator [48] and eigenvalue decomposition of the covariance matrix [49], [50] are some of the tools that can be used for optimal phase estimation. The main characteristic of these methods is that the network inversion is performed before phase unwrapping. Another important characteristic of these methods is the preprocessing of the distributed scatterers in order to be processed by PS algorithms. The preprocessing step enables the joint processing of distributed and persistent scatterers, which increases coverage with high accuracy deformation retrieval. This is due to the fact that the estimator of a distributed scatterer signal provides triangular phase that enables spatiotemporal (3D) unwrapping, which is superior to 2D unwrapping [51]. The main limitation of these techniques is the computational complexity given the big volume of SAR data.

The unprecedented availability of open SAR data, open source interferometric software packages as well as the ready-to-use interferometric products such as ground displacement maps, resulted in their wide use by a range of stakeholders such as scientists, institutional organizations and the commercial sector. Furthermore, in recent years, many algorithmic approaches and improvements able to exploit the large amount of multi-temporal interferometric SAR data and provide high accuracy ground deformation results have been developed. However, the repeatability and the reliability of multi-temporal interferometric processing still remains an open issue, mainly due to the ongoing and continuous algorithmic improvements [52]. Different processing methodologies may produce inconsistent ground displacement results. Moreover, the high complexity of the interferometric SAR signals makes interpretation a challenging task [53].

In this chapter, the three published case studies related to ground deformation from TSInSAR methodologies are presented. In the framework of this dissertation, the main objectives of this chapter are:

- Examine the accuracy of vertical ground deformation estimations from multiple track TSInSAR results.

- Develop a comparison methodology for results from different TSInSAR methodologies.

- Present the positive and negative sides of several TSInSAR approaches in respect to environmental conditions, accuracies and spatial coverage.

- Present the critical factors that are related to the performance of several TSInSAR approaches and present some best practices.

- Develop a methodology for identification of driving factors of ground deformation that will help the interpretation of TSInSAR estimations.

2.2 Description of TSInSAR methodologies/implementations
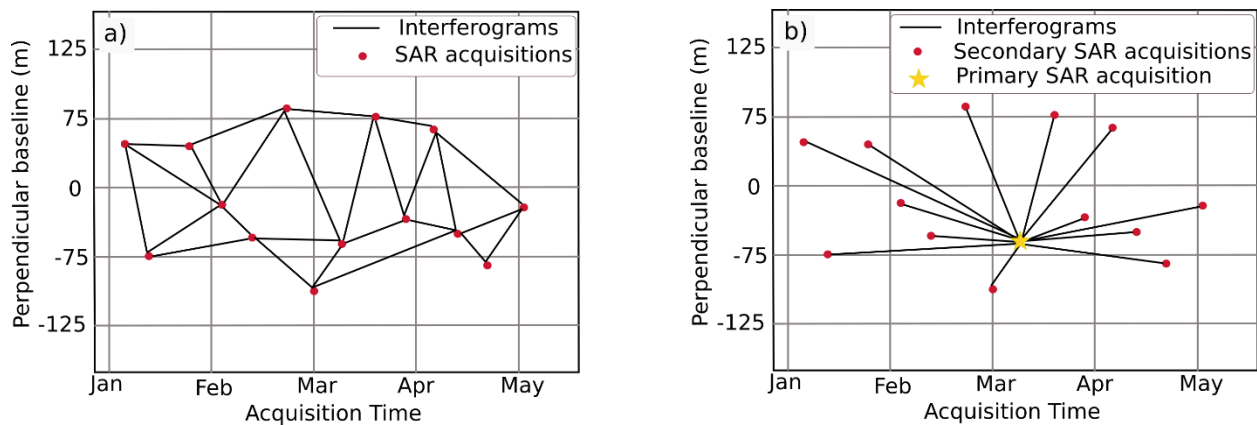
Figure 2.1 Interferogram network types a) fully connected network for Mintpy, Giant and Stamps/MTI approaches b) single master network for Stamps-PS approach

2.2.1 Mintpy-Miami InSAR Time-Series Software in Python

The Mintpy toolbox is a python 3 software for small baseline InSAR time series analysis. The input is a stack of differential interferograms that form a fully connected network (Figure 2.1a). Interferograms have to be already unwrapped with small geometric perpendicular and temporal baselines for maximizing their quality. For modern SAR constellations with small orbital tube and short revisit time, such as Sentinel-1, a fully connected network of interferograms can easily be formed. The input stack can be generated using among other tools, the Interferometric SAR Scientific Computing Environment ISCE [54]. The main steps of the interferometric processing performed by ISCE are orbit correction, de-burst, co-registration, interferogram generation and adaptive filtering, subtraction of topographic phase using given Digital Elevation Model (DEM) and 2D (space) unwrapping.

The Mintpy toolbox consists of three main processing steps a) the raw interferometric phase time series calculation b) the correction of the raw phase time series from error sources and c) the noise evaluation step that results in the exclusion of noise SAR acquisitions and the final calculation of noise-reduced displacement time series. Moreover, in order to have a quality index for the extracted deformation values, temporal coherence is calculated for each pixel according to [55].

The first processing step of Mintpy is the inversion of the input redundant, fully connected stack via an unbiased weighted least square estimator in order to acquire raw time series of interferometric phase for each date. The weight information can be related with a uniform behavior or no weighting [37], spatial coherence at pixel level [56], [57], inverse of the phase variance [58], and nonparametric Fisher information matrix (FIM) [50], [59]. For this study, only the inverse of the phase variance weighting was selected because, according to [48] and for a small number of looks [44] the inverse of phase variance as a weighting factor gives the most robust and one of the best performances for network inversion.

The second processing step is the correction of the raw inverted phase time-series from phase error sources at the time domain. Deterministic components such as tropospheric delays, topographic residuals and/or phase ramps are preserved after inversion and can be suppressed in the time-series domain in order to obtain a time series of noise-reduced displacement. Moreover, a correction scheme of 2D unwrapping procedure errors with a variety of approaches is offered. The unwrapping correction method that was selected is related with the phase closure of triplets of interferograms, based on the assumption that the SAR phase field is conservative [25].

The third processing step is the noise evaluation of each SAR acquisition in terms of residual phase. Mintpy considers the residual phase as a combination of residual tropospheric turbulence, uncorrected ionospheric turbulence, and the remaining decorrelation noise. The root mean square error of the residual phase is calculated for each SAR acquisition after a quadratic deramping [60] over the reliable pixels that are used in the network inversion. The identified noisy acquisitions are excluded and the topographic residual and velocity estimation is performed for a second time.

2.2.2 Giant - Generic InSAR Analysis Toolbox

The Giant toolbox [41] was developed for small baseline InSAR time series analysis in python 2. It requires a stack of differential geocoded or slant-range unwrapped interferograms (Figure 2.1a) for the extraction of ground deformation time evolution information. The input interferogram stack can be generated among other tools using ISCE [54].

The first step is the preparation of the interferograms stack by applying phase correction schemes. Firstly, a deramping correction scheme at a network level [25], [61] is applied. Secondly, a tropospheric correction scheme based on ERA-5 atmospheric model [62] is applied.

The next step is the inversion of the interferograms stack to obtain deformation information. Conventional SBAS [37], NSBAS [39], [62], [63] and Multiscale InSAR Time-Series MInTS [64] are the available inversion choices. Conventional SBAS uses singular value decomposition to redundant information from the interferometric stack to provide ground deformation time series. The main difference of NSBAS with respect to the conventional SBAS technique is that NSBAS includes constraints from user predefined temporal functions to join islands of disconnected interferograms. The main differences of MInTS with respect to conventional SBAS technique are firstly the transformation of the interferometric phase into the wavelet domain before the temporal inversion and secondly the description of the time evolution of the ground deformation by predefined functions. In all the strategies, the inversion operation is performed in each pixel separately subject to coherence and valid number of observation criteria. In this dissertation, only Giant-NSBAS approach was considered.

2.2.3   Stamps - Stanford Method for Persistent Scatterers

Stamps consists of a PS and a combined PS and SBAS (Stamps/MTI) processing workflow which are briefly described below. Comprehensive algorithm descriptions can be found in [33], [36], [65].

The Stamps-PS approach (Figure 2.1b) is based on spatial correlation of interferometric phases. Conventional PS methodologies [31] extract deformation over high amplitude pixels assuming a well-defined phase history. Furthermore, the phase history of each pixel is compared with a predefined temporal deformation model. Stamps-PS implementation is based on the stable spatial phase characteristics and is able to extract deformation over low-amplitude pixels without prior knowledge of temporal deformation behavior. However, the assumption that the deformation is spatially correlated is not true for isolated movement of individual scatterers which are considered as noise. Stamps-PS approach has a lot of applications in urban and non-urban areas like volcanic regions.

The combined Stamps/MTI approach (Figure 2.1a) is able to combine information from PS and SBAS at a full resolution and have some clear advantages over conventional multilooking SBAS approaches. It was observed that multilooking procedure may include pixels that completely decorrelate and add noise to the multilooked pixel. In this direction, adaptive multilooking approaches have been developed [46]. The full resolution processing that Stamps/MTI adopts, mitigates the noise from traditional boxcar multilooking procedures. Moreover, Stamps/MTI performs the unwrapping of the phase in three dimensions (space and time) and therefore produces more robust results in respect to two dimensional (space) unwrapping algorithms [34].

Both approaches include a selection strategy of pixels that the deformation information will be extracted. First, for computation reduction reasons an initial selection of pixels that are expected to be either persistent scatterers or slowly-decorrelating filtered phase (SDFP) pixels through amplitude dispersion analysis [65] is performed. For the selected pixels, a spatially-correlated part of interferometric phase is estimated by bandpass filtering of the surrounding pixels. The spatially-correlated part consists of phase due to ground displacement, atmospheric phase delay, orbit errors and spatially-correlated height error. Moreover, for each measurement point, a spatially-uncorrelated height/DEM error is estimated from its correlation with perpendicular baseline. By subtracting the spatially-correlated part and the spatially-uncorrelated height error from raw wrapped interferometric phase a temporal coherence metric is calculated for each measurement point. Then, a thresholding approach on the aforementioned coherence metric is performed to select the measurement points that are going to be processed.

2.3 Ground deformation case studies

2.3.1 Multi-track N-SBAS Sentinel-1 Interferometry focused on opencast mine monitoring: The case study of the Ptolemaida-Florina coal mine in Greece

2.3.1.1 Introduction

Deformation monitoring in mining areas has a great importance because mining activities impact the nearby environment and may cause severe mining hazards [66]. From the "interferometric" point of view, the mining areas have some special issues that have to be addressed. First of all, it is the loss of coherence that is usually caused by the mining operations that prevent the detection of ground surface deformation [67]. Secondly, the low density and the inhomogeneous distribution of persistent scatterers in the mining regions limit the use of high-accurate persistent scatterer methods [68], [69]. In contrast, SBAS techniques allow the measurement of surface displacements in low reflectivity areas like scattered outcrops, bare soil areas, debris areas that are usually found in mining regions [70].

In this study, a Sentinel-1 multi-track methodology based on N-SBAS [39] is presented. The main objective of this case study is to explore the deformation monitoring ability of the proposed methodology in mining regions. The case study of the Ptolemaida-Florina coal mine in Greece helped us to outline the strengths and the limitations of the proposed methodology. Validation between multi-track N-SBAS and levelling measurements was conducted. The output of this case study shows the effectiveness of the Sentinel-1 constellation for the monitoring of ground subsidence over non-active mining areas. The results can be useful for management, risk analysis and planning of mining operations.

2.3.1.2 Methodology

One of the limitations of deformation measurements made with TSInSAR techniques is that they provide only one component of the surface deformation in the satellite's line of sight (LOS) [71]. The availability of ascending and descending tracks of Sentinel-1 constellation that cover the same region is important in order to resolve the 3D surface deformation. Each orbit/track can yield only a single deformation measurement along LOS (Figure 2.2) so multiple orbits should be exploited in order to estimate northing, easting and vertical components.
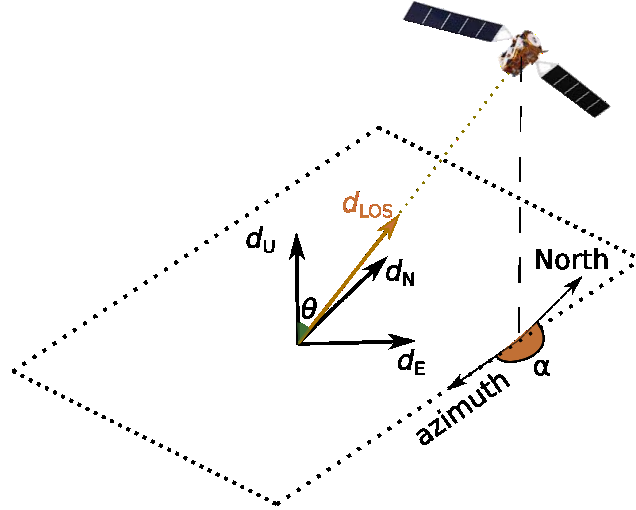

Figure 2.2 The SAR imaging geometry and the relationship between LOS deformation and the vertical, North-South and East-West components. θ and α are the radar incidence angle and the orbit azimuth angle, respectively.

According to Figure 2.2, the following equation derives [71], [72]:

$$d_{LOS} = d_U cos\theta + sin\theta(d_N sin\alpha - d_E cos\alpha) \tag{2.1}$$

Where d_{LOS} = deformation along LOS; d_U, d_N, d_E = vertical, North-South, East-West deformation components; α = heading angle; θ = incidence angle

From a theoretical point of view, in order to be able to resolve the 3D deformation components at least three LOS deformation measurements are required. Due to the high computational cost to obtain deformation time series for three tracks, a method that combines information from neighboring pixels is proposed. The main assumption of the method is that a subset of the neighborhood pixels share the same deformation behavior with the central pixel for which we want to obtain the 3D deformation components. The neighborhood pixels are defined by a 3x3 window. The gradient information is the criterion for neighborhood pixel selection. Gradient is estimated using a DEM with better resolution than the SAR grid. Two neighborhood pixels with the most similar gradient with the central pixel are selected for the solution

of the system of equations (2.1). In the following section a case study in Ptolemaida-Florina mine is presented.

2.3.1.3   Study area and datasets

The area of interest is located in the region of Western Macedonia (Kozani), Greece, which is considered one of the most important industrial areas in Greece. In particular this work focuses on a part of the Ptolemaida-Florina opencast lignite mine, illustrated in the left part of Figure 2.3. Due to the mining activities in the AOI "unstable" regions were delineated. In Figure 2.3, the "unstable" regions are denoted with a gray color. In these regions, TSInSAR techniques cannot provide reliable results due to strong decorrelation of the SAR signal. The main objective of the case study is to examine the stability of the zone along "Soulou" water stream that could potentially provide insights about the risks of the existing transportation network inside the mining area. For the validation of the results of the proposed methodology 10 leveling points located in the buffering zone along the "Soulou" water stream have been used.

A total of 249 Sentinel-1 TOPS IW acquisitions from the descending track 80 and the ascending track 102, spanning two and a half years have been processed. Around 1400 interferograms were created and processed with the multi-track Giant-NSBAS technique that was described in the previous section. The processed area is about 4x8 km^2. The earlier scene of each orbit stack was selected as the zero-deformation reference image. As an external DEM, a photogrammetric DEM with ground pixel size of 5 m, provided by KTIMATOLOGIO S.A. is used.
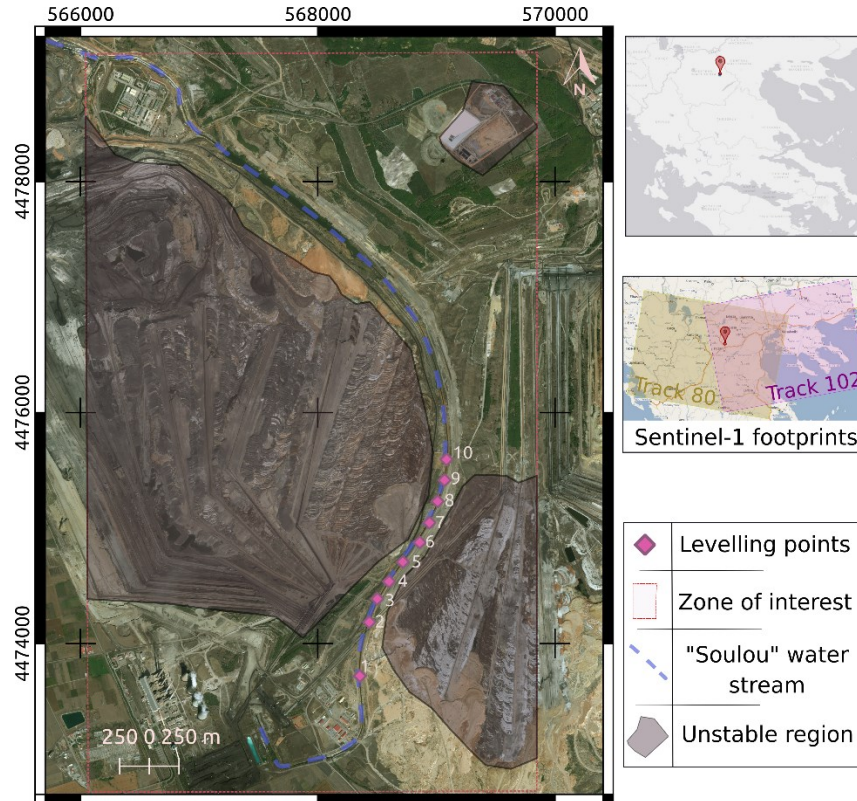
Figure 2.3 Study area (part of Ptolemaida-Florina coal mine) and available datasets
(Sentinel-1 and leveling). Reference system is WGS84 UTM34N. The background image
is a very high resolution optical image © Google Earth Copyright 2018

2.3.1.4   Results and validation

In this section the most significant results are reported and analyzed. In Figure 2.4 the cumulative displacements for the time period from the start of 2016 till the half of 2018 are presented. The pixel size of each map/grid in Figure 2.4 per each component is 15m. It can easily be identified that the vertical displacement values are relatively higher than in the other directions. Looking closely at the vertical component the subsidence zone (red ellipse) close to the active mining regions (gray regions) can be identified. It is important to state that for each point in the grid the time series of displacement are calculated. Inside the subsidence zone, the time series displacement information of a point (bottom right of Figure 2.4) is presented. Different linear components of the deformation in a time sense can be identified. The decreasing behavior of the subsidence rates is clearly evident.
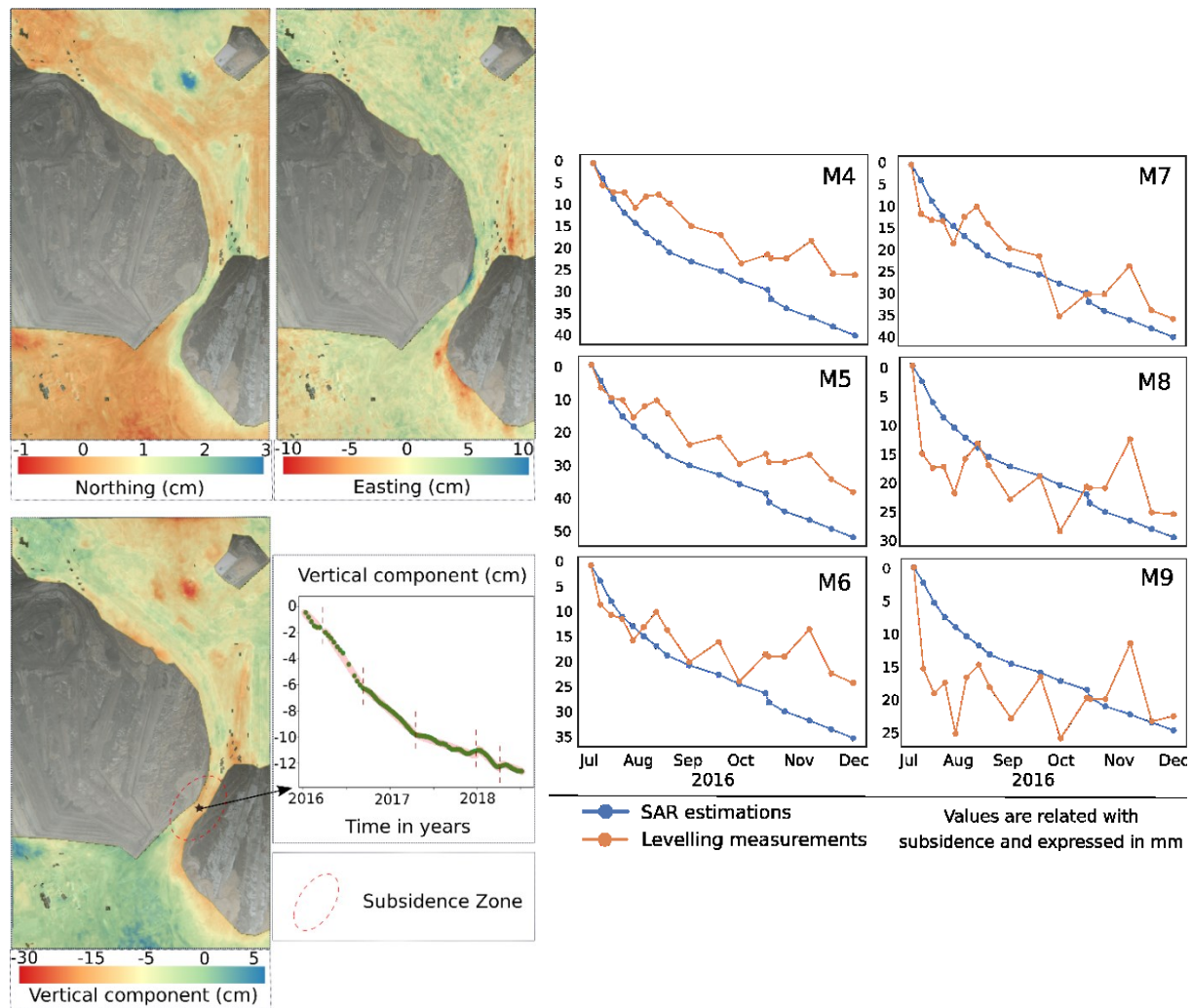
Figure 2.4 Cumulative displacement components from 10/1/2016 to 5/7/2018. Time series of displacement inside the subsidence zone (bottom right).

Figure 2.5 Time series of vertical ground deformations in correspondence of six locations the subsidence zone. The nearest centroid of the deformation grid was selected according to location of the leveling point.

The validation procedure has been performed by comparing the vertical component of multi-track N-SBAS approach with the levelling measurements in the levelling points close to the subsidence zone (Figure 2.5). In Figure 2.5, for each point, the evolution of the subsidence according to leveling measurements and to multi-track Giant-NSBAS estimations (denoted as SAR estimations) is presented. In most cases, SAR estimations tend to overestimate subsidence values. On the other hand, the subsidence rates between the two different methods are in good agreement. The overall RMSE between all (160) the leveling measurements at 10 leveling points and the multi-track N-SBAS estimations is 1.07 cm.

2.3.1.5   Discussion and conclusion

The above results demonstrate that the subsidence zone along a part of the "Soulou" water stream can be identified by the proposed methodology. In particular, subsidence and subsiding trend can be estimated with centimetric accuracy with the proposed technique over a complex mining environment. The subsidence is possibly connected with operations in the mine. However, the interpretation of the measured/observed deformation patterns is a complex task and requires the knowledge of the geological, tectonic, hydrogeological and geotechnical conditions. A deeper understanding of the subsidence mechanism requires more investigation.

The validation of the methodology for average subsidence values and subsidence rates showed that the proposed method can provide high temporal/spatial resolution and accurate subsidence information. In other studies such as [46], millimetric accuracy level has been achieved using an approach mainly based on persistent scatterer interferometry. Due to the absence of persistent scatterers in the study area, the centimetric level of accuracy is considered satisfactory. Combining InSAR and leveling measurements can be a good strategy to better monitor the subsidence of the area of interest. One possible solution for better monitoring of the subsidence phenomena can be the following: (1) to detect the hotspot areas using the multi-track Giant-NSBAS technique over the whole region and; (2) to plan ground survey measurements and collect precise ground information about the hotspot areas.

One of the most important limitations of the proposed method is related to the orientation and the slope of the ground. In steep-slope regions, the reliability of the interferometric estimations is decreased mainly due to geometric distortions of the SAR signal [23]. The geometric distortions also affect the spatial resolution of the SAR sensor which will cause lower spatial resolution of the final deformation results.

Another limitation factor of the proposed method is the 1- dimensional measurement of SAR systems in the LOS direction [71]. Moreover, due to the current near-polar orbiting SAR sensors the accuracy of each estimated component is different. The north component is considered the most difficult to determine, due to the small angular separation of the different LOSs in respect to the South-North direction [71]. In other studies, 3D deformations have been resolved using offset-tracking azimuth techniques [73] and multi-aperture InSAR techniques [68], [74]. The aforementioned techniques are valuable tools mainly in studies of large-scale displacement events like earthquakes, volcano eruption, glacier dynamics but they cannot provide sufficient accuracy for small-scale deformation phenomena [75]. The proposed approach which is based on the combination of multiple track interferometric results can produce estimations with sufficient accuracy at the vertical direction. Even though a lot of methods that resolve the 3D deformation components have been developed, it remains unclear which approach is the most suitable for each case [75].

One of the benefits of the proposed method is that the produced results can support decision makers for mining risk management and disaster awareness. The fact is that active mining operations are well monitored by the mining authorities. However in abandoned mines or abandoned regions of the mines even though they have been considered secured, hidden factors can cause geohazards at any time [76]. The proposed method can provide critical information to mitigate fatalities and ensure the safety of mining operations and local societies during pre-mining, mining and post-mining periods.

The multi-track Giant-NSBAS method yielded deformation results with centimetric level of accuracy at the vertical component. It has to be tested in regions with different conditions and to be compared with other methods. The results of the proposed method can be used for further planning of the ground surveys from mine authorities. Using Sentinel-1 free data the proposed method can provide regional coverage and continuous delivery information with no cost. The produced results can support decision making authorities for risk mitigation and sustainability.

2.3.2   Performance Analysis of Open Source Time Series InSAR Methods for Deformation Monitoring of Ptolemaida-Florina coal mine

2.3.2.1   Introduction

Ground movements and surface deformation on mines can lead to instabilities and slope failures that can cause risks to personnel, equipment and production [77]. The main limitations in our ability to monitor deformation in mining regions are the difficult and fast changing conditions caused by the ongoing mining activity. In order to successfully monitor the complex spatial and temporal behavior of the deformation in mining regions, a monitoring system with suitable spatial density of measurement points (MPs) with a high measurement frequency is required. In most cases, the monitoring techniques of such a system can be divided into two main categories. The first category is related to surveying techniques that determine the absolute and relative positions of certain points. The most popular surveying instruments that are commonly used are GNSS (Global Navigation Satellite Systems), total stations, levels, Terrestrial Laser scanners, Ground-based SARs, and photogrammetric cameras. The second category is related to the use of geotechnical equipment such as extensometers, piezometers, inclinometers etc. The aforementioned conventional techniques can provide high quality measurements but are limited by their operation and maintenance cost.

Due to the high maintenance and operation cost of the aforementioned deformation monitoring strategies, alternative approaches based on remote sensing data can potentially improve the monitoring procedure in terms of cost and accuracy. TSInSAR methodologies are capable to extracting the time series of ground deformation from a set of SAR acquisitions [78]. In the mining world, to our knowledge, there are only a few organizations that are using TSInSAR deformation results in existing deformation

monitoring systems. Open source tools play a crucial role in this respect. Nowadays, the availability of the TSInSAR algorithms will enable mining organizations and interested stakeholders to generate their own SAR derived ground deformation estimations. Given the fact that most of the mining organizations perform ground surveys for deformation measurements, open source TSInSAR estimations can be assessed and validated, and capabilities and limitations of each TSInSAR approach can be pointed out. However, an assessment and comparison approach of the results between different TSInSAR approaches and the in-situ measurements is missing. In fact, this will not only provide best practices and insights on the preferred existing methodological strategies over mining regions but also will potentially support the rapid evolution of algorithmic approaches that will make optimal use of big data in terms of accuracy and computational cost. Therefore, the following comparison methodological framework is proposed.

2.3.2.2   Comparison framework

The proposed comparison methodological framework consists of three steps. The first step is the conversion of the TSInSAR results to vector GIS compatible format with common attributes. Raster datasets from each of the selected open source TSInSAR tools (Stamps, Giant, Mintpy) are converted to TSInSAR point vector datasets mainly for visualization reasons and also to benefit from GIS processing tools. The common structure of the vector data from different TSInSAR tools is suitable for post-processing and comparison analysis.

The second step is the identification of the homologous points between the different TSInSAR point vector datasets. For every pair of vector datasets, a set of points for comparison is selected using a geographical distance criterion. For every point in the first TSInSAR result, the point from the second TSInSAR result with the nearest distance is selected. If this distance is below the predefined geographical distance, then this pair of points will be compared. For each pair of TSInSAR point vector datasets, a vector file including the comparison points is created.

The third step is the calculation of the similarity metrics for each point. Similarity metrics are important for an insightful comparison of time series data. The selection of the similarity metrics is required for optimizing grouping that can potentially reveal distinctive time-dependent processes related with deformation or noise sources. The Euclidean distance metric was selected because a) can provide robust results in a wide range of applications [79] and b) can provide insights because the unit have the same units as the input data. Moreover, the dynamic time warping method [80] has been used. Dynamic time warping method can handle time series that don't share the same exact time of observations, like the deformation time series that have different observation dates when they come from different sensors, different orbit geometries or result from different algorithms that exclude some observation dates. The Euclidean distance

metric is expressed as the RMSE by setting the one TSInSAR point vector dataset as a reference dataset and the other as test dataset. RMSE is calculated according to the following formula:

$$RMSE_{HP} = \sqrt{\frac{\sum_{i=1}^{N_{SARs}}(d_{methodA}^i - d_{methodB}^i)^2}{N_{SARs} - 1}} \tag{2.2}$$

Where, N_{SARs} is the total number of common used SAR acquisitions for methods A and B, HP is the homologous point that is and, $d_{methodA}^i$ is the ith LOS deformation estimation of method A.

The above steps enable the spatial identification of agreements and disagreements between TSInSAR results in terms of deformation and deformation rates. The spatial identification of these agreements can provide insights regarding the performance of each algorithm. The interested user can focus on particular regions to identify the common deformation patterns or to search potential uncorrected error sources among the different TSInSAR results.

2.3.2.3 Study area

The area of interest is located in the region of Western Macedonia, in Greece, which is one of the most important industrial areas of the country. The land cover classes in the area can be categorized into three main classes according to Corine level-1 land cover classes [81]: artificial surfaces, agricultural areas and forest/semi-natural areas. Interferometric coherence is different for each land cover class and is exploited in a lot of land cover classification studies [82], [83]. The different backscattering properties of each land cover can affect the density of the TSInSAR measurements [84] as well as their expected accuracies.
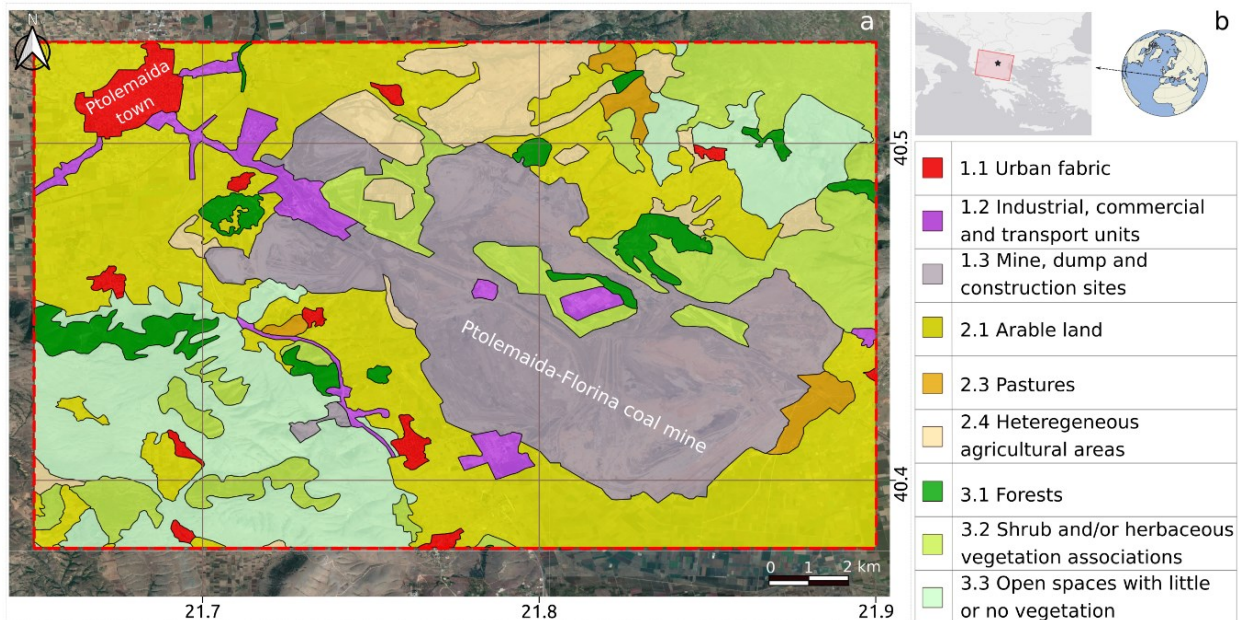

Figure 2.6 Corine land cover level-2 classes of the study area (Source Copernicus Land Monitoring Service [81]). a) The spatial extent of the AOI is denoted with the red dashed rectangle. b) Sentinel-1 footprint is denoted with filled red rectangle. Reference system is WGS84. © Google Earth background map Copyright 2018.

Active mining regions due to fast changing conditions need special treatment. There are regions inside the mine that are under work for certain time periods and other regions that are inactive. Fast changing surface properties result in temporal decorrelation. The study area is included in the dashed red rectangle and is around 357 km2. This work focuses on the part of the Ptolemaida-Florina opencast coal mine, which covers around 90 km2, illustrated with gray color in Figure 2.6a. Since the 1960s, Ptolemaida-Florina mine has been one of the main sources of energy production for the country and is owned by Public Power Corporation S.A.-Hellas [85]. Since 2020, according to the European Commission, the particular coal region is included in the transition initiative that will lead to mine closure. The gradual decrease of mining operations is an interesting subject for the study of post-mining deformation using TSInSAR techniques.

2.3.2.4 Datasets

Due to the expected temporal decorrelation of the mining regions, SAR data from short revisiting (6-day) Sentinel-1 constellation from ESA (European Space Agency) are used. Sentinel-1 consists of two satellites namely, Sentinel-1A and Sentinel-1B that were launched in 2014 and 2016, respectively. Sentinel-1 constellation is a polar-orbiting radar imaging system working at C-band (~5.7 cm wavelength). A total of 125 Sentinel-1 TOPS IW acquisitions from the descending track with relative orbit number 80, dating from 2016 till middle of 2018 have been processed. All the data are in the Single Look Complex (SLC) format and only the VV polarization is considered. All the employed S1 acquisitions were snow-free. The input SLC stack is prepared using ISCE Topstack functionality [86].

Due to the great importance of the stability of the transportation network, leveling measurements were performed in the "Soulou" region from June 2016 to the end of 2016. Leveling measurements for 7 points that are located inside the "Soulou" region Figure 2.7 are used for the validation of the TSInSAR results.
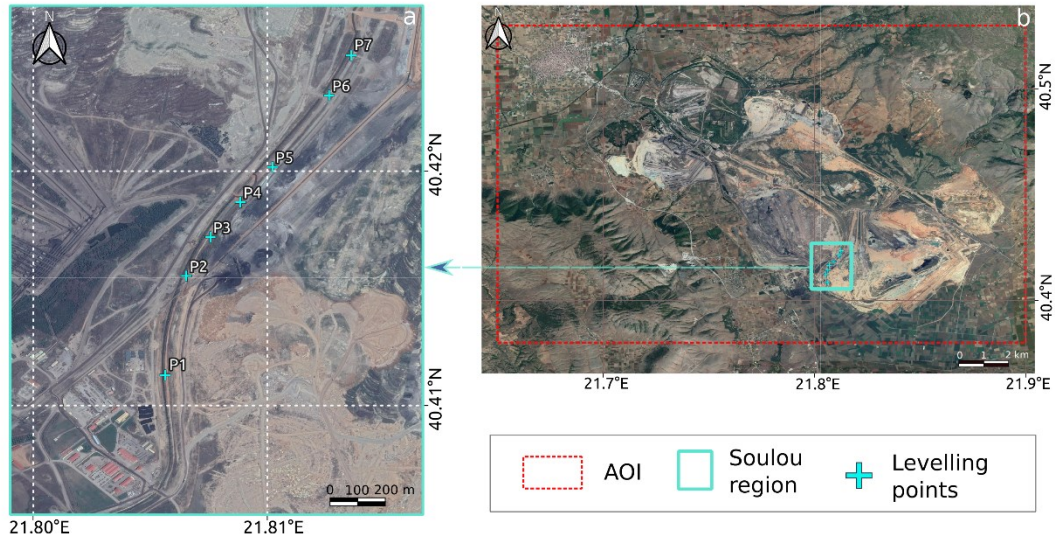
Figure 2.7 In-situ deformation measurements. a) Location of levelling points in Soulou region (light blue rectangle). b) The spatial extent of the AOI. Reference system is WGS84. © Google Earth background map Copyright 2018.

As an external DEM, a photogrammetric DEM with ground pixel size of 5 m, provided by KTIMATOLOGIO S.A is used. The aforementioned DEM was created in the years 2008-2009 and is more recent in respect to the SRTM DEM.

2.3.2.5　Experimental Results

In this section the generated results of the selected algorithms from the open source TSInSAR software packages are presented (Figure 2.8). It is important to state, that because of the high inconsistencies in the connected components of the 2D unwrapping procedure resulting from the available 12-day interferograms at the start of 2016, the Mintpy processing was performed only for 6-day interferograms (from October of 2016 till June of 2018). Stamps and Giant results refer to the time span from January 2016 till June 2018. All the results are differential in space and time. They are spatially related to the same reference point (Figure 2.8) that is located in a very high coherent region of Ptolemaida town. Temporally, the latest date of the SAR acquisition dataset is selected for all the approaches. The temporal reference has been changed to the first available satellite acquisition after the inversion of each algorithm approach. All the results are referring to the LOS sensor to target direction.
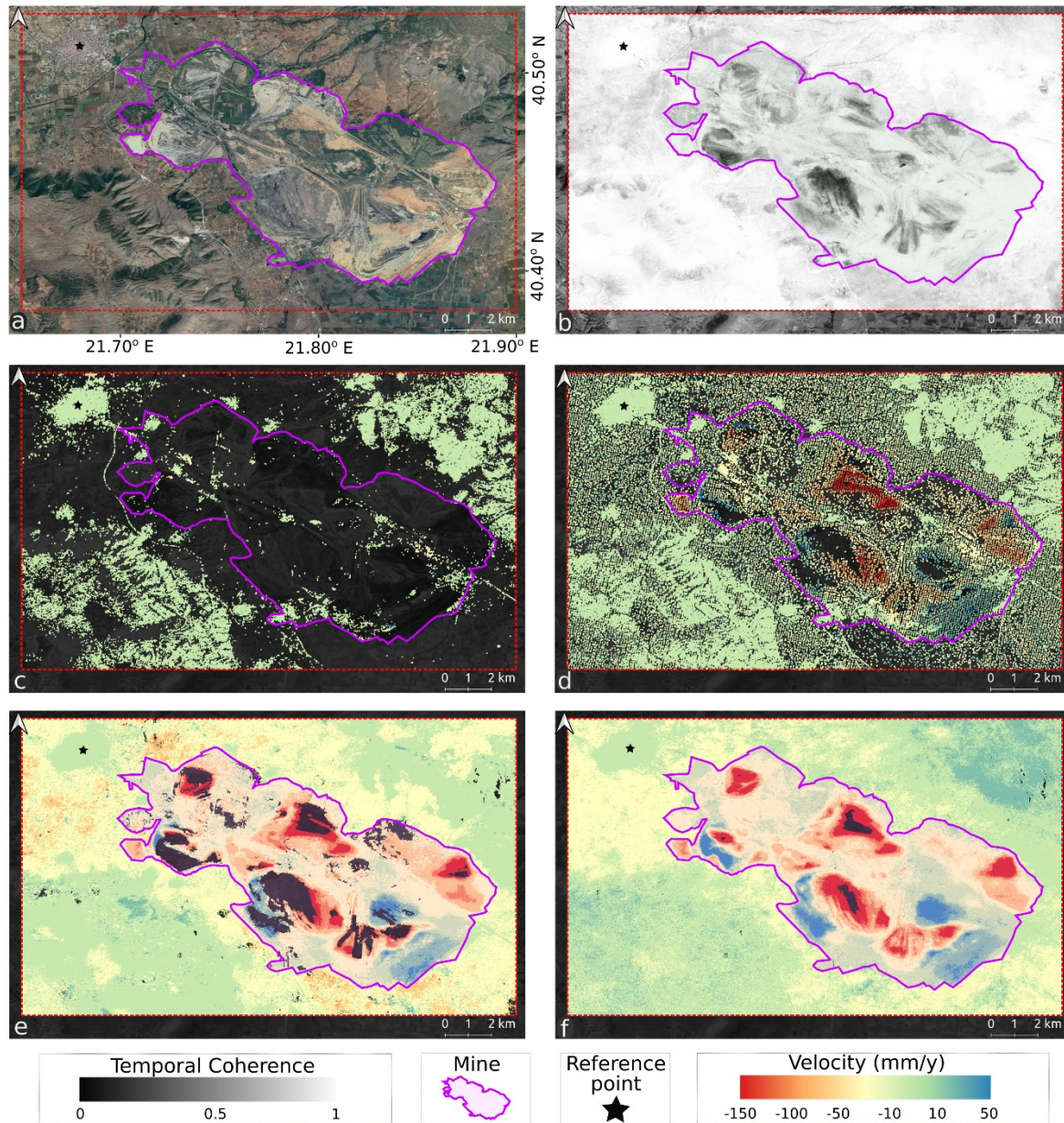
Figure 2.8 LOS deformation rate results of open source TSInSAR approaches. a) Google earth optical image at 2018. AOI is denoted with the red dashed rectangular. Mining region is denoted with purple polygon. b) Temporal coherence of the SAR dataset from Mintpy. c) Stamps Permanent Scatterers (PS) results d) Stamps/MTI results e) Mintpy-WSBAS results f) Giant-NSBAS results. Red color indicates subsidence while blue showing uplift.

In Figure 2.8, it is obvious that the density of measurement points for each selected algorithm is varying. The following can be related with the temporal coherence Figure 2.8b that can be considered as an index for the resulting point density. Temporal coherence can yield values from zero to one. According to Figure 2.8, over bright regions such as urban areas, rocks, roads, abandoned parts of mining regions, which preserve their scattering properties, a high density and good quality result is expected. Over the darker

regions, such as forests, crops, and active mining regions, due to temporal decorrelation, a sparse and low quality result is expected. In particular, the Stamps-PS method yielded around 100K measurement points over the high coherence regions. Using the combined Stamps approach that merges PS and SBAS results the measurement points increased to 135K. It is important to state that oversampling is not implemented in the Stamps processing chain, something that is expected to increase the density of MPs [87]. Mintpy-WSBAS and the NSBAS approach that is included in the Giant toolbox outperformed in terms of measurement point density and yielded 900K and 1300K points, respectively. Spatial patterns of ground deformation can be extracted easier from the results of these TSInSAR approaches.

All the algorithms performed similarly over urban areas. The deformation rate of spatial patterns inside the mining area are in agreement for Stamps/MTI, Mintpy-WSBAS and Giant-NSBAS approaches. Discrepancies between TSInSAR results can be found over low-medium coherent vegetated regions. Even though the Mintpy-WSBAS and Giant-NSBAS approaches yielded denser results their quality is questionable in vegetated regions. The deformation picture of the vegetated regions is similar for Stamps-PS and Stamps/MTI results, only. Thus, further investigation is required to identify and mitigate effects from potential noise sources such as the soil or/and vegetation moisture in forest, mountainous and crop field regions.

2.3.2.6   Cross-comparison

An RMSE metric is calculated for each pairwise combination of the results provided by the methods. For each pairwise combination, the results of one method are selected as a reference dataset and the results of the second method as a test dataset. RMSE metric is calculated for all the homologous points that are present in both results. Homologous points are selected based on the second step of the comparison methodology [2.3.2.2] using a 10m geographical distance criterion.
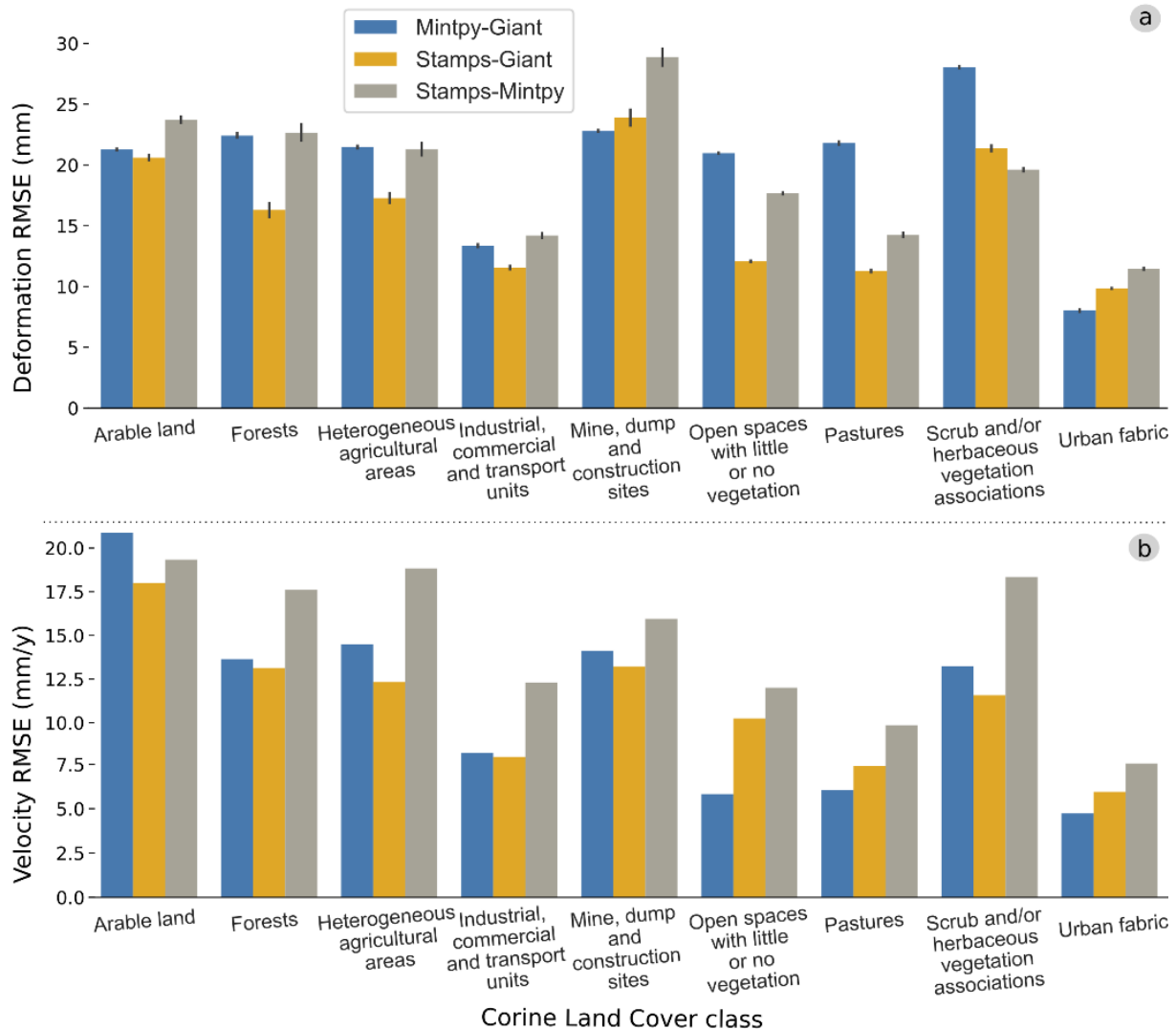
Figure 2.9 Deformation (a) and deformation rate (velocity) (b) RMSE values for each Corine land cover level-2 class in the AOI.

The deformation and deformation rate RMSE values for each Corine land cover level-2 class are presented in Figure 2.9. In general, the lowest RMSE values were found in industrial, commercial and transportation units, in open spaces with little or no vegetation, in pastures, and in urban fabric classes. This is expected due to their high coherence in respect with that of other land cover classes (Figure 2.8b). In land cover classes that include medium to high vegetation, the TSInSAR approaches showed the most controversial results. The different performance of the TSInSAR approaches in the vegetated areas, can be related with effects caused by seasonal variation in vegetation density, as well as, effects from variations in soil and vegetation moisture. Overall, among the three pairwise combinations (Figure 2.9), Stamps and Giant results showed the best agreement with each other. Stamps-Mintpy combination yielded the highest disagreements.
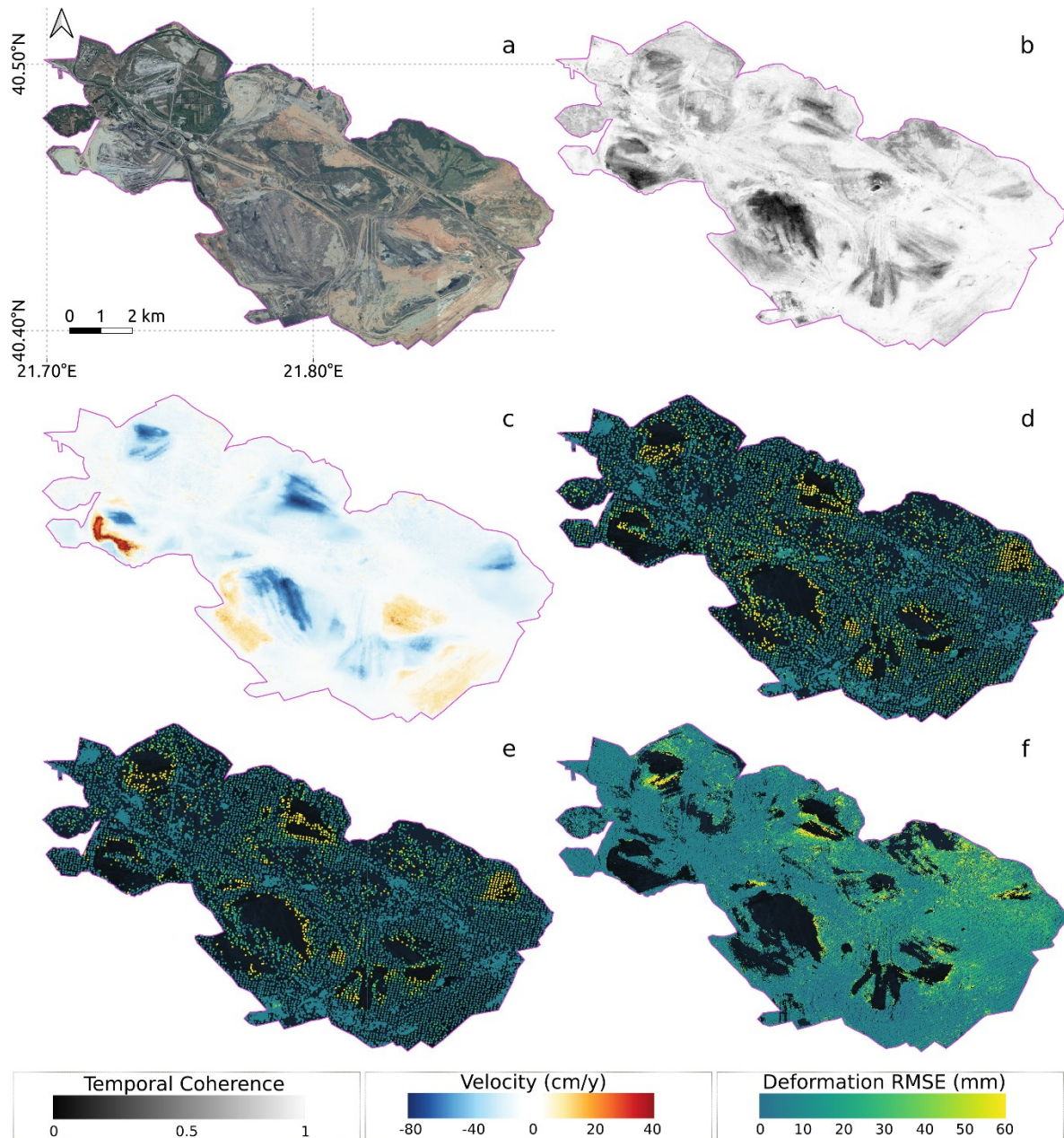
Figure 2.10 Cross-comparison of the deformation results in the mining region (denoted with purple polygon). a) Google earth optical image at 2018 b) Temporal coherence from Mintpy c) Average velocity (deformation rate) from Mintpy d) Stamps-Giant deformation RMSE map e) Stamps-Mintpy deformation RMSE map f) Mintpy-Giant deformation RMSE map.

In Figure 2.10, deformation RMSE maps for all available pairs between the used TSInSAR approaches for the corresponding comparison points are presented. TSInSAR approaches were not able to yield results in the high deformation mine regions, which present low temporal coherence (Figure 2.10b). These regions are observed with very high average deformation velocity in the result provided by Mintpy toolbox [44] (Figure 2.10c). In the borders of the high deformation regions, big deformation RMSE values, denoted with yellow color (Figure 2.10d, e, f) are observed. This occurs because of the low accuracy of the

results due to high temporal decorrelation. However, in the stable regions of the mine which are the brightest regions in Figure 2.10b, TSInSAR approaches yield comparable results, with low RMSEs. These regions are shown with purple color. The regions in the mine for which useful deformation results can be extracted are mainly high coherent regions such as abandoned mining regions, infrastructure and transportation network.

2.3.2.7   External comparison with in-situ levelling measurements

In this section, the comparison of TSInSAR results with levelling measurements is presented. The Mintpy processing was performed only from September of 2016 till June of 2018. The Giant-NSBAS deformation results present a smoothed behavior of the subsidence due to the inclusion of temporal functions (quadratic in this case) in the design matrix of the system. Mintpy and Stamps results were generated without the use of predefined temporal constraints.
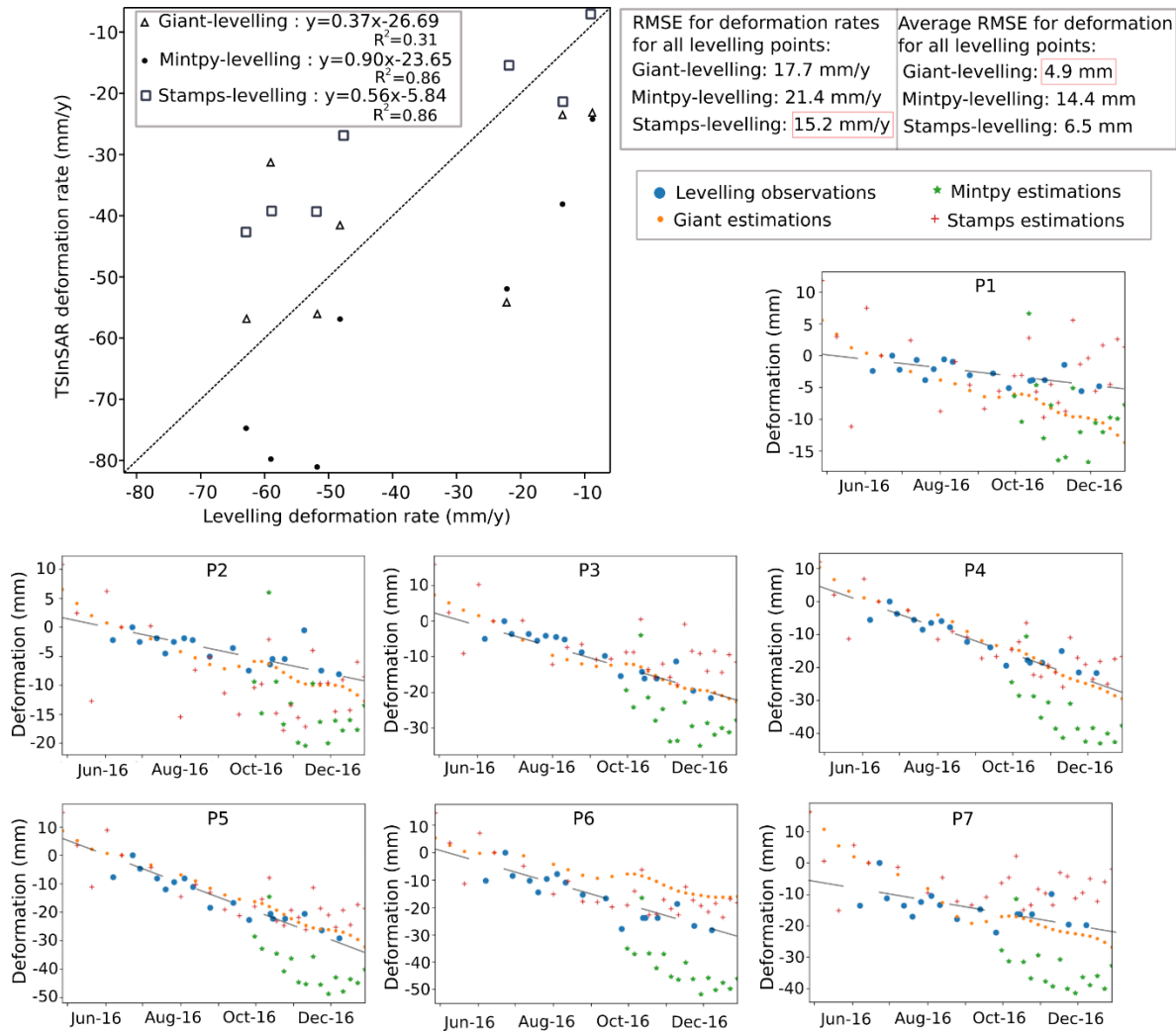
Figure 2.11 Comparison of TSInSAR accumulated displacement (subsidence) results with in-situ measurements for seven levelling points (position of the levelling pointσ given in Fig 2.6). Levelling values are projected in the LOS direction for the comparison.

Overall, all of the TSInSAR methods overestimated the subsidence rate according to the regression equations at top left side of Figure 2.11. Stamps and Mintpy regression equations for deformation rates presented the highest coefficients of determination (0.86). Stamps` approach was able to better capture the deformation rate information of the leveling points with an overall RMSE of 15.2 mm/year. Regarding the deformation information, Giant-NSBAS approach was able to better estimate the leveling observation with an overall RMSE of 5.9 mm. The RMSE values are calculated for the displacements in the LOS direction. In particular, leveling values are projected in the LOS direction by multiplying with the cosine of incidence angle of Sentinel-1 radiation, neglecting horizontal deformation, for the simplicity of validation.

The above results demonstrate that the subsidence behavior on the levelling points can be identified from all the selected open-source methodologies. The regional subsidence is possibly connected with mining operations. However, the interpretation of the deformation patterns is a complex task that requires

geological, hydrogeological and geotechnical information. In order to draw safe conclusions, the mining schedule activity may also be required. For the abovementioned reasons, the interpretation of the subsidence mechanism is omitted at the current stage of this study.

2.3.2.8   Discussion

In this session, the main advantages and limitations of each algorithm are discussed. Then, potential improvements for better monitoring of deformation in mining regions based on our case study results and other recent existing studies are proposed.

Table 2-1 Processing factors for the selected TSInSAR approaches

Algorithmic approach	Phase Unwrapping method	Multilooking	Measurement point selection factor
Giant-NSBAS	2D - space	suggested	spatial coherence
Mintpy-WSBAS	2D – space + corrections	suggested	spatial/temporal coherence, connected component unwrapping information
Stamps/MTI	2D - space + 1D time	-	Spatial deformation criteria

The performance of each TSInSAR approach is controlled by the following important factors (Table 2-1). The first factor is related to the unwrapping procedure of the interferometric phase. Mintpy and Giant software toolboxes require a stack of the differential unwrapped interferograms. In most cases, the unwrapping procedure is performed in space (2D) and for each interferograms separately. 2D unwrapping can produce errors that a sophisticated TSInSAR approach should be able to correct or mitigate their effects. Mintpy includes unwrapping error correction modules that can be employed and minimize the impact of the unwrapping errors in the displacement time series. NSBAS approach can mitigate the unwrapping errors by using predefined time functions. In our view, Stamps/MTI approach includes the most sophisticated unwrapping approach which exploits the spatiotemporal behavior of the wrapped phase. However, the 3D unwrapping inherently assumes the high temporal coherence of each point. This results in a network of points that will be sparser than that resulting from the 2D unwrapping procedures, as it is shown in Figure 2.8.

The second factor is related to the multilooking operation which is usually performed to improve the SNR with the cost of spatial resolution. The multilooking procedure is suggested using single-pixel SBAS techniques such as the Giant-NSBAS and Mintpy-WSBAS. On the other hand, multilooking can introduce noise to the resulting up-scaled pixel in case small scale deformation patterns exist or in case the study region is prone to geometric distortions. Adaptive multilooking approaches [46] can mitigate the errors from the multilooking operation. Additionally, multilooking procedure can also affect the performance of the unwrapping error correction algorithms that are based in the phase closure since the

assumption of conservative interferometric phase is violated [88]. Stamps/MTI approach is applied for the processing of full-resolution (without multilooking) interferograms which is critical for studying deformation in mining regions. However, full-resolution processing increases the processing cost which can be crucial for wide-coverage and/or large time series applications.

The third factor is related to the formulation and inversion of the interferogram network for each measurement point that takes place in each TSInSAR approach. Mintpy and Giant software packages require a stack of unwrapped differential interferograms in comparison with Stamps software which provides the functionality to form the unwrapped differential interferogram stack. Temporal and geometric baseline criteria should be defined to form the interferogram stack. For all the software packages, a quality check for each pixel in order to decide whether the pixel will be analyzed or will be discarded, is performed. In single-pixel SBAS techniques such as Giant-NSBAS and Mintpy-WSBAS for each pixel a separate interferogram network is formed.

In Giant-NSBAS approach, a thresholding technique based on spatial coherence is supported. This will result in the use of a subset of the initial interferograms stack for deformation estimation. The formed interferogram network can have isolated clusters of interferograms or to include only a small number of interferograms. In both cases, unstable inversion of ground deformation can be observed [89]. The sufficient number of interferograms that will lead to an unbiased estimation of deformation is also a common problem in modern sequential estimation techniques [90], [91]. The Giant-NSBAS approach requires a-priori knowledge of the temporal behavior of deformation in order to connect the isolated clusters in the network. In this study, based on the Stamps-PS results and the available levelling measurements the quadratic function is selected. It is important to state that the selection of the temporal function is a critical step for the Giant-NSBAS approach and this is possibly the main reason that Giant-NSBAS outperformed the most recent and sophisticated Mintpy-WSBAS approach.

In Mintpy-WSBAS approach, pixel selection criteria include the connected component information from the 2D unwrapping procedure and the temporal coherence information. The abovementioned approach exploits information about the temporal coherence and unwrapping quality and can ensure an unbiased deformation estimation [44]. Note that with this pixel selection strategy, after masking, the network inversion result is not sensitive to the few very low coherent interferograms in a redundant network, giving robust and consistent spatial coverage. On the other hand, in case of isolated islands in the interferograms network for high de-correlated regions such as mining regions, this approach can provide results at certain time periods. In this case study, during the start of 2016 only Sentinel-1A 12-day interferograms were available. However, after the launch of Sentinel-1B, using 6-day interferograms were formed and a fully connected interferograms network with great spatial coverage is constructed (Figure 2.8e).

Stamps/MTI approach identifies the measurement pixels based on their phase characteristics. This is performed by calculating the phase stability of each pixel by using the spatial correlation of the phases in the neighborhood. The high threshold value of the amplitude dispersion index (0.6 in this study) in the pixel selection strategy enables the selection of almost all PS and SDFP points [65]. One advantage of Stamps/MTI approach is the fact that this method is not based on the phase history of a single pixel but in phase similarity of the neighborhood assuming that deformation is spatially correlated. Moreover, accounting for spatial correlation significantly improves deformation estimates [36], [88]. This way there is no need to parameterize the deformation in time (performed in Giant) which can be challenging for temporally-variable deformation processes that are common in mining environments. Stamps/MTI approach employs an iterative band-pass adaptive filtering approach to estimate phase noise for each pixel in the interferogram stack. If the iterative filtering procedure doesn't converge then this pixel will be discarded. This will result in the inability of detecting isolated deformation phenomena, as well as, to extract information in cases of complex deformation at small spatial scales [87]. It can be critical in the deformation study of narrow regions inside mining regions such as transportation networks that remain coherent but their neighborhood experiences intense deformation or decorrelation. Another limitation of the Stamps/MTI approach that can be relevant for processing big SAR data is the processing cost.

In this paragraph, a discussion regarding the feasibility of TSInSAR approaches for deformation monitoring over opencast mining regions is presented. The main limitation of the TSInSAR approaches is related to the ambiguous nature of the wrapped interferometric observations. The following comes from the fact that a difference bigger than π between two subsequent differential phases cannot be converted to deformation unambiguously [92]. Moreover, in order to get a correct estimation of the unwrapped phase, the phase gradient between two adjacent pixels has to be less that π, which corresponds to $\lambda/4 \sim 1.4\ cm$ for Sentinel-1 [93]. For a 6-day interferometric stack over one year, the maximum detectable deformation rate is $\lambda/4\delta t \sim 85\ cm/year$. Longer wavelength interferometric data can yield higher maximum detectable deformation rate and should be considered in future studies. According to administration of the Mines Central Support Department of Public Power Corporation S.A.-Hellas [85], the displacement rates in the active mining regions of Ptolemaida-Florina opencast lignite mine are several meters per year. For this reason, the deformation values were not reasonable in the active mining regions. However, the administration found that TSInSAR displacement patterns (uplift or subsidence) (Figure 2.8) should be analyzed in combination with their excavation and dumping activities. Furthermore, TSInSAR results over abandoned mining regions, infrastructure, road network and neighbor regions were the most useful for the mining administration.

Based on the recent algorithmic advantages of TSInSAR techniques, there is a lot of room for improvements and advances for better monitoring of the deformation in mining regions. The main improvements according to our case study are related with the use of soil/vegetation moisture information that lead to high RMSE values (Figure 2.10). One other significant improvement is related with the parametrization of phase term due to DEM error in the inversion system. In the open-source toolboxes that are used in this study, the residual topographic phase due to DEM error is considered constant in time, fact that is not valid in active mining regions in case of large height changes. One possible solution to this problem can be a time varying parametrization of the DEM error phase term similar to the work of [94].

The proposed comparison scheme that is developed for this work can be useful for various communities and entities. Currently, many initiatives such as [95], [96] provide freely available geocoded unwrapped interferograms for most of the parts of the earth. Moreover, open source software tools such as Giant [41], Mintpy [44] and LiCSBAS [97] are selected to extract ground deformation information. To this point, we believe that the need of comparing and interpreting the differences of the results between several processing strategies is imperative. Moreover, identifying the differences can reveal the limitations of each methodology and the need for further corrections.

2.3.3   Exploring Driving Factors of Ground Deformation Using Wavelet Tools

2.3.3.1   Introduction

As we already discussed in the previous section, different TSInSAR methodologies can yield different ground deformation estimations (up to 5 mm/y over urban regions) even using the same SAR dataset (Figure 2.9). The motivation of this study is related to the complexity of the ground deformation extracted from interferometric SAR signals. In many cases, ground deformation information is hard to interpret and to use due to its complex nature and noisy interferometric SAR signals. Ground deformation complex patterns are a result of co-existing driving factors which can be related to natural and anthropogenic processes. The measured total ground deformation can be considered as a sum of several deformation components induced by several driving factors. Driving factors can be related with natural and anthropogenic processes such as tectonic activity, groundwater extraction etc. [98] successfully identified connections of natural driving factors (temperature and soil moisture) with ground deformation. In this case study, we present a wavelet-based approach to explore the connections of five potential driving factors (surface soil moisture, precipitation, lake water area variations, NDVI and ground temperature) with ground deformation results from TSInSAR.

2.3.3.2   Methodological framework and application

The study area covers a part of the Korisos basin, in Kastoria region, which is located in northwestern Greece (Figure 2.12). The area of the region of interest is about 95 square kms. The land cover of the study

area consists mainly of agricultural, mountainous regions and some villages. The methodological framework consists of four steps.
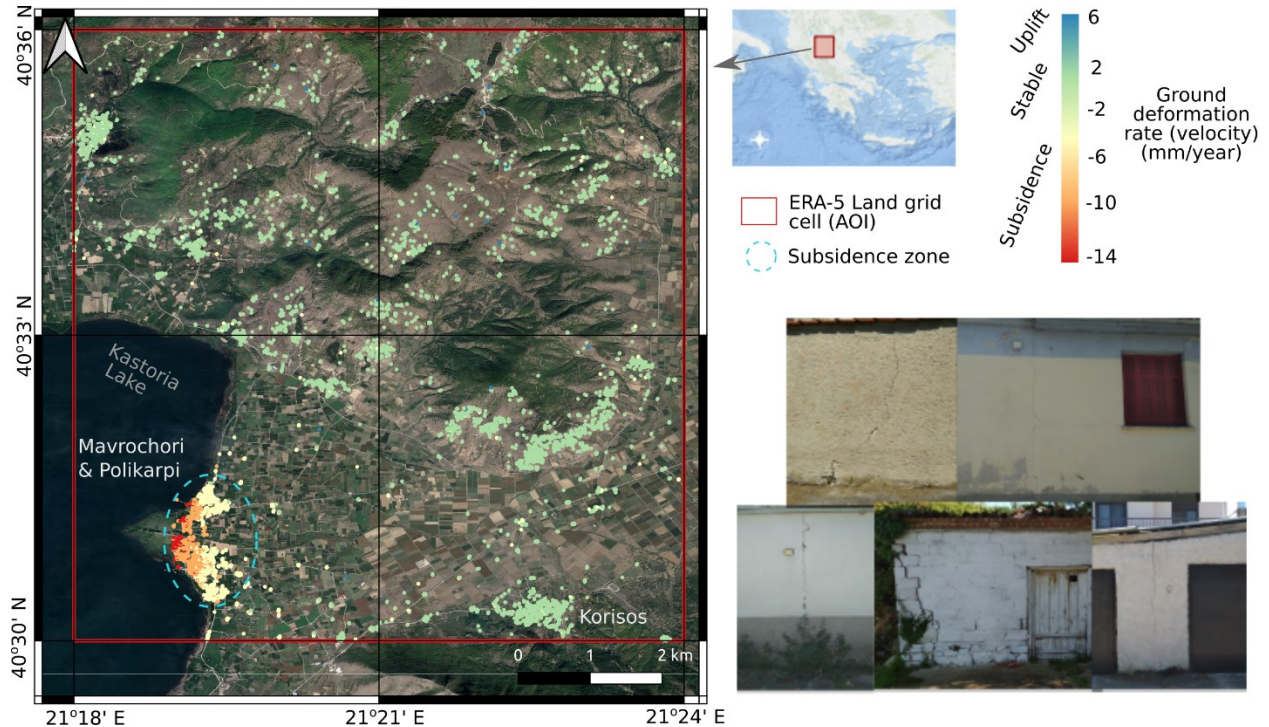
Figure 2.12 Area of interest (left), ground deformation rate information (left) and in-situ photographs of buildings located inside subsidence zone (bottom right).

Step 1: Ground deformation estimation using Stamps TSInSAR methodology

The ground deformation information time series, using a well-known Stamps-PS approach implemented in STaMPS toolbox [36], were extracted. A dataset of 193 single look complex C-band SAR images acquired by Sentinel-1A/B, from September of 2016 till December of 2019, have been processed. The preprocessing of the SAR dataset in order to be further processed by the Stamps-PS approach was performed using the ISCE software package [54]. As a reference stable point, a high coherent point located in Kastoria city outside of the AOI was selected. The first image of the SAR dataset was used as a temporal reference. The extraction of the topographic term from the interferograms was done using a photogrammetrically produced digital elevation model with ground pixel size of 5 m created in 2009, provided by KTIMATOLOGIO S.A. The calculated displacement time series was sampled every 6 days. The ground displacement values correspond to the direction between the sensor and the target (LOS). Only the points with high temporal coherence (>0.90) were used in this study. In Figure 2.12 we can identify the subsidence zone and subsidence effects from in-situ photographs taken in August 2020.
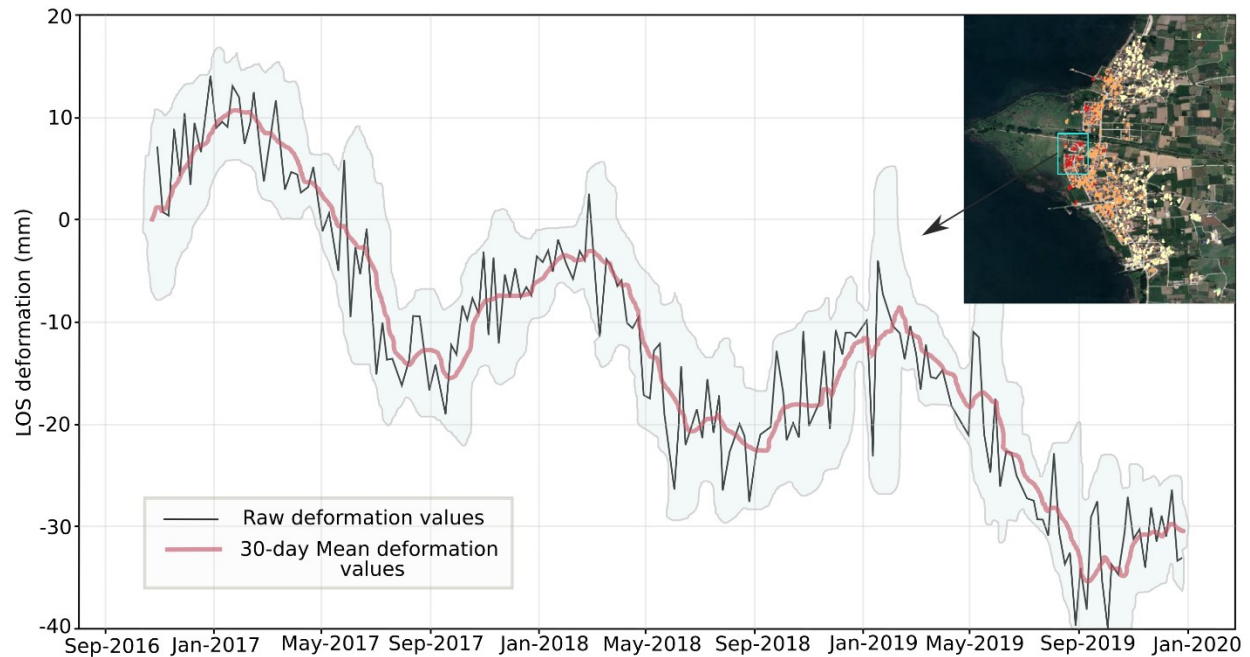
Figure 2.13 Ground deformation time series of a subsiding region in Mavrochori village, Kastoria, Greece.

In Figure 2.13, we can clearly identify the seasonal behaviour of ground deformation of a subsiding region over Mavrochori village. Based on our three and a half year analysis, we can say that a seasonal subsidence occurs from around March to September in an order of 2 cm and then we have the uplift period from September to the next March in an order of 1 cm. The subsidence behavior seems to have a significant impact on buildings according to our in-situ photographs (Figure 2.12).

Step 2: Clustering of ground deformation estimation

Next, a three-step clustering analysis of the ground deformation time series has been performed in order to reduce the volume of the data to be analysed (Figure 2.14). The t-distributed stochastic neighbor embedding (T-SNE) transformation [99] was applied in the ground deformation time series for all the points. Then using elbow and silhouette methods the optimal number of clusters was calculated [100]. Finally, a density-based spatial clustering of applications with noise (HDBSCAN) clustering [101] was applied to the transformed ground deformation data. This 3-step clustering analysis provided geographically well-separated clusters (Figure 2.15). Based on the average ground deformation time series, some of the regions appear to have stronger seasonal patterns than others.
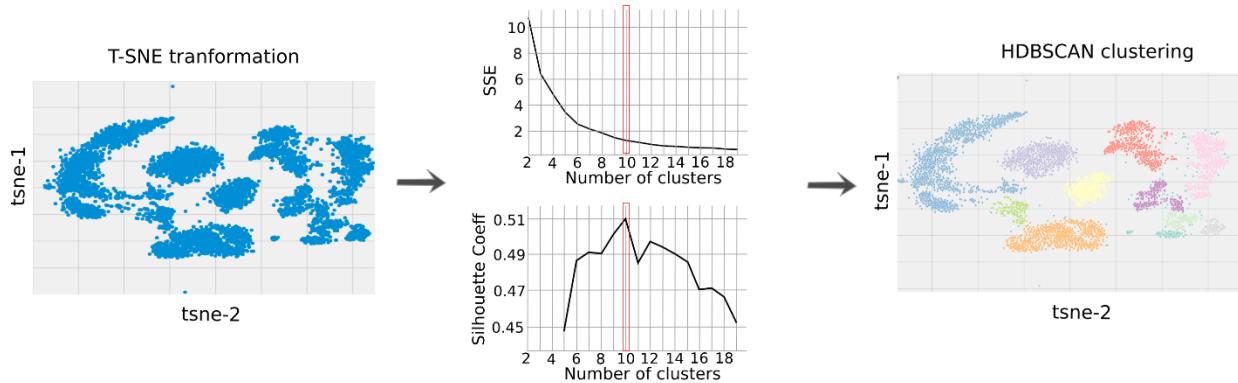
Figure 2.14 Three-step clustering analysis of ground deformation estimation
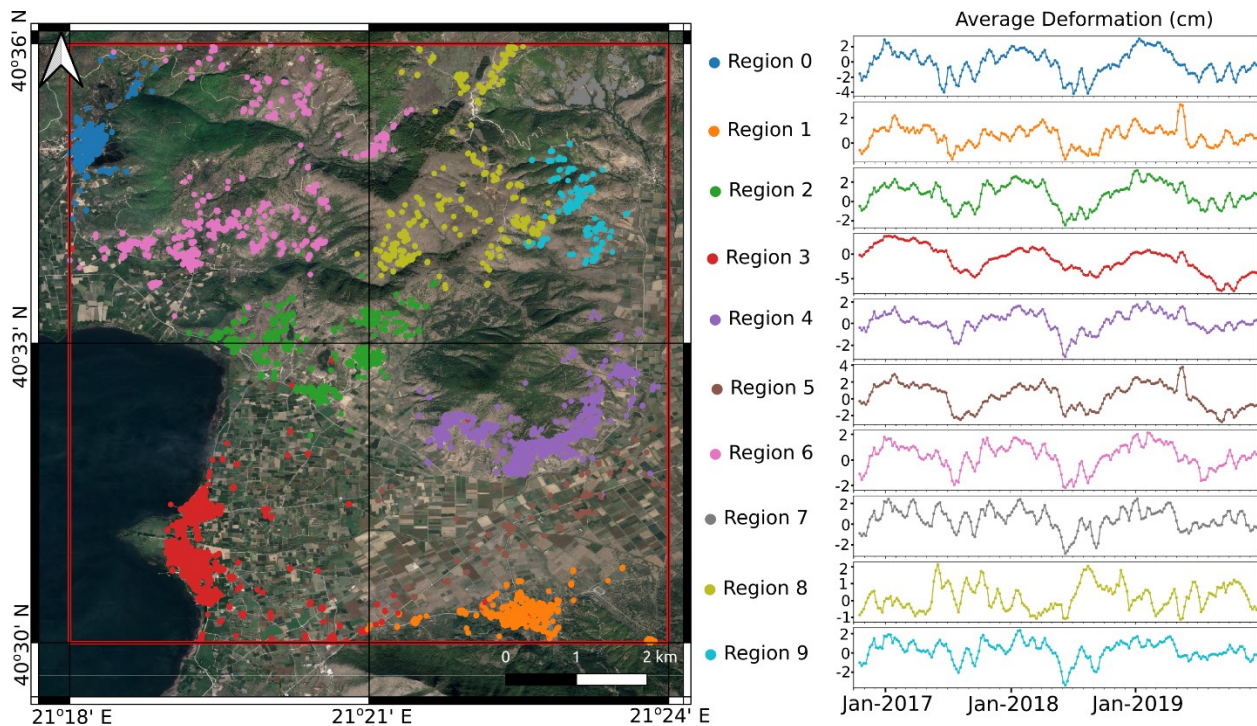
Figure 2.15 Clustered ground deformation results (left), Average deformation over time for each cluster/region

Step 3: Preprocessing of driving factor information

At a third stage, the preprocessing of the information related to the driving forces of the ground deformation is implemented. The driving factors that were considered consist of a) NDVI calculated from a stack of 250 Sentinel-2 acquisitions, b) the variations in lake water area by applying a thresholding approach on the intensity of the Sentinel-1 dataset, c) the temperature from ERA5-Land reanalysis dataset, d) the soil moisture from ERA5-Land reanalysis dataset and e) the total precipitation from ERA5-Land reanalysis dataset (Figure 2.16). It is important to state that the considered AOI covers a single ERA5-Land pixel, which means we have only a single value for ERA5-Land factors for the whole AOI in time.
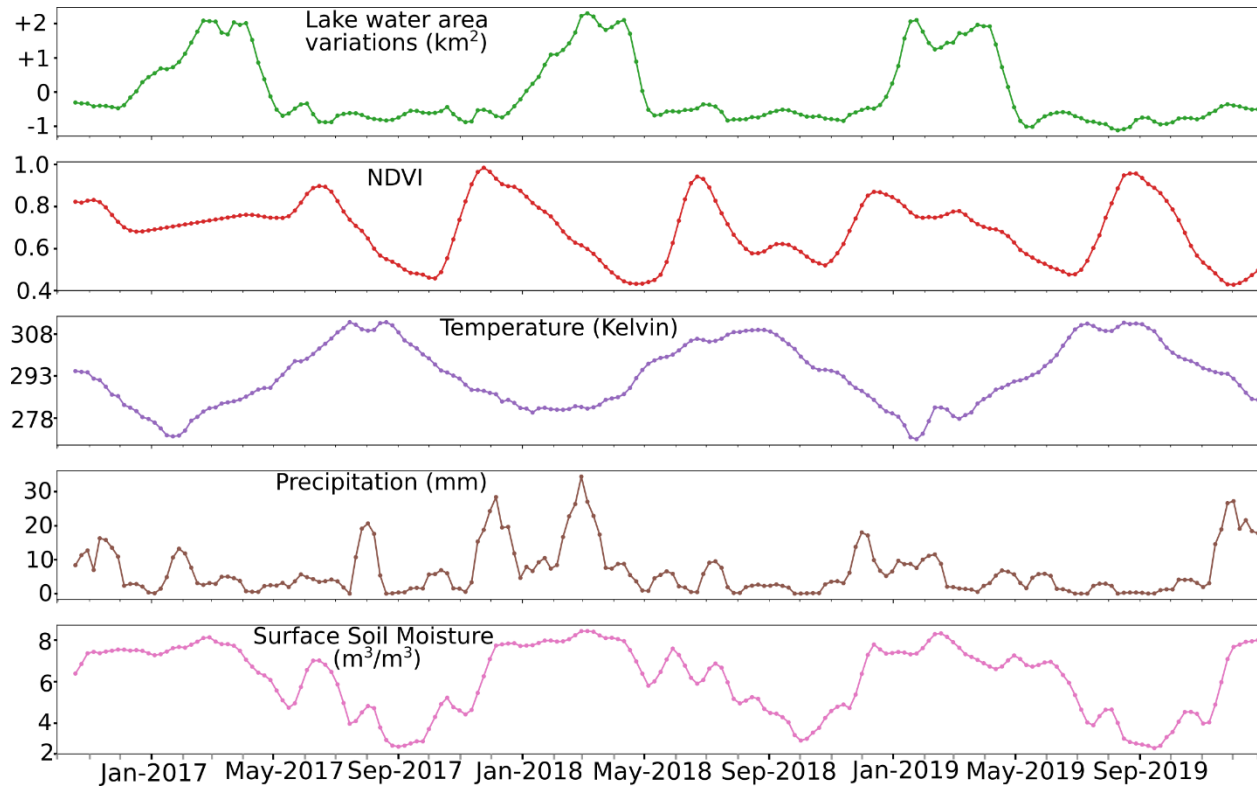
Figure 2.16 Considered potential driving factors of ground deformation over time.

Step 4: Cross wavelet analysis and results

In the fourth step, cross wavelet analysis (XWT) of the calculated ground deformation time series in conjunction with each one of the considered driving factors for each region/cluster was performed. The XWT analysis was performed to identify patterns at different time intervals and consists of two steps. The first step is the calculation of the continuous wavelet transform (CWT) of each time series to identify localized intermittent periodicities at time/frequency space. The second step is the multiplication of the CWT of the first time series with the complex conjugate of the CTW of each driven factor. Each XWT result is a 2-D representation of the absolute value and the phase of the complex number in the time-frequency space. The XWT analysis was performed using the freely available MATLAB wavelet tool [102]. The XWT results (Figure 2.17) of three regions (3, 5 and 6) are presented. The XWT results of all regions are provided at [103]. We encourage interested readers to have a look at [104] regarding the interpretation of XWT results. The following interpretations have been made.
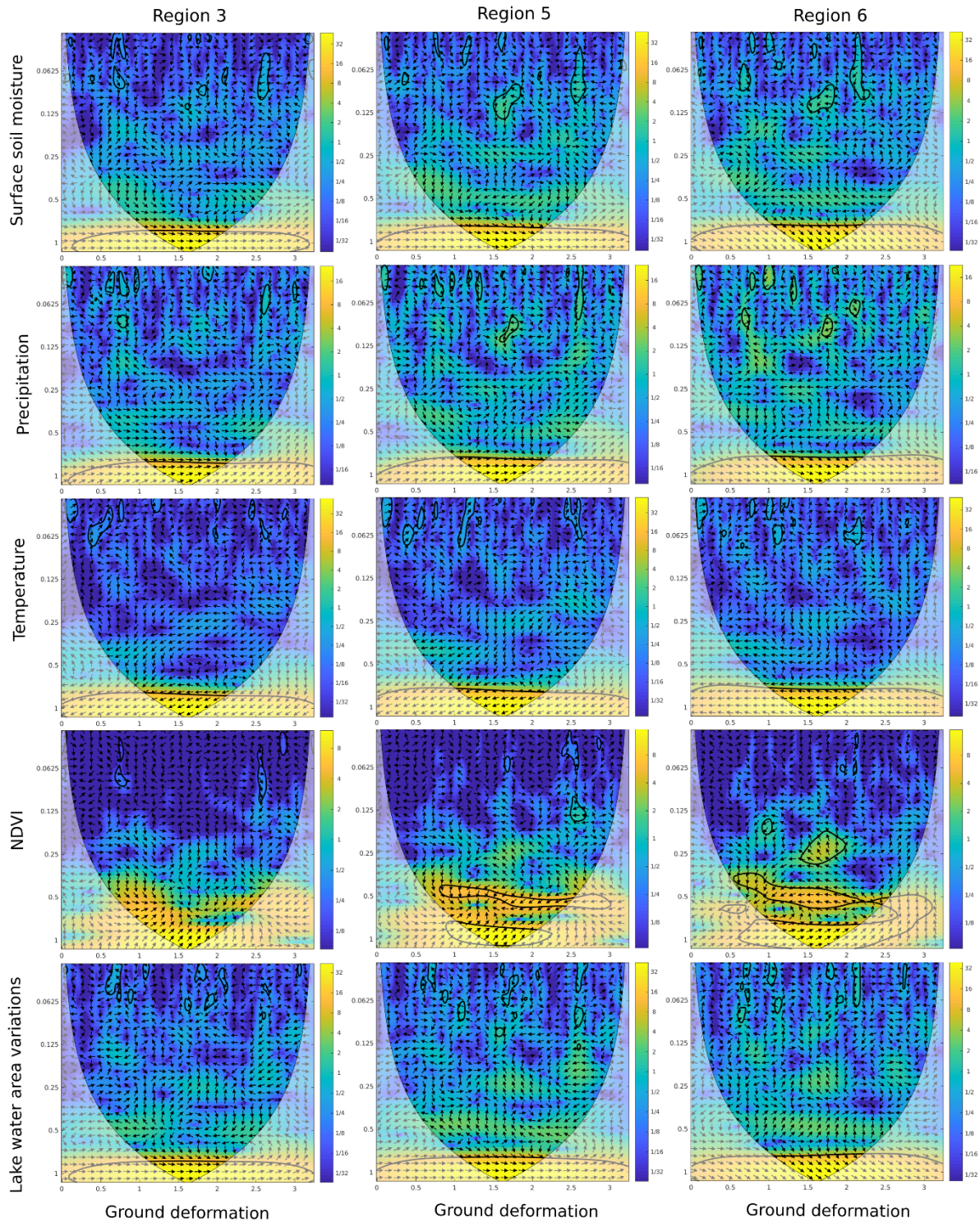
Figure 2.17 Cross wavelet results between driving factors and ground deformation for regions 3, 5 and 6.

- For all regions (3, 5 and 6) deformation and soil moisture are in phase. For region 6, deformation is leading precipitation for about 1.5 months. In regions 3 and 5 there is no time lag.

- For all regions (3, 5 and 6) deformation and precipitation are in phase. For region 6, deformation is leading precipitation for about 1 month for 1-year period. For regions 3 and 5 there is no time lag.

- For all regions (3, 5 and 6) deformation and temperature have an anti-phase relationship for 1-year period. For agricultural regions (3 and 5) deformation is leading temperature for about one month. We believe that this particular lag can be potentially related to the crop calendar. For region 6, no time lag was observed.

- For regions 5 and 6 deformation and NDVI were in-phase where NDVI is leading deformation about 1-2 months for 1-year period. For region 5, deformation and NDVI were anti-phase with NDVI leading deformation about 0.5-1 months for 6-month period. For region 6, deformation and NDVI were anti-phase where deformation is leading NDVI about 0.5-1 months for 6-month period. We can identify that results between different time periods are contradictory possible due to different agricultural actions at a field level. For region 3 we cannot draw any conclusions because the majority of the points are not located over/close to vegetated areas.

- Regions 3 and 5 deformation and lake water variations are in phase at 1-year period with no time lag. For region 6, deformation is leading lake water variations by around 1.5 months.

2.3.3.3   Discussion and conclusions

In this study, we presented the capabilities of the proposed wavelet-based approach which was able to reveal the different interactions of several driving factors to the ground deformation. We believe that the proposed methodology is a robust and efficient way to explore and analyse the impact of multiple and co-existing potential driving factors to a massive volume of ground deformation information.

A subsidence phenomenon with seasonal behaviour is identified over Mavrochori and Polikarpi villages. In particular, a subsiding trend from March to September is identified (Figure 2.13). Based on the wavelet analysis, the deformation information of regions 3 and 5 presented the highest agreement (in-phase) with no time lag with the variations of water cycle. The water cycle variations are captured via the following driving factors: a) lake water variations, b) precipitation and c) soil moisture. This is an important result given that the main deformation source of the study area is closely related to groundwater extraction activities for irrigation and domestic use purposes during the dry season from May to September [105]. We strongly believe that groundwater information is an essential factor of the water cycle that should be studied. Studying ground deformation can provide information in order to construct a better water management plan which is essential to ensure water sustainability and food security.

Regarding the relationship between ground deformation and vegetation variations, we observed different behaviour at 6-month and 12-month span. In particular, ground deformation and NDVI was found to have an anti-phase relationship for a 6-month period. Over agricultural regions, ground deformation is leading (0.5-1 month) NDVI. Over the regions with natural vegetation no time lags are identified. The contradictory results between deformation and NDVI can be related to the different agricultural actions on each field over the agricultural regions of the AOI. Further investigation is required to draw a safe conclusion.

Ground deformation and temperature was found to have an anti-phase relationship for a 12-month period for all regions of that AOI. Over agricultural regions, deformation is leading temperature by about one month, in comparison with all the other regions, no time lag was identified. We believe that the observed time lag over agricultural regions can be related with the crop calendar and agricultural practices. However, further investigation is required mainly due to the fact that a single temperature value from the ERA5-land dataset is used for this study. We generally believe that temperature datasets with higher spatial resolution (e.g. Landsat-8/9, ECOSTRESS) can potentially reveal unobserved relationships.

The proposed methodology can be used as an exploration tool to improve the interpretation and the usability of ground deformation from interferometric SAR signals via exploring the links with predefined possible driving deformation factors. We consider the exploration of the driving factors of the ground deformations a critical step towards applying new methodologies such as data-driven approaches.

2.4   Interferon - Interferometric Time Series for Deformation

A software package (Interferon) for ground deformation estimation was developed based on the published and unpublished work. Interferon is a python software package able to provide ground deformation estimation using Sentinel-1 datasets. Currently, Interferon is an in-house software but will be released as an open-source software under GPLv3 license in the near future. The main features of Interferon are:

Innovation: Interferon includes implementations of state-of-the-art TSInSAR methodological advances. It encourages collaboration of ideas and sharing of resources and promotes research initiatives.

Usability: Interferon is easy to use and learn. It can be utilized as a learning medium, for educational purposes.

Continuity: Interferon is a cost-effective solution because it allows people to save time and effort by leveraging existing code. Contributors can boost the scalability and the sustainability of the software.

Freedom: Interferon is developed in open-source language (Python) in order to ensure its use at no cost. In particular, many functionalities from MATLAB-based software (e.g. Stamps) were translated to Python.

Interferon includes implementation of several methodological steps for ground deformation estimation by utilizing PS and DS. Interferon requires as input a coregistrated SLC stack and outputs a point vector file with ground deformation time series. A brief description of these steps is provided.

1. Calibration of SAR amplitude information [36]
2. Identification of PS candidates using amplitude dispersion thresholding [31]
3. Identification of similar neighbors for every pixel that is not a PS candidate. The identification is based on non-parametric statistical test (e.g. Kolmogorov-Smirnov, Andersen-Darling) on temporal behavior of SAR amplitude. [46]
4. Identification of DS candidates based on temporal coherence thresholding and phase linking of DS phase information to generate PS-like phases [49], [106]
5. Estimate of phase noise of PS/DS candidates and dropping of noisy PS/DS scatterers [65]
6. Construction of graph using PS/DS time series information [107].
7. Outlier detection and removal of PS/DS candidates based on graph theory [34], [108].
8. PS/DS spatiotemporal phase unwrapping [29].
9. Calculation and subtraction of spatially correlated DEM error [107].
10. Estimation and subtraction of spatially correlated noise using kriging [107].

2.5 Conclusions

In this chapter the work related to TSInSAR methodologies was presented. First, several of multiple track/orbit TSInSAR (Giant-NSBAS) results are combined to calculate vertical and horizontal ground deformation. The estimated vertical component of ground deformation had centimetric accuracy in comparison with in-situ leveling data. Then, a detailed performance analysis of several TSInSAR methodologies (Stamps/MTI, Giant-NSBAS, Mintpy-WSBAS) is provided. All the considered TSInSAR methods generated similar spatial patterns of ground deformation over a region with high complexity of ground deformation patterns (mining region). Land cover categories that have stable scattering properties (e.g. urban areas, rocks) presented the best accuracies (RMSE of deformation rate: 5 mm/y). Disagreements between the results of the selected algorithmic approaches were found in the vegetated areas. A thorough discussion regarding the positive and negative sides of each TSInSAR approach is presented. Next, a wavelet-based approach is introduced which was able to explore the relationships between five driving factors (surface soil moisture, precipitation, lake water area variations, NDVI and ground temperature) and ground deformation results from TSInSAR. Finally, Inteferon software package is developed where, most of the knowledge acquired and lessons learned can be found.

3   SOIL MOISTURE ESTIMATION USING INSAR DATA

In Chapter 3, the work related to soil moisture estimation from InSAR observables (interferometric coherence and phase closure) is presented. In section 3.1, we provide an introduction and background information regarding soil moisture estimation from InSAR observables. In section 3.2, we introduce our proposed methodological framework that is focused on arid regions. In section 3.3, the study area and the datasets of the case study on an arid region located at California, USA are described. In section 3.4, the soil moisture estimation and their accuracy assessment is presented. In section 3.5, the main benefits and limitations of the proposed methodology are highlighted. Finally, in section 3.6 the conclusions of the work related to soil moisture estimation from InSAR observables are provided.

3.1   Background and Introduction

Soil moisture is considered a crucial environmental variable related to water, energy, and carbon cycles [109]. In arid and semi-arid environments, which cover around 40% of global terrestrial surface, soil moisture exhibits significant spatio-temporal variability [110] and is a critical input to weather, climate, drought and flood modelling and forecasting [111]. In order to study the complex patterns of soil moisture, methodologies and surface soil moisture (SSM) products that exploit satellite earth observation data have been developed [112], [113]. However, the challenge of an operational soil moisture product with high spatial resolution and high spatiotemporal coverage remains elusive [114]. Current and upcoming satellite missions offer opportunities to bridge the gap between soil moisture products and user/application requirements. SAR missions which can provide all-weather, day and night, global, and data with extensive and continuous coverage, have a critical role for high-resolution satellite SSM applications [114]. Recent studies [115]–[117] highlight the great potential of interferometric synthetic aperture radar (InSAR) time series for high-resolution and accurate SSM mapping over arid environments.

Time series InSAR is a well-established technique to estimate ground surface deformation [44]. In order to extract deformation signals, other factors that can decorrelate SAR signals such as residual topography, atmospheric delay, vegetation and soil moisture variations have to be compensated [118]. In most of the ground deformation studies, in order to overcome limitations associated with decorrelation, a methodology based on phase-stable point scatterers technique and/or distributed scatterers is implemented [36], [46], [51]. In those studies, soil moisture contributions are treated as noise and mitigated by applying filtering approaches. However, due to the observed relationship between SSM and InSAR observations, methodological approaches able to estimate SSM from InSAR phase and coherence information have been developed [111], [115]–[117], [119], [120].

The InSAR observables that are mainly used for SSM estimation are interferometric phase, coherence magnitude and phase closure. De Zan et al., (2014) proposed an analytical solution for bare lands

based on plane waves and the Born approximation that models soil moisture as vertical complex wavenumbers and successively interferometric observables from L-band airborne SAR data. Coherence and phase closure observables were inverted to estimate soil moisture. Zwieback et al., (2015) assessed the relationship of the three aforementioned observables with the soil moisture using regression tools, for airborne and UAV L-band SAR. A positive relationship with increased sensitivity between soil moisture and interferometric phase, compared to the two other observables, was reported. Moreover, changes in soil moisture were found to be associated with a loss of coherence. Zwieback et al., (2017) highlighted the importance of phase referencing in order to estimate soil moisture. Phase referencing was found challenging using only InSAR observations in cases where displacement and soil moisture variations are correlated. De Zan and Gomba, (2018) used satellite L-band data and estimated successfully soil moisture at sub-kilometer scale by inverting phase closures constrained by coherence information. In this study, the need for evaluating the potential of phase closure for soil moisture estimation in the context of an operational approach and in shorter wavelengths was highlighted. Michaelides, (2020) introduced a partially correlated interferometric model (PCIM) that considers the statistical properties of surface roughness and volume scattering. The PCIM model yields a closer match to the simulation results than De Zan`s model [119]. Bürgi and Lohman, (2021); Jordan et al., (2020); Scott et al., (2017) introduced approaches able to generate accurate SSM proxies after precipitation events from InSAR coherence over arid and hyper-arid environments. Mira et al., (2022) proposed a two-step SSM estimation method for bare soils that uses C-band (Sentinel-1) SAR data. In the first step, the atmospherically corrected interferometric phase and coherence were calculated by exploiting nearby Global Navigation Satellite System (GNNS) observations. In the second step, the De Zan`s model was inverted and SSM were estimated with high accuracy (RMSE: 0.04 m^3/m^3) over bare soils.

To the best of our knowledge, a limited amount of existing studies [115], [117], [123] are based on C-band InSAR datasets. We believe that the continuously increasing volume of C-band, mainly due to the Sentinel-1 constellation, offers a great opportunity for exploring the potential of C-band data for SSM estimation. In this study, we developed a SSM estimation methodology for arid environments based on VV polarized Sentinel-1 InSAR time series. The implementation of the proposed approach is implemented and provided as an open-source software toolbox (INSAR4SM) available at www.github.com/kleok/INSAR4SM under GPLv3 license. The main research questions that we will try to address are:

- Can we improve the quality of InSAR observables that will be used for soil moisture estimation?
- Can we resolve coherence ambiguity which is reported at [121], to improve soil moisture estimation?

- Can we provide a more robust inversion scheme for soil moisture estimation from InSAR observables?

3.2 Methodology

The required inputs for our methodology are a co-registered SLC stack and a meteorological dataset (precipitation, snow and temperature) for the same area and time considered. Currently, SLC stacks that are prepared using ISCE TopStack functionality [86] are supported by the INSAR4SM tool. The main methodological steps (Figure 3.1) are described as follows:

Step 1: Identification of driest SAR acquisition.

Over arid regions, we assume that the majority of the selected SAR acquisitions correspond to low SSM conditions [124]. Using the input meteorological dataset, we select the SAR acquisitions that are ice/snow free and are not related to precipitation activity. The driest SAR acquisition is selected as the one that yields the highest mean coherence in respect to the other selected images.

Step 2: Coherence and phase closure calculation.

First, a SSM estimation grid is constructed according to specified grid size (e.g. 250 m). For each SSM grid cell, a DS is constructed from SLC SAR pixels that have similar intensity temporal patterns. A DS is a group of SLC SAR pixels that has lower noise in respect with a single SLC SAR pixel [46]. The selection of those SLC SAR pixels is performed by using the non-parametric statistical Kolmogorov-Smirnov test [46]. Then, the matrix Z^{pxl} is formed by using the l selected SLC SAR pixels at p SAR acquisitions. We assume that the statistically homogeneous region of each SSM grid cell that consists of l selected SLC SAR pixels, follow a zero-mean complex circular Gaussian model with sample covariance matrix C [46], [49], [90] that can be expressed by the following formula:

$$C = \frac{ZZ^H}{\sqrt{\|Z\|^2 (\|Z\|^2)^T}}$$

(3.1)

Where, $.^H$ indicates the Hermitian conjugation, $\|Z\|$ gives the row-wise Euclidean norm of the matrix Z. Power and division operations are elementwise. According to [49], an element of C at SAR acquisitions n, m can be decomposed/considered as:

$$C_{nm} = \gamma_{nm} I_{nm}$$

(3.2)

$$I_{nm} = e^{j\varphi_{nm}} \tag{3.3}$$

Where, γ is the magnitude of the interferometric coherence, I the complex interferometric value and φ the interferometric phase over the region that is covered by the l selected SLC SAR pixels. Imaginary number is denoted with j. Phase closure Ξ for n, m, k SAR acquisitions according to [121] can be expressed by the following formula:

$$\Xi_{nmk} = \arg(I_{nm}I_{mk}I_{kn}) \tag{3.4}$$

Step 3: Identification of "dry" SAR acquisitions.

For each SSM grid cell, the ordering of SAR acquisitions based on SSM levels is calculated by exploiting the magnitude of the interferometric coherence and SAR backscattering. The ordering algorithm was based on the hypothesis that similar SSM levels yield high coherence values and different SSM levels yield low coherence values [115], [121]. The magnitude of the interferometric coherence between SAR acquisitions can be affected by several factors such as vegetation changes, sediment transport, soil moisture changes or other types of changes that alter the composition of scatterers within a resolution pixel [125]. It is important to state that the contribution of vegetation on coherence losses is assumed zero because of the low vegetation coverage of arid regions [115]. This allows us to exploit the coherence information for ordering SAR acquisitions based on their SSM levels.

The identified driest acquisition from Step 1 is selected as a starting point. Then, based on the coherence values of the remaining acquisitions in respect to the driest acquisition we order every other SAR acquisition. Besides the coherence-based ordering, we calculate a backscattering-based ordering by assuming the positive monotonic relationship between SSM and SAR backscattering levels [126]. In the end, the best ordering is considered the one that yields the steepest negative slope of coherence with respect to the distance between the temporal positions of ordered SAR acquisitions [121]. After the ordering, the 30% of the driest SAR acquisitions are considered to have low SSM and characterized as "dry". The abovementioned statement is considered valid, over arid regions and using a considerable length of SAR time series [124].

Step 4: Calculation of coherence due to SSM variations.

In this step, for each SSM grid cell we calculate the coherence due to SSM variations. Coherence is related to several decorrelation sources with the following product form [45], [111], [115]:

$$\gamma = \gamma_0 \gamma_p \gamma_{sm} \tag{3.5}$$

Where, γ_O is the background coherence due to surface roughness, slope, etc; γ_P is the permanent coherence loss due to permanent changes due to precipitation events, erosion, deposition; and γ_{sm} is the coherence loss due to SSM changes. The abovementioned expression is considered valid given that we operate over arid environments and for SAR stack with small spatial baseline separation [115].

Over arid regions, the variations of low vegetation cover are considered to have negligible impact in coherence and small perpendicular baselines mitigate geometric decorrelation that cause coherence loss. Coherence loss due to SSM over "dry" SAR acquisitions is assumed to be negligible ($\gamma_{sm} = 1$). Then, γ_O and γ_P are estimated by considering the exponential model introduced by [127] only over the coherence values calculated by the "dry" SAR acquisitions γ_{dry}.

$$\gamma_{dry} = (\gamma_O - \gamma_P)e^{-t/\tau} + \gamma_P \tag{3.6}$$

Where, τ is the decorrelation rate and t the time span between SAR acquisitions. After fitting the model for each SSM grid cell we have a single γ_O value, a single τ value and a temporal function of γ_p. Then, for each combination of SAR acquisitions we calculate γ_{sm}.

Step 5: SSM inversion.

For each SSM grid cell, an inversion of the analytical interferometric model proposed by [119] is performed. The selected model provides a direct relationship between the SSM change and the coherence and phase closure information. The modelled complex interferometric value between n, m SAR acquisitions reported in De Zan et al., (2014) is:

$$I_{nm}^{model} = \frac{1}{2j(k_n - k_m^*)} \tag{3.7}$$

Where, k is the complex wavenumber in the vertical direction and j is the imaginary number. The model assumes that soil moisture variations cause different propagation of the SAR signals that can be described by the complex wavenumbers in the vertical direction. The soil is modeled as a uniform lossy dielectric layer and k is described by the formula [121]:

$$k = \sqrt{\omega^2 \mu \varepsilon} \tag{3.8}$$

Where, ω is the angular frequency; μ is the magnetic permeability; and ε the dielectric permittivity. Dielectric permittivity is related to soil moisture and is given by Hallikainen's empirical model [128]. The following cost function L for all n, m, k SAR acquisitions is considered:

$$L = \sum_{n<m<k} \left| \Xi_{nmk} - \Xi_{nmk}^{model} \right|_{2\pi}^{2}$$
$$+ \sum_{n<m<k} \left(\left| \gamma_{sm,nm} - \gamma_{nm}^{model} \right| + \left| \gamma_{sm,mk} - \gamma_{mk}^{model} \right| + \left| \gamma_{sm,nk} - \gamma_{nk}^{model} \right| \right)^{2} \quad (3.9)$$

Where, Ξ is the observed phase closure; Ξ^{model} is the modelled phase closure based on De Zan`s model; $\gamma_{sm}$ the coherence due to soil moisture variations; and $\gamma^{model}$ the modelled coherence based on De Zan`s model.

The Sequential Least SQuares Programming (SLSQP) solver [129] is selected due to its robust and fast performance. In our implementation, the SSM value of the driest SAR acquisition identified at step 1 is set to 0.03 m³/m³, which we assume is a reasonable value for arid environments. Next, the computed coherence due to soil moisture variations (output of step 4) over "dry" SAR acquisitions (output of step 3) was exploited to update the sorting of SAR acquisitions. Then, starting from the driest SAR acquisition, the initial SSM values of all other SAR acquisitions are calculated by the following formula which is based on Eq. 4 in [115].

$$sm_n = \frac{sm_m}{\gamma_{sm,nm}}, \qquad if \; sm_n < sm_m \qquad (3.10)$$

Where, n, m are indices for SAR acquisitions and sm the SSM level of a SAR acquisition.

The inversion procedure was constrained in order to yield the SSM value of the driest SAR acquisition with an upper limit equal to the predefined SSM value of the driest SAR acquisition (0.03 m³/m³). The method may produce a soil moisture offset that is due to an error in the considered initial soil moisture value of the driest SAR acquisition.
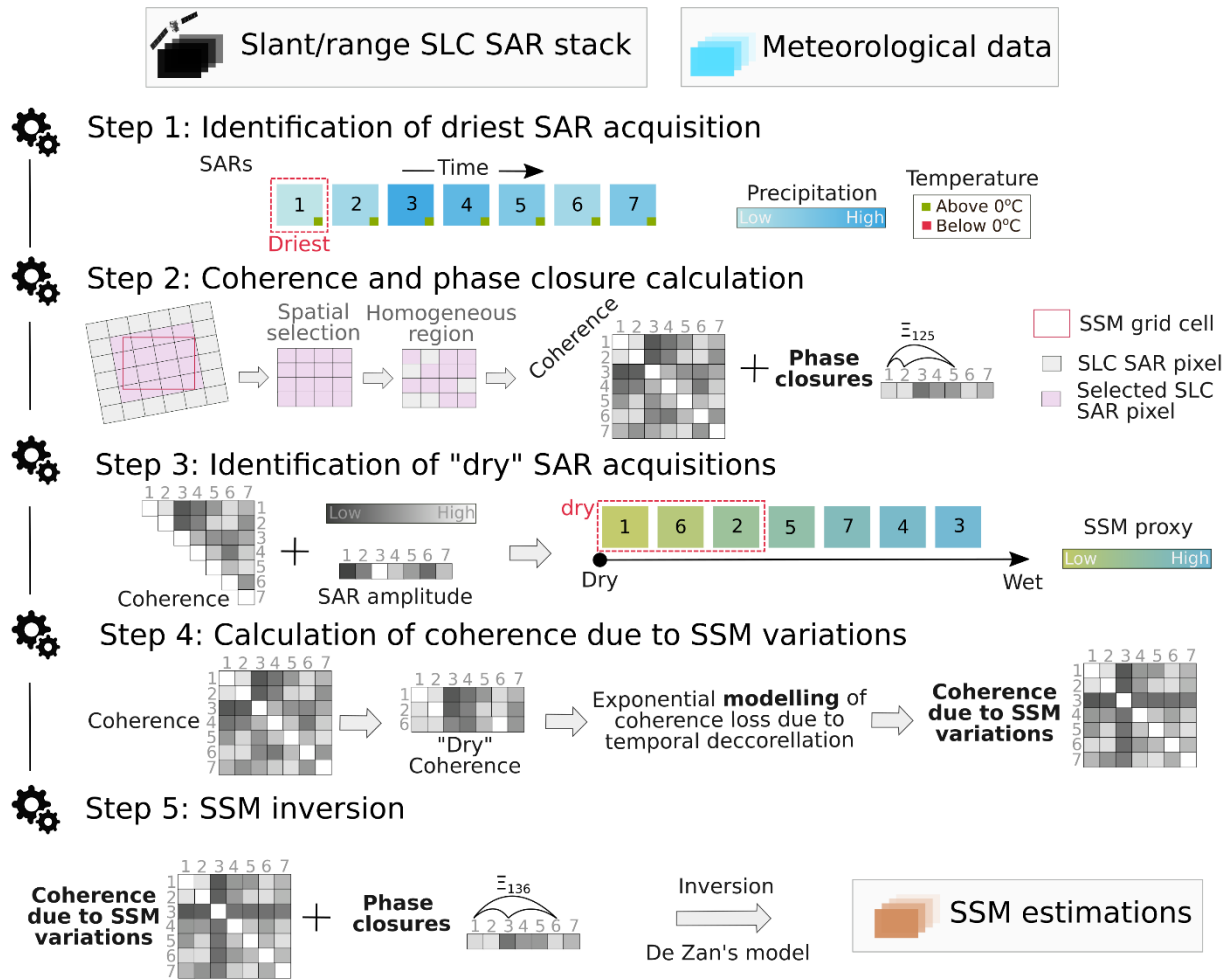
Figure 3.1 Methodological steps of the proposed approach

3.3 Application

The proposed methodology is applied to an arid region located at California, USA (Figure 3.2). In particular, the area of interest is located in the central Sonoran desert, in the Lower Colorado River Basin, and has low annual rainfall (50–300 mm) and high temperatures [130]. The soil type of the area of interest is Orita gravelly fine sandy loam with low runoff rates and high percolation rates [131]. Regarding the land cover of the area of interest, the vegetation of the area of interest has low coverage and consists mainly of creosote bush (Larrea divaricata) and white bursage (Ambrosia dermosa) [130]. Moreover, anthropogenic surfaces such as highways, gravel roads, solar farms and agricultural fields can be found. The area of interest has broad, nearly flat valley bottoms to high rocky mountain peaks.
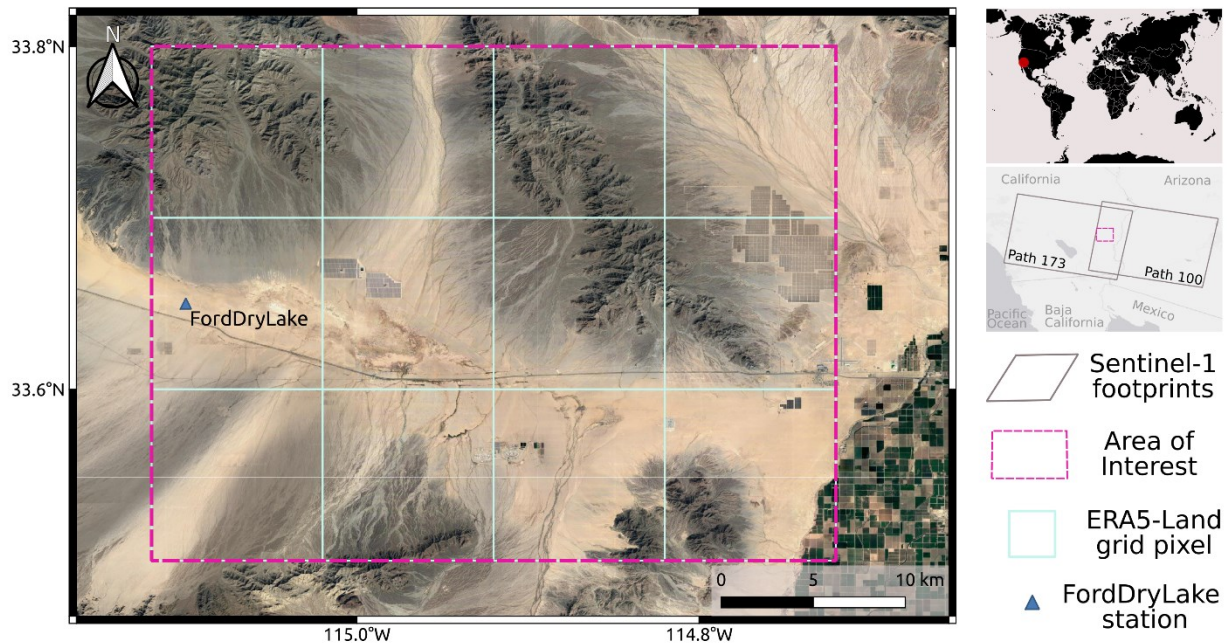
Figure 3.2 Area of interest and ground footprint of datasets used

In the presented application, frequent (12-day repeats) Sentinel-1 (C-band) and ERA5-Land reanalysis meteorological data [132] were used for estimating soil moisture in top 5 cm for bare soils over the area of interest. In our area of interest data from three orbits (173, 100, 166) of Sentinel-1 can be retrieved. For this study, we selected 23 (orbit 173) and 22 (orbit 100) Sentinel-1 acquisitions acquired at about 14:30 UTC from July 2018 to March 2019. We dropped SAR acquisitions from orbit 166 because the acquisition time was during early morning (04:30 UTC). This decision is made because the thin water layer due to potential dew during the mornings affects the SAR signal and cannot be captured by soil moisture sensors used for validation [133]. Precipitation and temperature data from ERA5-Land model were used for identifying the driest SAR acquisition. For validation purposes in-situ soil moisture observations and soil moisture ERA5 model data were exploited. In-situ soil moisture measurements at depth of 5 cm from FordDryLake station of the SCAN network [134] that belongs to ISMN network [135], [136] were used for assessing the performance of the proposed methodology. ERA5-Land reanalysis soil moisture data at depth of 0-7 cm were also used for quantitative assessment.

3.4   Results and accuracy assessment

In Figure 3.3, the precipitation and soil moisture observations from the FordDryLake station are presented. Moreover, the SSM estimations at six selected time points on a 250 m SSM grid using the proposed methodology are presented. The 250 m SSM grid size was decided because it yielded the most accurate results after experimentation at the FordDryLake station. Based on the results, we can identify that

valley regions experience more SSM variation in respect with the mountainous regions. Moreover, some regions tend to have higher SSM values in respect to other regions. For time points A, B and D in Figure 3.3, we observe that after rain events the SSM is increasing. The decay of SSM between time points (B to C) that we don't have rain events can also be observed. Based on the SSM estimations at time points E and F, we can also observe the temporal evolution of the SSM when no major rain events took place.
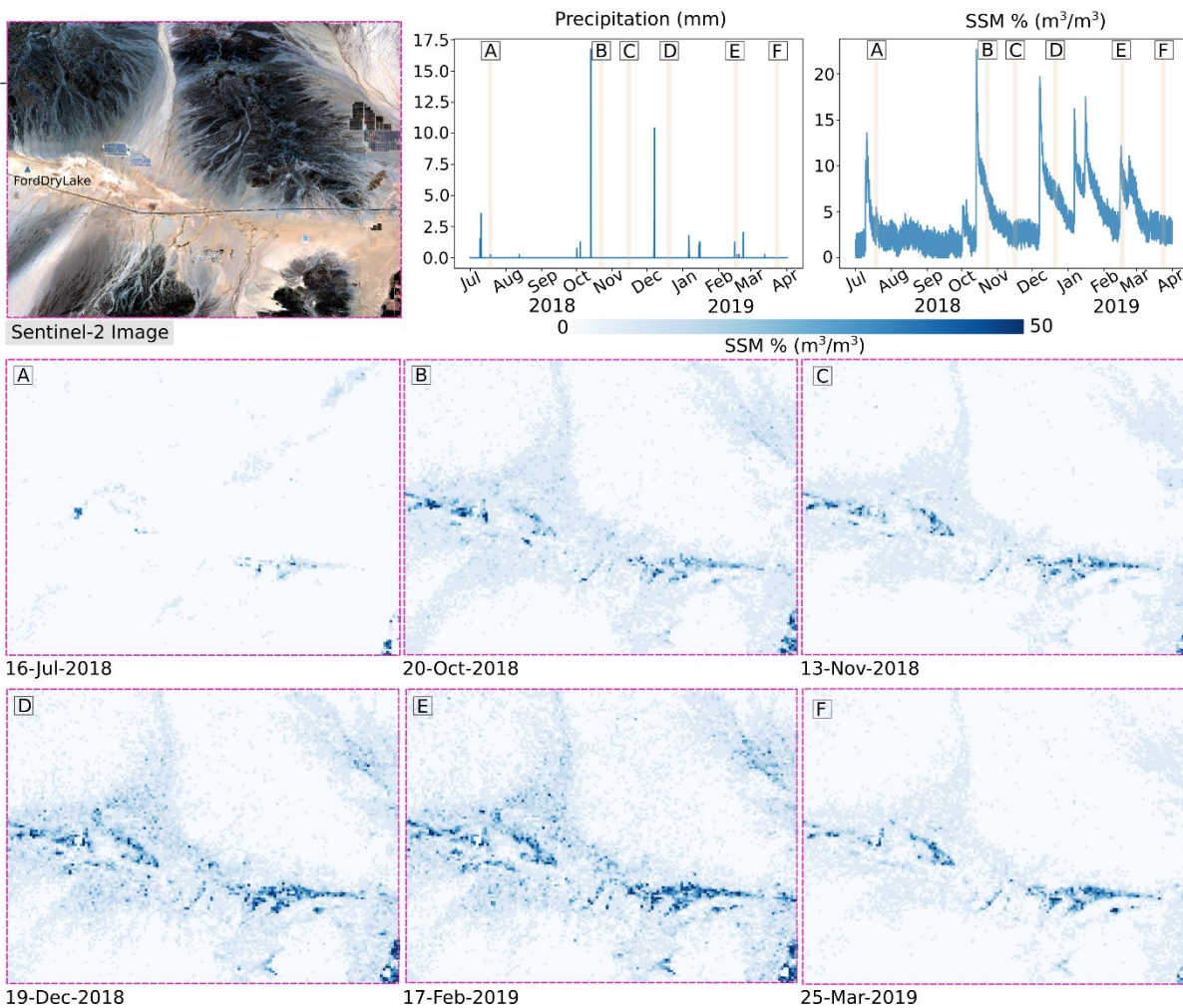

Figure 3.3 InSAR4SM SSM estimations

In Figure 3.4, the soil moisture observations at 5 cm depth from FordDryLake ISMN station are compared with SSM estimations for orbits 173 and 100. For orbit 173, we have 23 SSM estimations with root mean square error (RMSE) of 0.031 m^3/m^3 and Pearson's correlation (R) of 0.93. For orbit 100, we have 22 SSM estimations with RMSE of 0.022 m^3/m^3 and R of 0.82. We can identify that in most cases, we have a positive monotonic relationship between the ISMN observations and InSAR4SM SSM estimations. In both orbits, the InSAR4SM was able to successfully capture the SSM increases due to rain events. However, in cases that we have a SSM decrease, SSM values are overestimated. We believe that this can

be caused by the post-rain coherence loss that is not modeled by the proposed exponential temporal decorrelation model. It is also important to state that the predefined SSM value for the driest acquisition plays an important role and can cause bias/offset effects visible in Figure 3.4.
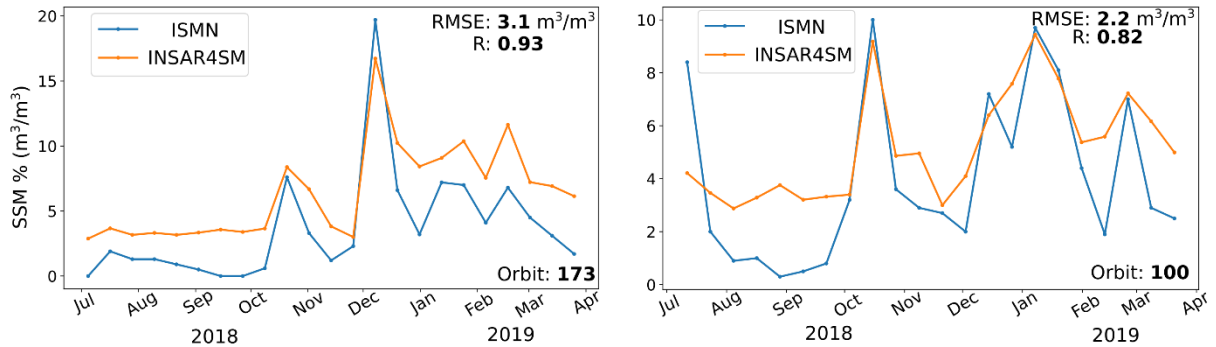

Figure 3.4 InSAR4SM SSM (volumetric %) estimations vs FordDryLake ISMN SSM (volumetric %) observations

In Figure 3.5, the comparison between the InSAR4SM SSM estimations and the ERA5-Land soil moisture data from 0 to 7 cm depth is presented. A consistency between the InSAR4SM SSM estimations from two different orbits can also be observed. For each ERA5-Land grid cell, we can observe the temporal pattern of the InSAR4SM SSM estimations in respect to ERA5-Land data. Different performance of InSAR4SM is observed for each ERA5-Land grid cell due to different land cover composition. In particular, InSAR4SM was not able to capture the SSM temporal pattern for ERA5-Land grid cells 1, 2, 3, 7, 8, 9 and 10 (Figure 3.5) due to their rocky land coverage. Over the other ERA5-Land grid cells (4, 5, 6, 11 and 12), InSAR4SM was able to capture the SSM increases due to rain events. In all cases, InSAR4SM overestimated the SSM decreases after rain events in respect to ERA5-Land data
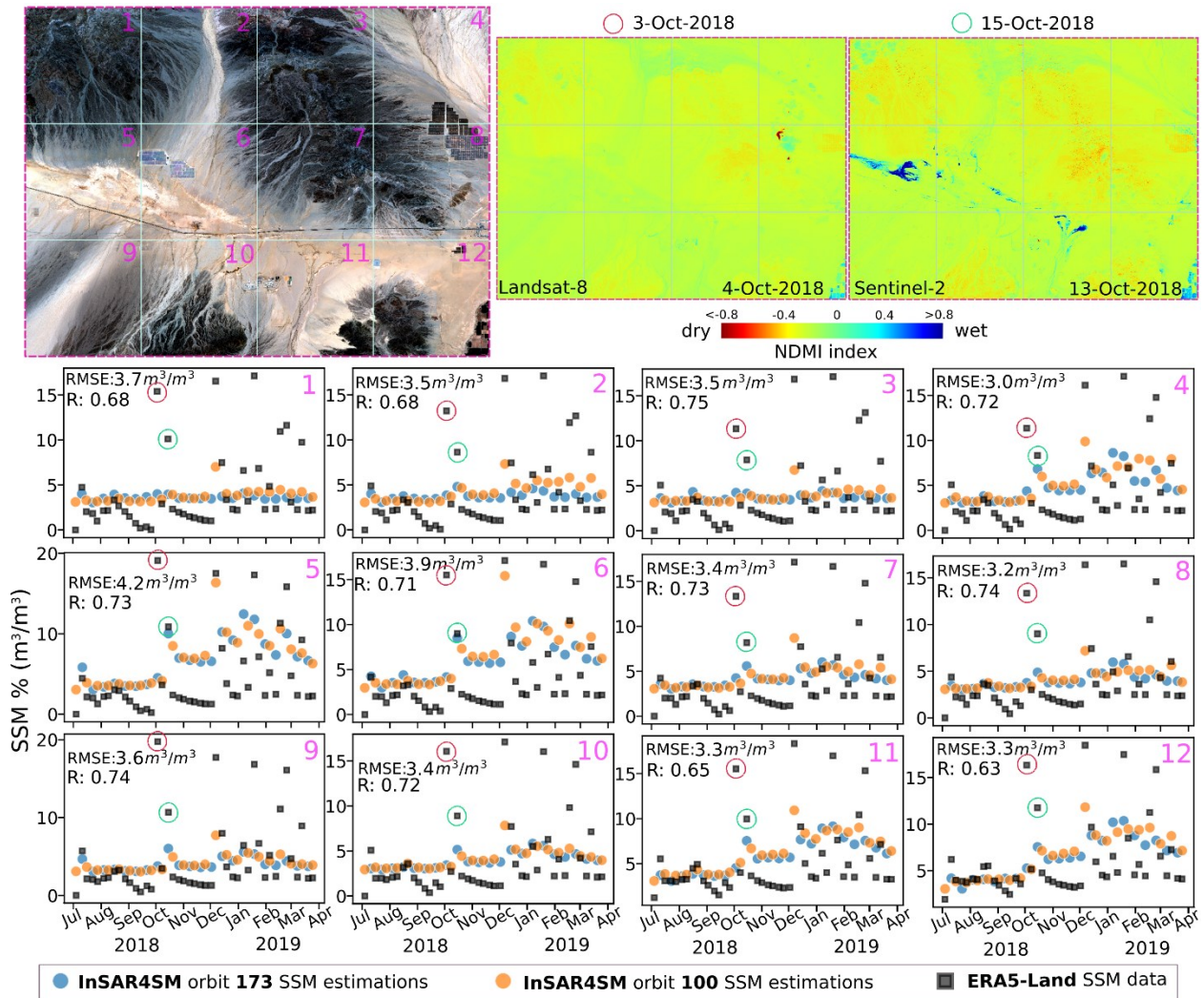
Figure 3.5 InSAR4SM SSM (volumetric %) estimations vs ERA5-Land soil moisture (volumetric %) estimations

For our accuracy assessment, it is important to also consider the accuracy of the ERA-5-Land soil moisture data [132]. In particular, based on the FordDryLake ISMN soil moisture observations (Figure 3.3) and Normalized Difference Moisture Index (NDMI) information [137] from multispectral data (Landsat-8 and Sentinel-2) (Figure 3.5) we identified an anomaly of ERA5-Land soil moisture data point (circled in red in Figure 3.5). In addition, we believe that the observed dispersion of ERA5-Land soil moisture data in 2019 (Figure 3.5) needs further investigation. We consider ERA5-Land soil moisture data the second best option after soil moisture observations from in-situ stations. After dropping the identified outlier, the mean RMSE value over the whole region of InSAR4SM estimations from orbits 173 and 100 is 0.035 m^3/m^3 with R value 0.71.

3.5   Discussion

InSAR4SM was able to produce SSM estimations with remarkable accuracy (~0.035 m^3/m^3) at high spatial resolution (250 m). Complex spatiotemporal patterns of SSM can be identified (Figures 3.3, 3.4) in our case study. Moreover, different orbits yielded consistent results without abnormal discontinuities (Figure 3.5). We believe that the good performance of InSAR4SM is due to three main methodological innovations. First, interferometric observables (InSAR coherence and phase closure) are calculated over homogeneous regions in terms of SAR backscattering [46]. Due to the linkage between SAR intensity and SSM [113], by ensuring that the selected SAR pixels have similar intensity behavior we mitigate the risk to include scatterers that have different SSM patterns. This is considered a methodological improvement in respect to other approaches [111], [115] that assume that all the SAR pixels inside a window share similar SSM patterns. Second, InSAR4SM exploits external meteorological data and SAR backscattering in order to identify the driest image, resolve coherence ambiguity, which is reported at [121] and order SAR acquisitions based on their SSM levels. Ordering is used for the identification of SAR acquisitions that have low SSM conditions. Those "dry" acquisitions are exploited to model coherence loss due to temporal decorrelation and calculate only the coherence information due to SSM variations. Third, SSM inversion procedure was improved because: a) an initialization based on the coherence-based SSM index (Eq. 10) was introduced in order to avoid ambiguities due to randomized initializations [121]; b) a constraint based on the identified driest SAR acquisition was introduced; c) the decomposition of coherence and use only the coherence component related to SSM variations. Next, the main assumptions/limitations of the InSAR4SM approach are discussed.

A complex relationship between interferometric observables, SSM, and land coverage exists [111], [121], [123]. In this study, in order to estimate the coherence information due to SSM variations from the raw coherence a) we considered that coherence losses due to vegetation and geometric decorrelation are negligible and b) we modelled coherence mainly due to surface roughness, and permanent changes from precipitation events. It is important to state that land cover and ground surface roughness are assumed to be constant over time. However, in many cases this is not valid due to anthropogenic (e.g. constructions, mining, agricultural activity) and natural factors (e.g. vegetation changes, post-storm erosion and deposition of sediments). The coherence variations due to the abovementioned factors are not captured by the InSAR4SM`s exponential modelling of temporal decorrelation and SSM estimation errors are introduced. In our case study, this is mostly evident after rain events. In order to overcome this limitation, we believe that coherence loss due to post-storm erosion or deposition of sediments should be modelled. We believe, in order to better discriminate the coherence contribution from SSM variations it is important to consider

more data related to topography, soil composition, temporal and spatial information of precipitation and land cover changes.

Another limitation is related to the complex relationship between different soil types and interferometric observables [111]. For this study, the soil composition of the FordDryLake station was used for the whole region. This choice is considered reasonable due to the ongoing changes from fluvial sediment transport [138] and aeolian sand supplies [139] over desert environments. However, a lower performance of InSAR4SM mainly to rocky desert soils (Figure 3.5) was identified. We believe that incorporating soil properties information [140] and studying interactions between soils and rocks can provide insights regarding the relationship between soil compositions and SSM estimation from interferometric observables.

After several experiments, we concluded that using a SSM grid of 250 m for our case study was suitable to provide accurate SSM estimations. The abovementioned spatial resolution is considered an improvement in comparison with backscattering approaches where 1x1km grid size is commonly used [113]. The selected spatial resolution corresponds to about 12x50 C-band Sentinel-1 SLC resolution pixels. In order to enhance the signal quality and compute the interferometric observables, grouping of the statistically homogeneous pixels is required [51]. In our view, spatial resolution can be improved if we ensure the quality of interferometric measurements. This can be achieved by either using SAR datasets with better spatial resolution or by using SAR data (e.g. L-band) with better signal-to-noise ratio. Further investigation is required in order to understand the relationship between spatial resolution and achieved accuracy by using SSM products with high spatial resolution.

Another assumption of this work is the validity of De Zan's interferometric model. Even though the model was developed for L-band data, it has been used also for C-band data [117], [141]. The proposed InSAR4SM workflow can support L-band data from upcoming SAR missions (NISAR, ROSE-L). It is important to consider that L-band data can provide soil moisture estimations at deeper levels and have lower temporal decorrelation due to changes in the surface conditions (e.g. vegetation) over time. Even though L-band interferometric observables are considered to have better quality in respect to C-band observables [142], over sandy regions L-band presents lower interferometric coherence than C-band [143]. Finally, it would be interesting to evaluate the performance of a more sophisticated interferometric model [122].

3.6   Conclusions

This chapter provides a methodological approach and provides a description of the open-source software package InSAR4SM for soil moisture estimation over arid regions using InSAR and meteorological observations. The following three methodological improvements were introduced (listed below) and accurate SSM estimations at high spatial resolution over an arid region using Sentinel-1 data had been made.

    i.   InSAR coherence and phase closure observables are calculated by forming distributed scatterers [46] and not over squares assuming homogeneity of scatterers [111], [115].

    ii.   Use of external meteorological and SAR backscattering information for resolving coherence ambiguity which is reported at [121] in order to calculate ordering of SAR acquisitions based on their SSM levels.

    iii.   Constrained inversion by using the identified dry SAR acquisition. Improved initialization of the inversion by exploiting the relationship between coherence and SSM [111], [115].

InSAR4SM contributes to better understanding the potential of interferometric observables for SSM estimation for arid regions. InSAR4SM can boost research initiatives and complement other soil moisture products.

4   UNSUPERVISED FLOODWATER MONITORING USING SAR DATA

In this chapter, the work related to floodwater monitoring using SAR data is thoroughly assessed and discussed. First, background information and the objectives of this work are provided in section 4.1. The Flood Mapping Python toolbox (FLOMPY) with its methodological pipeline is introduced in section 4.2. In section 4.3, a case study for Pinios flood is presented. An accuracy assessment of the proposed methodology using EMS products as reference data and a comprehensive discussion regarding the theoretical concepts of the proposed methodology and its limitations are presented in section 4.4. Two case studies that utilize FLOMPY`s floodwater maps are presented in section 4.5. In Section 4.6, conclusions are outlined.

4.1   Background and Introduction

Mapping the spatial extent of surface waters is considered an important step for many initiatives related to water sustainability and natural hazards such as floods [144]. Floods are among the most severe natural disasters, causing great losses to anthropogenic and natural environment around the globe [20]. Moreover, it is important to improve flood relief efforts due to expected increases in the frequency and magnitude of flood events due to climate change [145]. Fast responses from decision makers and emergency managers can mitigate casualties and damages. For this reason, near-real time spaceborne remote sensing data could be exploited in order to provide accurate and rapid maps of affected areas by floods [146]. These maps can be used for calibration and validation of hydrological models [147]. Furthermore, they can help to better set intervention priorities in order to form a loss mitigation plan [148] and even improve flood forecasting [149].

Optical multispectral satellite data can be used in an easy and straightforward way in order to identify flood features in a scene [150], [151]. However, optical data are not optimal to use mainly due to their sensitivity to high cloud coverage which is usually present during rain/flood events [22]. On the other hand, synthetic aperture radar (SAR) sensors have their own source of illumination and can acquire data day and night in all-weather conditions. Over open water surfaces and open floodwater regions, the active SAR pulses have low signal returns due to the specular backscattering [152]. However, inundated vegetation and flooding in urban regions may have strong signal returns due to "double bounce" effect [22]. Moreover, wind can increase the roughness of water surfaces which results in higher backscattering values [153].

A considerable number of methodological approaches based on SAR data have been developed in recent years. Some of the developed methods are based on supervised approaches that require human intervention [154] and/or they are using labelled data which require manual work. This is an important obstacle for developing a robust automatic approach and an ongoing effort to exploit data-driven approaches is present [155]. On the other hand, unsupervised methods are suitable from automatic

workflows. The majority of the unsupervised methods include thresholding operations. Thresholding approaches rely on selecting an adequate threshold in order to determine flooded versus non-flooded areas. Thresholding can be applied on a single backscatter image [156] or on a combination of backscatter time series [157] and on a global or local scale in order to account backscatter spatial variability [158].

It is known that thresholding approaches have many drawbacks and can be affected by a lot of errors [146], [153], [158] such as a) Bragg scattering due to wind [159]; b) "double bounce" effects due to urban and inundated vegetation; c) water-like features (smooth surfaces, soils with high soil moisture, shadow regions) [160]; d) speckle effect and e) selection of threshold. Due to the continuous increase of the data volume and availability, one of the most promising ways to overcome some of the abovementioned drawbacks is via exploiting multi-temporal information [146], [161], [162]. Change detection approaches exploit the multi-temporal information by comparing data related with pre-flood and flood state. It is important to state that the forming of the pre-flood (baseline) dataset is a crucial step to accurately estimate the extent of the floodwater using change detection approaches [152], [163].

In this chapter, we describe a robust methodological approach we introduced [164] able to mitigate the abovementioned drawbacks and provide rapid and accurate flood maps. The proposed approach includes four steps: a) baseline (pre-flood) dataset formation; b) preprocessing; c) SAR statistical temporal analysis; and d) floodwater classification. The proposed pipeline is provided as a free open-source python tool [165] inspired by the free policy of Sentinel-1 data. The objective of this work is to release a tool able to produce floodwater maps which mainly can be used for a) flood damage assessment for fast responses, b) calibration and validation of hydrological models, and c) flood forecasting.

4.2   Methodological pipeline of FLOMPY

In this section, we describe the proposed methodology that is implemented in Flood Mapping Python toolbox (FLOMPY) [165]. FLOMPY is a free and open-source toolbox which is written in Python 3 and published under the GNU GPL version 3 license. Some modules are based on Sentinel's Application Platform (SNAP) [166] functionalities. The proposed and implemented methodology consists of following steps:

4.2.1   Baseline dataset formation

In the first step, a selection of the Sentinel-1 images in order to form a pre-flood (baseline) dataset is performed. Starting with a predefined area of interest and flood event time, all available metadata for Sentinel-1 acquisitions are assessed. We select the optimal orbit track for analysis based on the time difference between acquisition time and the selected time of the flood event. For facilitating the description of the methodology, the acquisition right after the selected time of the flood event will be referred to as the

flood image. Next, we form a pre-flood (baseline) dataset by using only the acquisitions with the same orbit as the flood image of the latest past months that are related with low precipitation.

In particular, based on historical precipitation data (ERA-5), we keep only the acquisitions that have previous 5-day cumulative precipitation lower than a predefined threshold (45 mm in most cases). A 3-month time period was selected to minimize the temporal changes which are not related with the flood and to achieve an adequate number of acquisitions (>5) for temporal statistical analysis. Next, the preprocessing step of the selected pre-flood images and the flood image is performed.

4.2.2   Preprocessing

The pre-processing workflow is based on ESA Sentinel`s Application Platform (SNAP) functionalities and consists of the following steps [166], [167]:

- Orbit correction using precise orbit information or restituted orbit information if the former is not available.
- Thermal noise removal operation.
- Border noise removal which masks artificially low backscatter pixels and invalid data found at the edge of the image swath.
- Radiometric calibration to produce unitless backscatter intensity.
- Subsetting at a given spatial extent.
- Co-registration between all images in order to create a stack that will be used for time series analysis.
- Terrain geocoding using the 1-arcsec digital elevation model (DEM) from the Shuttle Radar Topography Mission (SRTM).
- Local incidence angle normalization based on [168]

4.2.3   SAR statistical temporal analysis

After the preprocessing, a statistical temporal analysis between pre-flood (baseline) stack and flood image is performed. In order to exploit the polarimetric capabilities of Sentinel-1 products, both VV and VH polarizations were exploited. In particular, the product of VH and VV polarizations was calculated using formula (1) and used for the temporal statistics (Appendix A). This way, the processing cost was reduced because only one band (product of VV with VH) is used.

$$\sigma_{VV*VH} = 10log_{10}(\sigma_{VV} \cdot \sigma_{VH}) \qquad (4.1)$$

Where, $\sigma_{VV*VH,}$ the product of backscatter coefficients of VV and VH in decibel and σ_{VV}, σ_{VH} the unitless backscatter coefficient of VV and VH, respectively.

The temporal t-score was selected due to the small sample size and is calculated for each pixel according to the formula (2). The hypothesis is that the backscatter coefficient of the pre-flood state follows a T-distribution. T-distribution is a type of normal distribution for smaller sample sizes.

$$t_{score} = \frac{\sigma_{VV*VH,flood} - mean\sigma_{VV*VH,baseline}}{\dfrac{std\sigma_{VV*VH,baseline}}{\sqrt{n}}}$$

(4.2)

Where, $\sigma_{VV*VH,flood}$ the product of backscatter coefficients between VV and VH of the flood image; $mean\sigma_{VV*VH,baseline}$ and $std\sigma_{VV*VH,baseline}$ the average value and the standard deviation of the product of VV and VH backscatter coefficients of the baseline (pre-flood) stack, respectively; n the number of the acquisitions in the baseline stack

4.2.4   Classification

In the final step, a novel spatially adaptive thresholding methodology was developed for the classification of the calculated t-score map in flooded and non-flooded areas. The t-score has the same resolution with Sentinel-1 GRD products. The classification scheme consists of five main steps (Figure 4.2):

Step 1: Calculation of a mask in order to achieve similar class sizes of the flooded and non-flooded samples. The use of this mask by histogram thresholding algorithms improves their performance significantly [169], [170]. This mask is referred to as a bimodality mask because it is calculated by using bimodality coefficient (BC) [171]. The bimodality coefficient is expressed by the formula:

$$BC = \frac{s^2 + 1}{k + 3\dfrac{(n-1)^2}{(n-2)(n-3)}}$$

(4.3)

Where, s the skewness of the distribution, k its kurtosis and n the number of the samples.

The bimodality mask is computed as follows. First, BC values are calculated at multiple grid sizes that range from 25 to 500 pixels with a step of 25 pixels. The result of each grid size is saved at the t-score`s pixel level. Then, a mean BC value for each pixel is calculated and a single thresholding approach is applied. If the BC value is smaller than 0.555, a uniform distribution is expected. Higher values point toward multimodality [171].

Step 2: In this step, a single threshold that discriminates the flooded and the non-flooded regions based on Kittler-Illingworth algorithm [172] was implemented over the masked t-score. The result of this step is a first binary flood mask by applying the scene-level threshold.

<u>Step 3:</u> Next, a spatial adaptive local thresholding was applied to compress over-detection and under-detection issues from the single scene-level thresholding. The main steps that apply for each flooded-pixel according to the binary flood mask of the previous step are the following:

- For each flooded pixel we select the optimal window size based on the bimodality index value. In particular, from a predefined range of window sizes (from 15 to 80 pixels with a step of 5 pixels) we select the one that yields the maximum bimodality index. If its value is above 0.555 [171] we proceed to the next step. Otherwise, we move in the next flooded pixel.

- A local histogram thresholding based on the Otsu algorithm is performed. More information regarding the Otsu algorithm can be found in [173], [174]. Otsu algorithm was selected due to its good performance in tiled thresholding [170]. From the local thresholding we get two samples. The first sample (sample-1) is the one that includes values less than the local threshold and the second sample (sample-2) is the one that includes values bigger or equal with the local threshold. Next, we test how sample-1 and sample-2 are related with floodwater and non-floodwater population from the step-2 binary flood mask by calculating the following flags:
    - Water_flag1: Is sample-1 similar to floodwater population.
    - Water_flag2: Does sample-1 have significantly lower values in respect to floodwater population.
    - Land_flag1: Is sample-2 similar to non-floodwater population.
    - Land_flag2: Does sample-2 have significantly higher values in respect to floodwater population.

The similarity flags (Water_flag1, Land_flag1) were calculated using a non-parametric two-sample Kolmogorov-Smirnov test with 95% confidence ratio [175]. The comparison flags ((Water_flag2, Land_flag2) were calculated by utilizing the Fisher discriminant ratio [176]. In order to ensure that the local thresholding can improve the scene-level thresholding we follow the decision tree (Figure 4.1) based on the computed flag values.
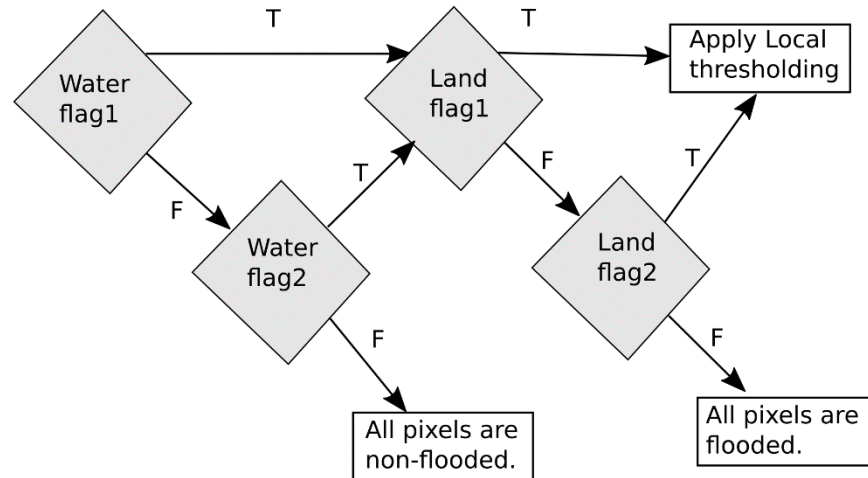
Figure 4.1 Decision tree of adaptive local thresholding methodology

Step 4: Region growing was used in order to improve pixel-based performance by accounting spatial information, compress under-detection issues and reduce omission errors [152]. The region growing algorithm that we developed searches for pixels within the t-score map that are connected neighbours to the flood pixels (seeds) from step 3 and that fall within a tolerance criterion. We point out that the tolerance level is not the same for each seed but it is linearly related with its t-score value. This way the algorithm is stricter for seeds with higher t-scores than for seeds with lower t-scores.

Step 5: Refinement is the final step and consists of a) masking out high slope regions (>15 degrees) from available DEM and b) morphological filtering based on a predefined minimum mapping unit. In particular, based on the predefined minimum mapping unit we fill the small holes and we remove the small objects.
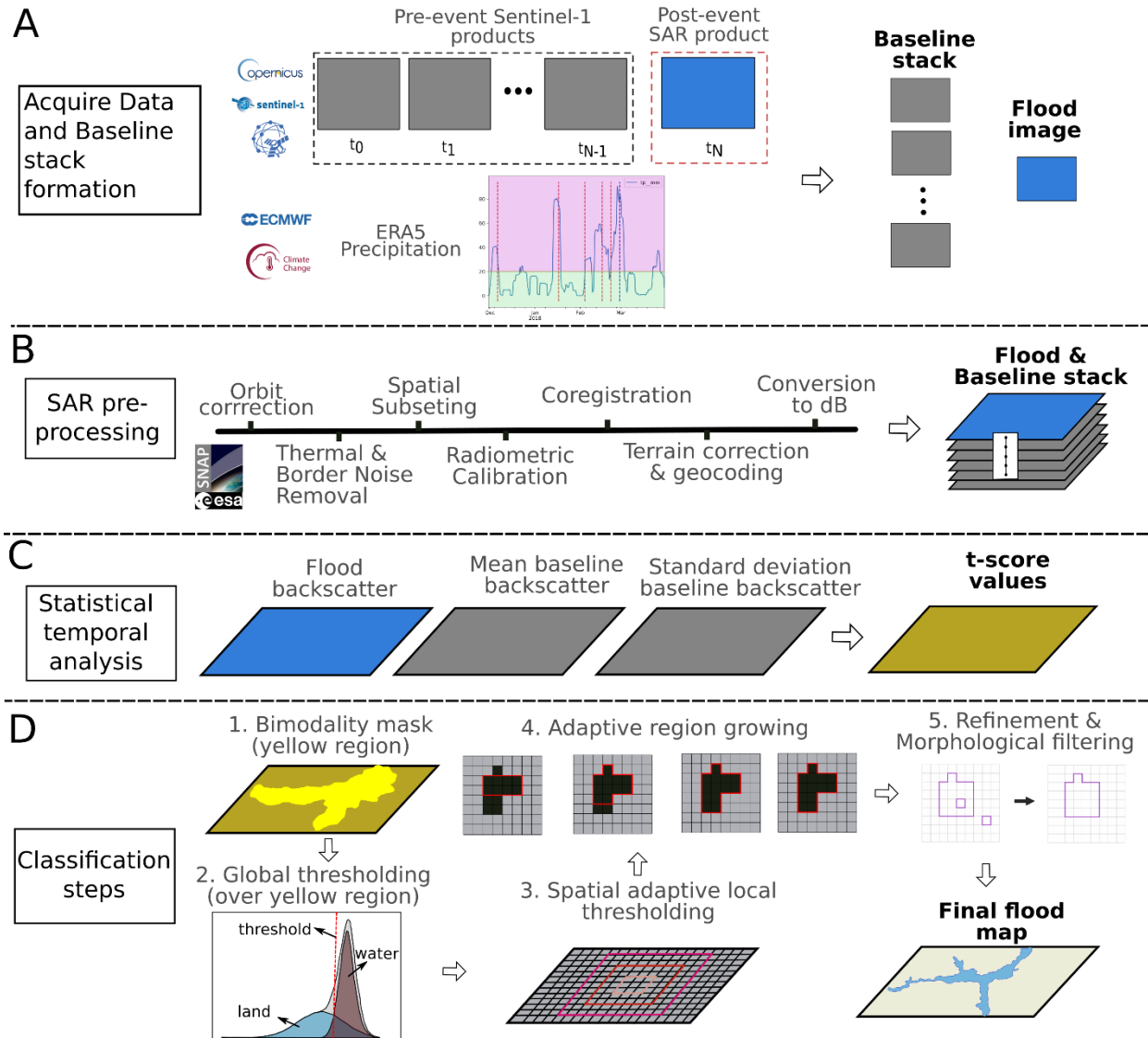
Figure 4.2 Flowchart of the four-step proposed methodological pipeline (FLOMPY).

4.3   The case study of Pinios flood

4.3.1   Area of Interest

Pinios catastrophic flood event occurred in spring of 2018 and was caused by a series of storm events from 21ʳˢᵗ to 26ᵗʰ of February, 2018 [177], [178]. In the particular flood event, Pinios River and all its tributaries have overflowed since 24ᵗʰ of February, 2018 and hundreds of acres of rural and urban areas have been affected by flooding [179].

The area of interest (AOI) is located in the region of central Greece between the cities of Larissa and Trikala. (Figure 4.3a). The complex dendritic hydrographic network consists of Pinios River and its tributaries, and has a length of around 1188 km [180]. Due to the high frequency of the flood events along

Pinios River, many flood protection works have been performed in the past and still planned for the future [181].

We focus on a region (Figure 4.3b) that covers an area of about 764 km^2 and with elevations that vary from 69 to 970 m above sea level (a.s.l.). The relative low terrain elevation along the hydrographic network increases the flood risk at the study area [180]. In Figure 4.3c, a map of maximum floodwater depth is shown to demonstrate the severity and the impact of the flood events over the area of interest. According to the land cover map (Figure 4.3d), cropland covers the largest part of the AOI, especially along Pinios River which is mainly used for irrigation [180], [181]. The intense and high-frequency flood events can cause significant damages to the agricultural production and to several villages along the river network.
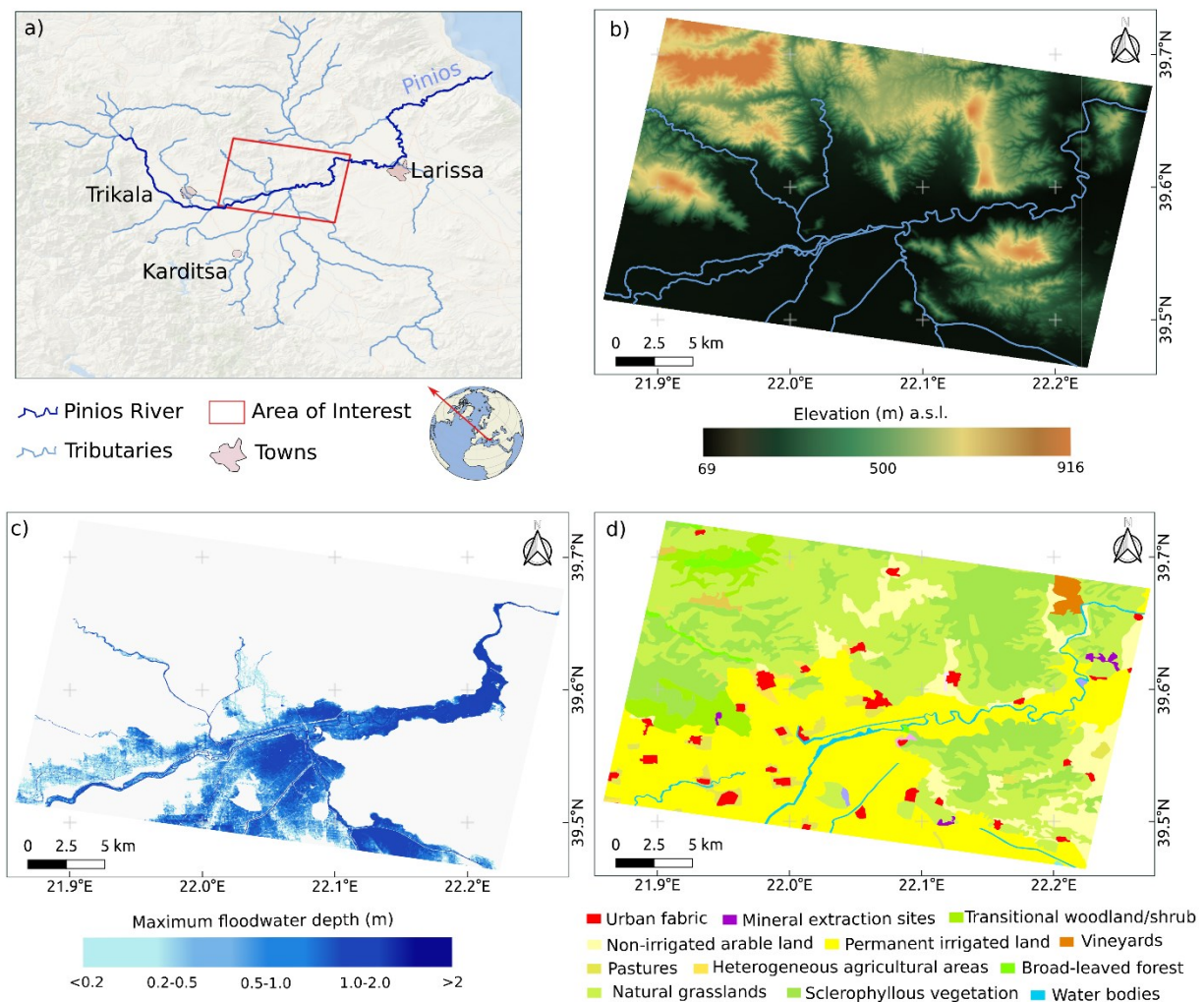
Figure 4.3 Description of the case study a) Pinios river with its major tributaries and main cities over a broader area. The area of interest is denoted with the red rectangle. b) Elevation and hydrographic network of the area of interest c) Spatial distribution of maximum floodwater depth for return period T=50-years over the area of interest [182]. d) Corine land cover level-2 classes of the study area [81]. Reference system is WGS84.

4.3.2   Datasets

SAR data from short revisiting (6-day over Europe) Sentinel-1 constellation from ESA (European Space Agency) are used. Sentinel-1 consists of two satellites namely, Sentinel-1A and Sentinel-1B that were launched in 2014 and 2016, respectively. Sentinel-1 constellation is a polar-orbiting radar imaging system working at C-band (~5.7 cm wavelength). All the Sentinel-1 TOPS IW acquisitions (9) from the descending track with relative orbit number 80, dating from December 2017 till the flood event (28/02/2018) have been processed. All the data are in the Ground Range Detected (GRD) format at a 10-m spatial resolution and both VV and VH polarizations are considered.

The ancillary data consists of the 1arcsec SRTM Digital Elevation Model (DEM) and the precise orbit ephemerides. For validation purposes the EMS product was used. The EMS product was extracted using the semi-automatic method. More information regarding the semi-automatic method and the quality control of the EMS products can be found in [183]. The EMS flood map was produced from a semi-automatic approach on a 3-m Cosmo-Skymed image acquired at 04:00 of 28/02/2018 [179]. We point out that in this case study, the Sentinel-1 image that was used as a flood image was acquired at 04:20 of the 28/02/2018.

4.3.3   Results and accuracy assessment

In this section the FLOMPY results and the validation with EMS product are presented. In Figure 4.4a, an optical image that covers a part of the area of interest is presented. This part will be used for validation purposes. We will focus in three regions to comment on FLOMPY`s performance. In Figure 4.4b, we can visually identify the open floodwater regions with high negative values (dark tones) in the t-score map. The high negative values correspond to a big negative change to the backscatter characteristics of these regions that are connected with the change due to flood event. In Figure 4.4c, we can visually verify the strong agreement of the FLOMPY results with the dark regions of the t-score map and with the EMS product.
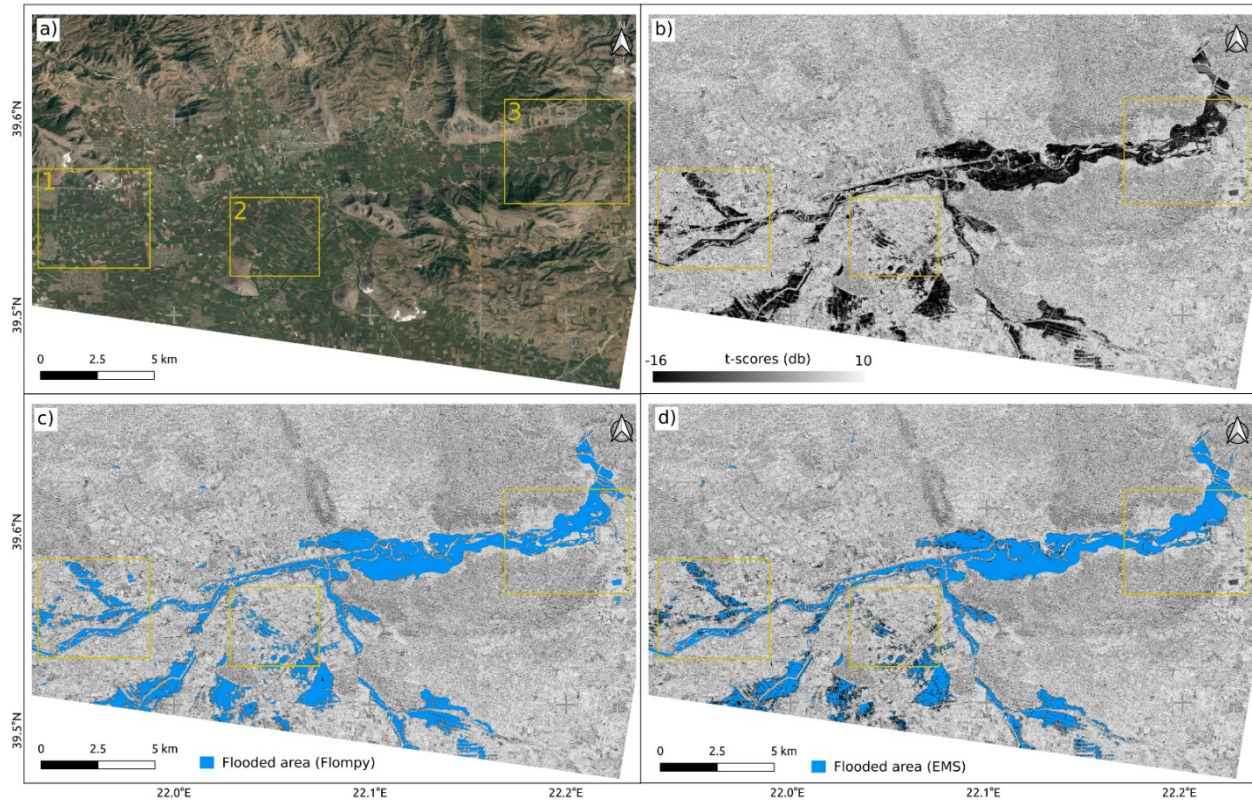
Figure 4.4 Results of the case study a) Optical Google earth imagery, b) T-scores of the Sentinel-1 intensity dataset. c) FLOMPY results. d) EMS results.

The quantitative accuracy assessment of the FLOMPY results was also performed using EMS product as ground truth. Firstly, EMS vector product was rasterized and resampled to FLOMPY 10-m map using nearest neighbor resampling. Then, the accuracy metrics that were calculated according to [184] are the following:

- Overall accuracy which is the proportion of the flood pixels that are mapped correctly.
- User`s accuracy (precision) which is the accuracy related to the commission errors of the flood pixels.
- Producer`s accuracy (recall) which is the accuracy related to the omission errors of the flood pixels
- Kappa score which is a performance metric of the classification compared to just randomly assigning values. Kappa scores can range from -1 to 1. Values close to one indicate that the classification has significantly better performance than random.

In Pinios flood case study the overall accuracy was 0.97 with a kappa score of 0.76. The user`s accuracy of floodwater was 0.78 and the producer`s accuracy of floodwater was 0.76.
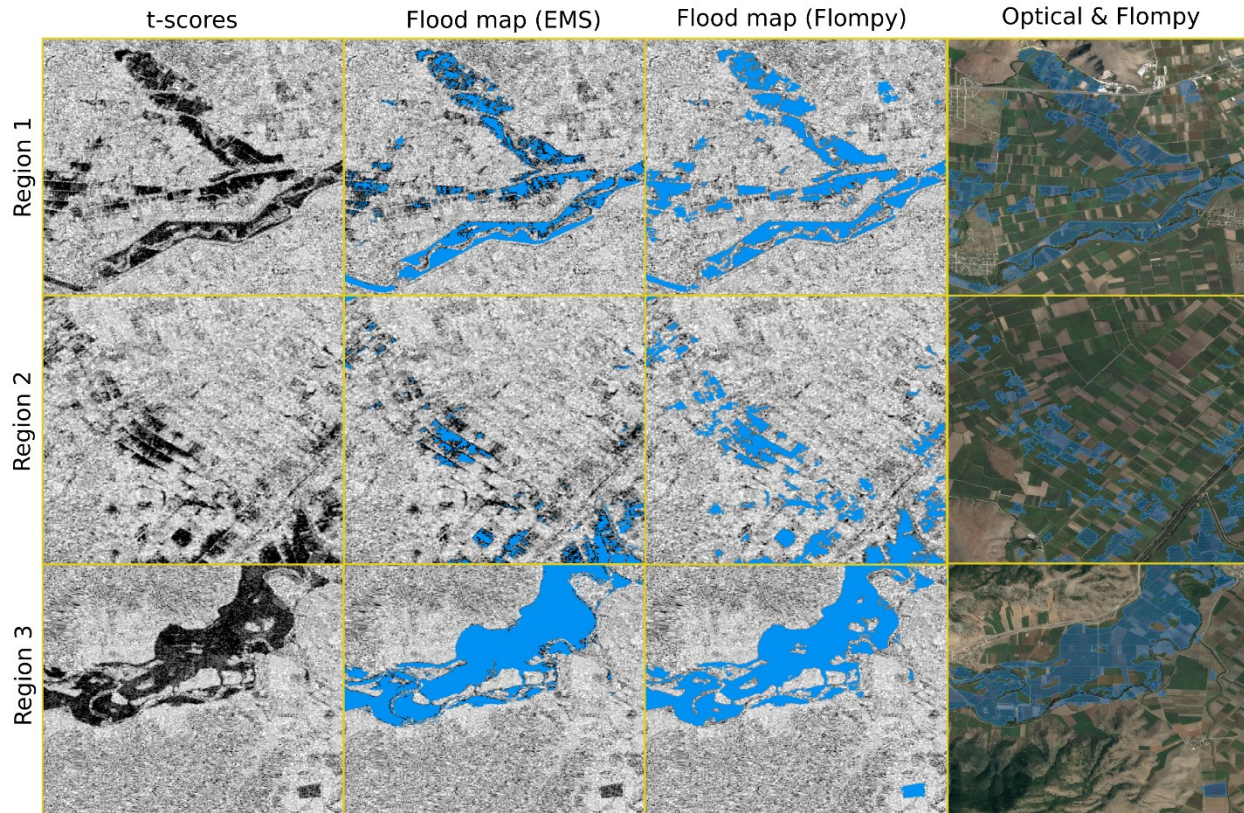
Figure 4.5 Results of selected regions for the case study

We strongly believe that the actual performance of the FLOMPY toolbox cannot be sufficiently depicted by only comparing with EMS products. The abovementioned statement is valid over the three selected regions (Figure 4.4a) where discrepancies between t-score map and EMS product are visible (Figure 4.5). We point out that the omission errors of the EMS product affect the derived accuracy metrics and underestimate the actual FLOMPY`s performance. However, due to the lack of other validation data, EMS products were considered as ground truth data.

4.4   Validation using EMS products

In this section, we describe the main benefits and limitations of the FLOMPY toolbox. FLOMPY toolbox aims at exploiting big EO data, and is especially designed for Sentinel-1 intensity data. Based on a selection of the pre-flood images, a statistical temporal analysis and an adaptive thresholding method satisfactory results were obtained over Pinios flood case study. Moreover, based on thorough experimentation a fixed parametrization for the FLOMPY pipeline was decided.

In order to test the transferability of the implemented methodology, we assessed the accuracy based on EMS products in four more EMS cases. In order to be consistent, we selected EMS cases that their product is based on the analysis of Sentinel-1 images. The same images were used by FLOMPY toolbox.

In Figure 4.6, the main land cover characteristics for each flood case are presented. We point out that in those cases, the floodwater was found over bare soil and low-height vegetated regions. In the Table 1, the FLOMPY`s accuracy metrics are presented. FLOMPY yielded high and consistent accuracies over the presented case studies, which is promising. The SAR temporal t-scores proved to be an objective measure of changes due to flood events. Moreover, the pixel-wise implementation of the FLOMPY is compatible for computation cost improvements such as parallelization.

Figure 4.6 Optical Google earth imagery of validation regions over four EMS cases: a) EMSR504. b) EMSR456. c) EMSR497. d) EMSR520. The validation regions are denoted with the red polygons.

Table 4-1 Accuracy assessment for floodwater in other EMS cases

Case study	EMSR504	EMSR456	EMSR497	EMSR520
Sentinel-1 datetime	19/3/2021 19:07	16/08/2020 23:50	03/02/2021 05:49	16/7/2021 05:41
Location	Taree (Australia)	Nicaragua	Germany	Netherlands
Overall accuracy (OA)	0.95	0.97	0.98	0.95
User`s accuracy (UA)	0.83	0.88	0.81	0.85
Producer`s accuracy (PA)	0.82	0.80	0.81	0.75
Kappa score	0.80	0.83	0.79	0.77

Another important issue is related to the flood classification accuracy. As we already presented in the previous section, EMS accuracy is not homogeneous over different regions of an EMS product. Based on our further analysis of four more EMS cases, we realized that there is also an issue regarding offset errors in EMRS504 [185]. As we can see in Figure 4.7, a systematic offset of the EMS flood map [185] can be observed. In the same figure, a superior performance of the FLOMPY map can be also observed. To our knowledge, no in-situ observations were available for any of the investigated case studies. Even though, the purpose of this study is not to evaluate existing EMS products, we believe that it is important to focus on producing high-quality validated datasets in order to better assess new developed methodologies.
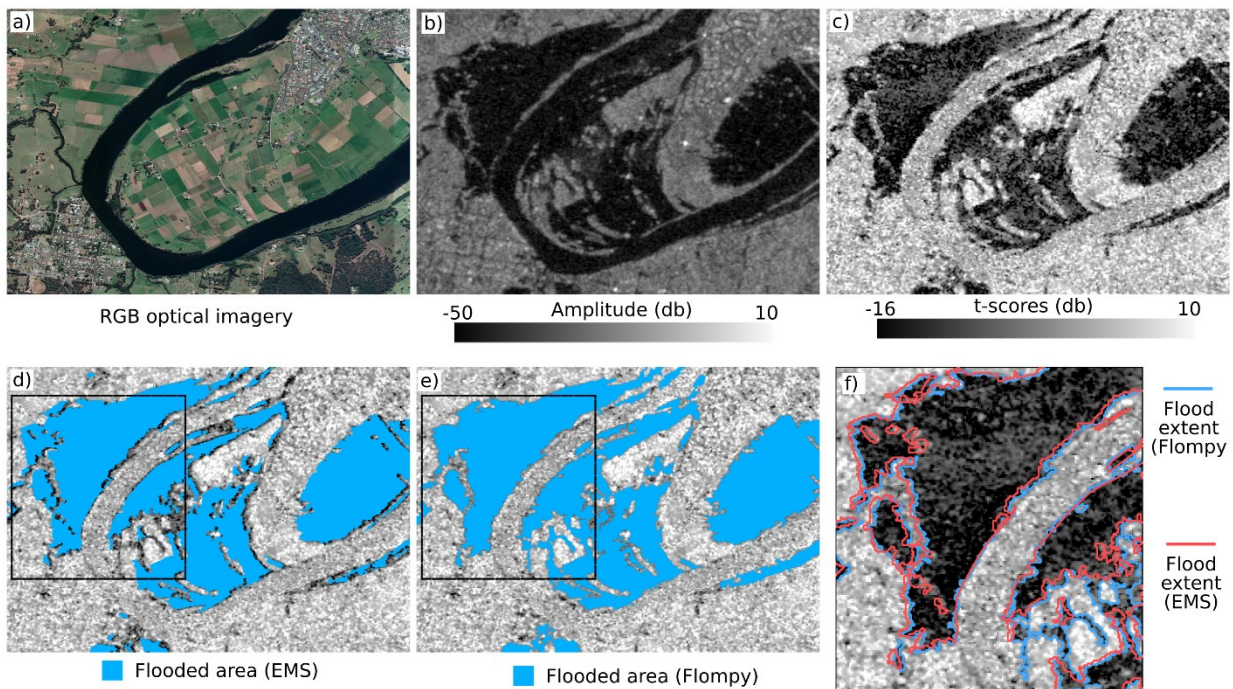
Figure 4.7 Geometric distortions of EMS product (EMSR504) a) Optical Google earth imagery. b) Amplitude which is the product of backscatter coefficients of VV and VH in decibel at flood date. c) T-scores of the Sentinel-1 intensity dataset. d) EMS results overlaid over the t-score image. e) FLOMPY results overlaid over the t-score image. f) Flood extents between FLOMPY and EMS products.

One of the biggest limitations of the FLOMPY pipeline is related with the mapping of flooded regions over medium- and high-height vegetated and urban environments. FLOMPY pipeline was specifically designed to map open floodwater over bare soil and low-height vegetated regions where a decrease of backscatter coefficient is distinct due to specular scattering mechanism [152]. Over flooded medium- and high-height vegetated regions, as well as, flooded urban regions a high increase of the backscatter coefficient can also be observed due to double-bounce scattering mechanisms [158]. Over these regions, mapping floodwater in an unsupervised way at Sentinel-1 resolution (~20x22m) is considered a

really challenging task [186]. One of the future improvements of the FLOMPY toolbox will be the exploitation of interferometric coherence information in order to overcome the abovementioned limitation.

One other limitation of the FLOMPY methodology is related to the quality of the baseline stack. Currently, the baseline stack is formed using images from three months before the flood event. In some cases, a small number of pre-flood images can be available/useful, due to low Sentinel-1 data availability, high precipitation rates or regular inundation patterns (rice fields). In those cases, the assumption regarding the t-distribution of the backscattering coefficient will not be valid anymore. Exploiting more acquisitions with higher temporal separation from the flood date would increase the risk of introducing errors in t-score statistic due to land surface changes (removal of crop canopies). Future improvements of the developed toolbox would be related with the forming of a higher-quality baseline stack with support from multi-orbit Sentinel-1 data, ancillary data and data from other sensors. Exploiting multiple types of data would also lead to a contextualization of the flood extracted areas which is critical. Nevertheless, it is worth exploring since discrimination of the flooded areas can significantly help damage assessment and disaster response actions.

4.5   Case studies based on FLOMPY`s floodwater maps

4.5.1   Flood damage assessment on agricultural regions

Floods are considered the second gravest disaster for the agricultural sector. The increasing intensity and the frequency of flood events can result in significant yield losses. A methodological pipeline able to provide information related to flood-affected agricultural fields is introduced [187]. The proposed methodology is an extension of the initial FLOMPY`s functionalities. Multi-temporal S-2 data were exploited for agricultural information extraction. The required inputs are the geographical region and the time of the flood event. The main processing steps are:

1. Generation of floodwater map using FLOMPY toolbox.
2. Generation of the multispectral cube. In particular, Sentinel-2 level 2A products for three months before the flood event are retrieved. Up-sampling (10m), subsetting and cloud masking are performed.
3. Calculation of field intensity map and field-edge intensity map by analyzing the temporal variation of optical NIR and SWIR information [188] of multispectral cube is performed.
4. Pixel classification of the multispectral cube as field-edge, cultivated or non-cultivated class. The classification is performed by thresholding field and field-edge intensity maps.
5. Calculation of vector field-edge map by combining information from field-edge intensity maps and field-edge binary map predicted from pretrained U-net segmentation model [189].

6. Classification of each delineated field as cultivated or non-cultivated. A field is considered cultivated if at least 30% of its pixels are classified as cultivated.

A case study related to the "Ianos" Mediterranean tropical-like cyclone over an agricultural area in central Greece is presented. The "Ianos" cyclone took place from 14th to 19th of September 2020 causing floods and significant damage in Central Greece. We focus on an agricultural area of 325 km² near Palamas city. The results consist of a) the floodwater map based on FLOMPY toolbox functionalities and b) the flood-affected agricultural fields and their agricultural status (cultivated or non-cultivated).
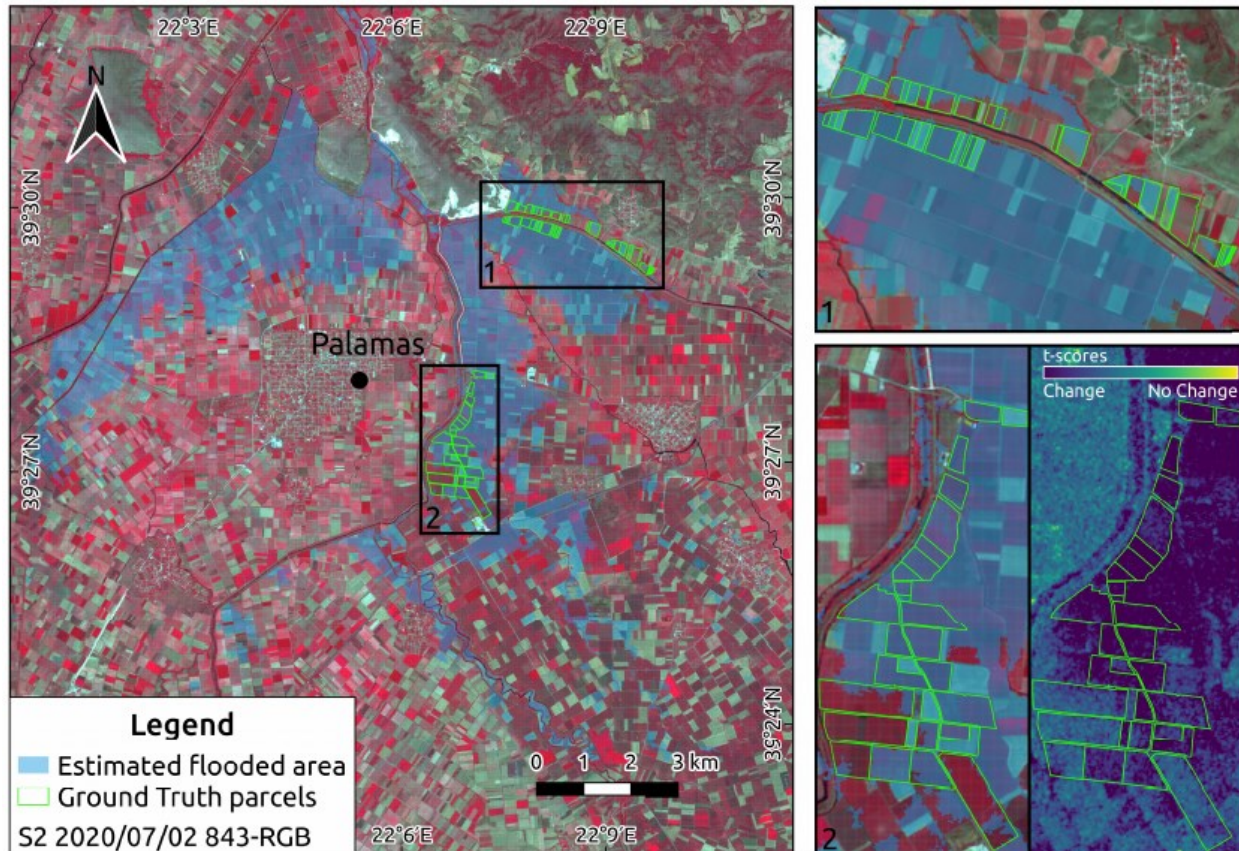
Figure 4.8 Floodwater map (FLOMPY) and in-situ observed flooded fields over the area of interest.

For the particular case study, we managed to collect some in-situ observations of flooded fields that we used to quantify the performance of the FLOMPY algorithm. We need to highlight that due to the severity of the event our in-situ observations (regions 1 and 2 in Figure 4.8) are limited (close to roads) and cannot capture the actual flood conditions. Therefore, we used the observed flooded fields in order to quantify only the omission errors of the FLOMPY performance. FLOMPY successfully detected the 76% of the observed flooded fields. Based on personal communication with farmers of the region, many omitted flooded fields were cultivated with corn that at that time had a height of about 1.5m. Vegetation height is identified as a limitation for floodwater mapping over agricultural regions.

In Figure 4.9, delineated flood affected field geometries are presented. The total amount of detected flood-affected fields were 1582 in total, covering 30 km². Cultivated and non-cultivated fields are presented in green and orange colors, respectively. 1222 out of 1582 fields were detected as cultivated covering 24 km². After personal communication with farmers of the regions, we were able to classify some of the fields as cultivated and non-cultivated. Those fields were used as ground truth for validation reasons. The proposed methodology was able to classify the identified fields correctly with 90% overall accuracy. We believe that the produced maps with delineated flood-affected agricultural fields can be helpful for flood damage assessment, agricultural insurance, food security and recovery planning.
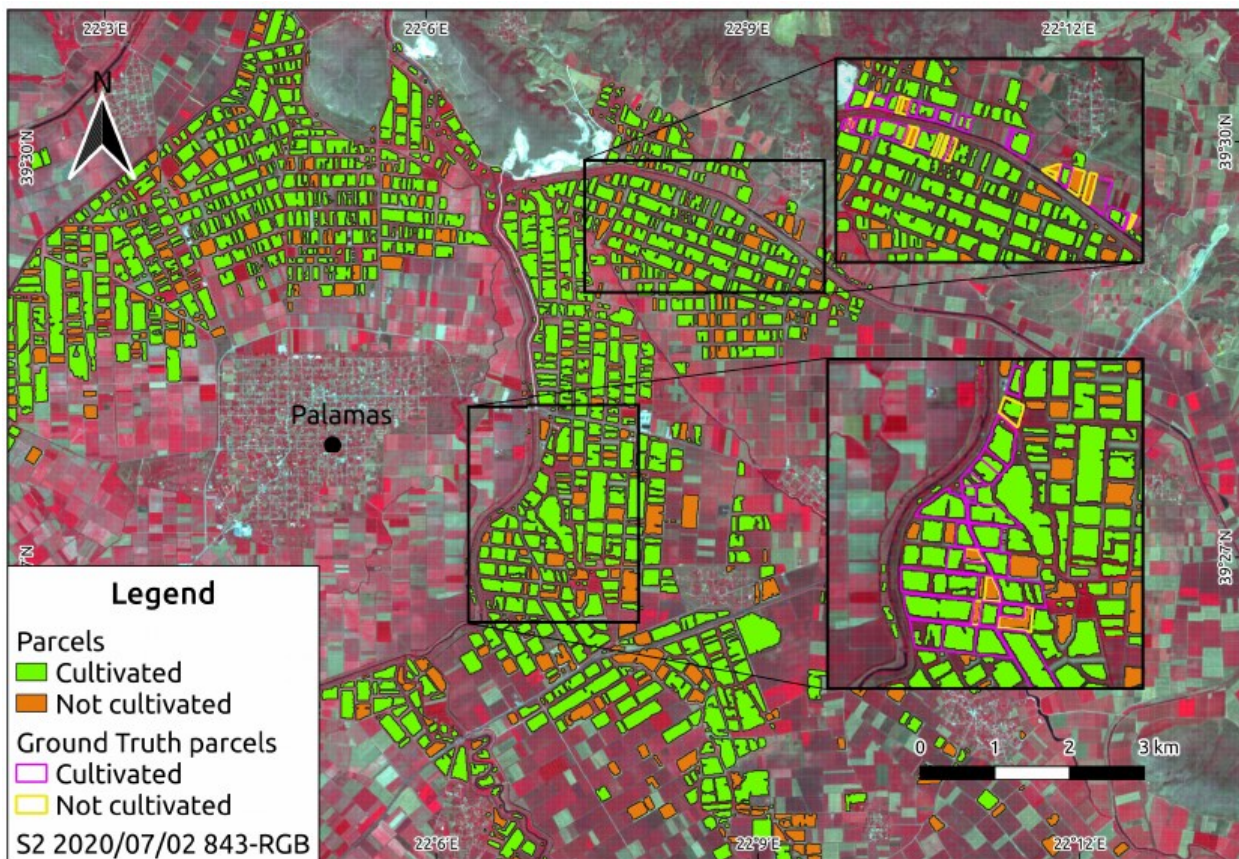
Figure 4.9 Flood-affected delineated agricultural fields and their agricultural status (cultivated or non-cultivated).

4.5.2   Sensitivity analysis of a coupled 1D/2D hydrodynamic model

Hydrodynamic modeling is essential for all the stages of flood disaster management (mitigation, preparedness, response, and recovery). During the last decades, earth observation data have been widely used to improve the performance of flood models. In this case study, a hydraulic modeling analysis was performed and satellite-derived flood delineation maps were exploited. In particular, a sensitivity analysis of an integrated 1D/2D hydraulic model in respect to roughness coefficient and upstream inflow variations, is presented. Upstream inflow information was estimated through a hydrological simulation combined with

a Monte-Carlo uncertainty analysis [178]. Roughness coefficient information was extracted for each land cover from literature [190]. The accuracy assessment was performed by using generated flood delineation maps from FLOMPY software package [165] as reference.

The area of the case study is located at Spercheios River, Central Greece. The flood event which took place in early February of 2015, is studied. The main methodological steps [191] are:

1. Upstream inflow variations were estimated combining a HEC-HMS hydrologic model and Monte-Carlo uncertainty analysis.

2. Estimation of roughness coefficient value ranges for main river (1D) channel based on its reaches (lower, middle and upper).

3. Estimation of roughness coefficient value ranges for each land use category (Paved roads and driveways, Construction sites, Cultivated Crops, Emergent Herbaceous Wetlands, Pasture/ grasslands and Mixed forests) of the overbank flow (2D) area based on the literature.

4. Implementation of HEC-RAS hydraulic simulations incorporating the generated upstream inflow variations, roughness coefficient value ranges for main river (1D) and for each land use category of the overbank flow (2D).

A number of simulations have been performed by using different values for the considered parameters (upstream inflow and roughness coefficient). The sensitivity metrics that have been considered are a) the flooded area generated by the hydraulic model and b) the agreement between the hydraulic model`s flood map and FLOMPY`s flood map. According to the sensitivity analysis results, two main conclusions have been drawn

- The upstream inflow exerted the greatest impact on the hydraulic simulation results.

- Considering the roughness coefficients, the main channel and cultivated crop land cover presented the highest sensitivity. The optimal roughness coefficient value range for the cultivated crop land cover was close to average. For the main channel, it was observed that increasing roughness coefficient yields better performance.

In this case study, satellite derived flood maps were used to investigate the sensitivity of hydraulic model. FLOMPY`s maps have been used to assess and improve the performance of hydraulic modeling procedure. According to our view, an uncertainty layer of satellite derived flood maps could have been beneficial to better assess the performance of hydrodynamic modelling.

4.6   Conclusions

In this chapter we described a methodological framework for floodwater mapping using Sentinel-1 time series. We demonstrated its robust performance over several investigated cases around the world achieving high accuracy (OA~ 0.97, Kappa score~ 0.77). The proposed methodology was implemented in

an open-source python toolbox named FLOMPY. FLOMPY toolbox requires as inputs only the location and the time of the flood event. Using FLOMPY, even less-experienced users can exploit the Sentinel-1 time series in a standard and consistent way. The FLOMPY toolbox is open-source, modular and easy to integrate in workflows, therefore optimal for collaboration and potential future improvements. We also presented two case studies that utilized FLOMPY floodwater maps for a) flood damage assessment on agricultural regions and b) sensitivity analysis of a coupled 1D/2D hydrodynamic model. We consider this tool useful and relevant in the context of emerging initiatives such as EMS [192] and ARIA [95].

5   CONCLUSIONS & FUTURE WORK

5.1   Overall Conclusions

In this dissertation, we have introduced methodologies and presented applications for monitoring ground deformation, soil moisture and floodwater with time series analysis of SAR data. The majority of the proposed methodologies and developed algorithms are released as open source software according to the fourth objective of this dissertation.

In Chapter 2, we demonstrated the potential of several TSInSAR methodologies for ground deformation estimation, following the first objective of this dissertation. Firstly, we decomposed multiple track LOS ground deformation estimations to vertical and horizontal components. A centimetric accuracy in respect to leveling measurements was achieved. Then, we provided a thorough performance analysis of several TSInSAR methodologies over a region with high complexity of ground deformation patterns (mining region). All the considered TSInSAR methods presented the best accuracies over land cover categories with stable scattering properties. Disagreements between the results of the selected TSInSAR approaches were found in the vegetated areas. Stamps/MTI approach was found the most reliable method mainly due to its sophisticated unwrapping approach which exploits the spatiotemporal behavior of the wrapped phase. Next, we proposed a wavelet-based approach able to visualize and explore the relationships between potential driving factors and ground deformation results from TSInSAR. Lastly a software (Interferon) has been developed that implements the TSInSAR using persistent and/or distributed scatterers.

In Chapter 3, we proposed an innovative methodology for soil moisture estimation exploiting InSAR observables and we presented an application over an arid region, fulfilling in this way the second objective of this dissertation. We released the open-source software package InSAR4SM for soil moisture estimation over arid regions using InSAR and meteorological observations. Three main methodological improvements were introduced and accurate SSM estimations at high spatial resolution (250 m) over an arid region in California, USA using Sentinel-1 data had been made. These are a) the calculation of interferometric observables by forming distributed scatterers, b) incorporation of meteorological information, and c) enhanced inversion procedure. The released software package (InSAR4SM) is an initiative that can improve the understanding of the interferometric observables for soil moisture estimation, can boost research initiatives and can generate information to complement other soil moisture products.

In Chapter 4, we proposed a fast, unsupervised methodological framework for floodwater monitoring/mapping using Sentinel-1 intensity time series, according to the third objective of this dissertation. The methodological framework was released as an open-source project called Flood Mapping PYthon toolbox (FLOMPY). The main innovations are: a) use of meteorological data as a-priori knowledge b) exploitation of multitemporal SAR data and c) adaptive sophisticated thresholding. We demonstrated

FLOMPY`s robust performance over several investigated cases around the world. We also presented two case studies that utilized FLOMPY floodwater maps for a) flood damage assessment on agricultural regions and b) sensitivity analysis of a coupled 1D/2D hydrodynamic model. The vision of FLOMPY initiative is similar to emerging initiatives such as EMS and ARIA in the context of flood disaster resilience.

5.2   Future Work

In this section, we present some areas of future activities, inspired by the work of this dissertation. In chapter 2, we presented the capabilities and the limitations of several TSInSAR methodologies for ground deformation estimation. In our view, the following future actions can be accomplished:

  i.   Release of the developed TSInSAR software (Interferon) as an open-source software package under FAIR principles [193]. We believe this will boost research and help collaborations.

 ii.   Applications of the Interferon over regions that groundwater extraction activities occur. Extraction of the TSInSAR ground deformation component that is related to groundwater fluctuations and optional use of gravimetric data [12]. Modelling of groundwater variations by exploiting TSInSAR technology. A data-driven approach is considered promising due to the big volume of TSInSAR results.

iii.   Application of the Interferon over permafrost regions. Due to peculiar characteristics of permafrost regions, methodological enhancements to increase the estimation accuracy of ground deformation in such areas are required. Modelling of the active layer freeze-thaw cycle by exploiting TSInSAR ground deformation results is the final goal of this activity.

In chapter 3, a novel methodological pipeline able to estimate soil moisture from interferometric coherence and phase closure is presented. A list of the future actions in order to improve the accuracy of soil moisture estimations and the performance of InSAR4SM software package is provided.

  i.   Applications of InSAR4SM to other arid regions in order to further test its performance and comparison with other interferometric models (e.g. PCIM [122]). Potential improvements of the spatial resolution of the produced soil moisture maps. Use of soil properties from soil databases [140] in order to better model the scattering behavior of soil.

 ii.   One of the biggest limitations of InSAR4SM is its inability to model coherence loss due to post-storm erosion or deposition of sediments. We believe that the use of topography, land cover, rain rate and soil composition information can be beneficial.

iii.   Experiment with simulated NISAR data in order to provide support for upcoming L-band (NISAR, ROSE-L) data.

In chapter 4, a methodological pipeline able to identify floodwater regions by using Sentinel-1 intensity time series is introduced. The following list of future actions can improve the performance and accuracy of floodwater mapping/monitoring.

i.   Support the SLC Sentinel-1 products in order to include interferometric coherence information. Coherence information is considered an essential observable for floodwater mapping over urban environments [194], [195].

ii.   Investigate the performance of convolutional neural networks (such as AlbuNet-34; FCN; DeepLabV3+; UNet; U-Net++) which according to [196] outperform rule-based approaches and potential inclusion in the FLOMPY.

iii. Extension of FLOMPY for urban areas by introducing a recurrent neural network approach as a probabilistic anomaly detector of the temporal coherence. This particular action is inspired by [197].

6 BIBLIOGRAPHY

[1]   "Forging a climate-resilient Europe - the new EU Strategy on Adaptation to Climate Change," *European Commission*, 2021. https://eur-lex.europa.eu/legal-content/EN/TXT/PDF/?uri=CELEX:52021DC0082&from=EN (accessed Nov. 05, 2022).

[2]   U. Khanal, C. Wilson, B. L. Lee, and V.-N. Hoang, "Climate change adaptation strategies and food productivity in Nepal: a counterfactual analysis," *Clim. Change*, vol. 148, no. 4, pp. 575–590, Jun. 2018, doi: 10.1007/s10584-018-2214-2.

[3]   E. Sesana, A. S. Gagnon, C. Ciantelli, J. Cassar, and J. J. Hughes, "Climate change impacts on cultural heritage: A literature review," *WIREs Clim. Chang.*, vol. 12, no. 4, pp. 1–29, Jul. 2021, doi: 10.1002/wcc.710.

[4]   F. Cottier, M. Flahaux, J. Ribot, R. Seager, and G. Ssekajja, "Framing the frame: Cause and effect in climate-related migration," *World Dev.*, vol. 158, p. 106016, Oct. 2022, doi: 10.1016/j.worlddev.2022.106016.

[5]   J. Nalau and B. Verrall, "Mapping the evolution and current trends in climate change adaptation science," *Clim. Risk Manag.*, vol. 32, no. August 2020, p. 100290, 2021, doi: 10.1016/j.crm.2021.100290.

[6]   J. Yang *et al.*, "Erratum: The role of satellite remote sensing in climate change studies," *Nat. Clim. Chang.*, vol. 3, no. 11, pp. 1001–1001, Nov. 2013, doi: 10.1038/nclimate2033.

[7]   B. Sirmacek and R. Vinuesa, "Remote sensing and AI for building climate adaptation applications," *Results Eng.*, vol. 15, no. July, p. 100524, Sep. 2022, doi: 10.1016/j.rineng.2022.100524.

[8]   S. Mukherjee, A. Mishra, and K. E. Trenberth, "Climate Change and Drought: a Perspective on Drought Indices," *Curr. Clim. Chang. Reports*, vol. 4, no. 2, pp. 145–163, Jun. 2018, doi: 10.1007/s40641-018-0098-x.

[9]   J. D. Petersen-Perlman, I. Aguilar-Barajas, and S. B. Megdal, "Drought and groundwater management: Interconnections, challenges, and policyresponses," *Curr. Opin. Environ. Sci. Heal.*, vol. 28, p. 100364, Aug. 2022, doi: 10.1016/j.coesh.2022.100364.

[10]   J. Bhardwaj, Y. Kuleshov, Z.-W. Chua, A. B. Watkins, S. Choy, and Q. (Chayn) Sun, "Evaluating Satellite Soil Moisture Datasets for Drought Monitoring in Australia and the South-West Pacific," *Remote Sens.*, vol. 14, no. 16, p. 3971, Aug. 2022, doi: 10.3390/rs14163971.

[11]   E. Chaussard, P. Milillo, R. Bürgmann, D. Perissin, E. J. Fielding, and B. Baker, "Remote Sensing of Ground Deformation for Monitoring Groundwater Management Practices: Application to the Santa Clara Valley During the 2012–2015 California Drought," *J. Geophys. Res. Solid Earth*, vol. 122, no. 10, pp. 8566–8582, Oct. 2017, doi: 10.1002/2017JB014676.

[12]   W. R. Neely, A. A. Borsa, J. A. Burney, M. C. Levy, F. Silverii, and M. Sneed, "Characterization of Groundwater Recharge and Flow in California's San Joaquin Valley From InSAR-Observed Surface Deformation," *Water Resour. Res.*, vol. 57, no. 4, pp. 1–20, Apr. 2021, doi: 10.1029/2020WR028451.

[13]   R. Li *et al.*, "Monitoring surface deformation of permafrost in Wudaoliang Region, Qinghai–Tibet Plateau with ENVISAT ASAR data," *Int. J. Appl. Earth Obs. Geoinf.*, vol. 104, p. 102527, Dec. 2021, doi: 10.1016/j.jag.2021.102527.

[14]   X. Zhang *et al.*, "Time-series InSAR monitoring of permafrost freeze-thaw seasonal displacement over Qinghai-Tibetan Plateau using sentinel-1 data," *Remote Sens.*, vol. 11, no. 9, 2019, doi: 10.3390/rs11091000.

[15]   L. Delevinge, W. Glazener, L. Gregoir, and K. Henderson, "Climate risk and decarbonization: What every mining CEO needs to know," 2020. [Online]. Available: https://www.mckinsey.com/~/media/McKinsey/Business Functions/Sustainability/Our Insights/Climate risk and decarbonization What every mining CEO needs to know/Climate-risk-and-decarbonization-What-every-mining-CEO-needs-to-know.ashx.

[16]   M. Zheng, H. Zhang, K. Deng, S. Du, and L. Wang, "Analysis of Pre- and Post-Mine Closure Surface Deformations in Western Xuzhou Coalfield From 2006 to 2018," *IEEE Access*, vol. 7, pp. 124158–124172, 2019, doi: 10.1109/access.2019.2938846.

[17]   D. Becker, F. J. Othmer, and S. Greiving, "Climate Impact Assessment for Sustainable Structural Change in the Rhenish Lignite Mining Region," *Land*, vol. 11, no. 7, p. 957, Jun. 2022, doi: 10.3390/land11070957.

[18]   E. Chaussard, F. Amelung, H. Abidin, and S.-H. Hong, "Sinking cities in Indonesia: ALOS PALSAR detects rapid subsidence due to groundwater and gas extraction," *Remote Sens. Environ.*, vol. 128, pp. 150–161, Jan. 2013, doi: 10.1016/j.rse.2012.10.015.

[19]   L. Wang *et al.*, "Permafrost Ground Ice Melting and Deformation Time Series Revealed by Sentinel-1 InSAR in the Tanggula Mountain Region on the Tibetan Plateau," *Remote Sens.*, vol. 14, no. 4, p. 811, Feb. 2022, doi: 10.3390/rs14040811.

[20]   J. Sanyal and X. X. Lu, "Application of remote sensing in flood management with special reference to monsoon Asia: A review," *Nat. Hazards*, vol. 33, no. 2, pp. 283–301, 2004, doi: 10.1023/B:NHAZ.0000037035.65105.95.

[21]   J. Boulange, N. Hanasaki, D. Yamazaki, and Y. Pokhrel, "Role of dams in reducing global flood exposure under climate change," *Nat. Commun.*, vol. 12, no. 1, p. 417, Dec. 2021, doi: 10.1038/s41467-020-20704-0.

[22]   X. Shen, E. N. Anagnostou, G. H. Allen, G. Robert Brakenridge, and A. J. Kettner, "Near-real-time

non-obstructed flood inundation mapping using synthetic aperture radar," *Remote Sens. Environ.*, vol. 221, no. October 2018, pp. 302–315, 2019, doi: 10.1016/j.rse.2018.11.008.

[23] C. Colesanti, S. Le Mouelic, M. Bennani, D. Raucoules, C. Carnec, and A. Ferretti, "Detection of mining related ground instabilities using the Permanent Scatterers technique—a case study in the east of France," *Int. J. Remote Sens.*, vol. 26, no. 1, pp. 201–207, Jan. 2005, doi: 10.1080/0143116042000274069.

[24] F. Raspini *et al.*, "Continuous, semi-automatic monitoring of ground deformation using Sentinel-1 satellites," *Sci. Rep.*, vol. 8, no. 1, p. 7253, Dec. 2018, doi: 10.1038/s41598-018-25369-w.

[25] J. Biggs, T. Wright, Z. Lu, and B. Parsons, "Multi-interferogram method for measuring interseismic deformation: Denali Fault, Alaska," *Geophys. J. Int.*, vol. 170, no. 3, pp. 1165–1179, Sep. 2007, doi: 10.1111/j.1365-246X.2007.03415.x.

[26] I. Papoutsis *et al.*, "Mapping inflation at Santorini volcano, Greece, using GPS and InSAR," *Geophys. Res. Lett.*, vol. 40, no. 2, pp. 267–272, Jan. 2013, doi: 10.1029/2012GL054137.

[27] F. Calò *et al.*, "Enhanced landslide investigations through advanced DInSAR techniques: The Ivancich case study, Assisi, Italy," *Remote Sens. Environ.*, vol. 142, pp. 69–82, Feb. 2014, doi: 10.1016/j.rse.2013.11.003.

[28] C. Zhao, Q. Zhang, Y. He, J. Peng, C. Yang, and Y. Kang, "Small-scale loess landslide monitoring with small baseline subsets interferometric synthetic aperture radar technique—case study of Xingyuan landslide, Shaanxi, China," *J. Appl. Remote Sens.*, vol. 10, no. 2, p. 026030, Jun. 2016, doi: 10.1117/1.JRS.10.026030.

[29] B. Osmanoğlu, F. Sunar, S. Wdowinski, and E. Cabral-Cano, "Time series analysis of InSAR data: Methods and trends," *ISPRS J. Photogramm. Remote Sens.*, vol. 115, pp. 90–102, May 2016, doi: 10.1016/j.isprsjprs.2015.10.003.

[30] S. Samsonov, N. D'Oreye, and B. Smets, "Ground deformation associated with post-mining activity at the French–German border revealed by novel InSAR time series method," *Int. J. Appl. Earth Obs. Geoinf.*, vol. 23, no. 1, pp. 142–154, Aug. 2013, doi: 10.1016/j.jag.2012.12.008.

[31] A. Ferretti, C. Prati, and F. Rocca, "Permanent scatterers in SAR interferometry," *IEEE Trans. Geosci. Remote Sens.*, vol. 39, no. 1, pp. 8–20, 2001, doi: 10.1109/36.898661.

[32] C. Werner, U. Wegmuller, T. Strozzi, and A. Wiesmann, "Interferometric point target analysis for deformation mapping," in *IGARSS 2003. 2003 IEEE International Geoscience and Remote Sensing Symposium. Proceedings (IEEE Cat. No.03CH37477)*, 2003, vol. 7, no. July, pp. 4362–4364, doi: 10.1109/IGARSS.2003.1295516.

[33] A. Hooper, H. Zebker, P. Segall, and B. Kampes, "A new method for measuring deformation on volcanoes and other natural terrains using InSAR persistent scatterers," *Geophys. Res. Lett.*, vol. 31,

no. 23, pp. 1–5, Dec. 2004, doi: 10.1029/2004GL021737.

[34]   A. Hooper, P. Segall, and H. Zebker, "Persistent scatterer interferometric synthetic aperture radar for crustal deformation analysis, with application to Volcán Alcedo, Galápagos," *J. Geophys. Res.*, vol. 112, no. B7, p. B07407, Jul. 2007, doi: 10.1029/2006JB004763.

[35]   A. Ferretti *et al.*, "Submillimeter Accuracy of InSAR Time Series: Experimental Validation," *IEEE Trans. Geosci. Remote Sens.*, vol. 45, no. 5, pp. 1142–1153, May 2007, doi: 10.1109/TGRS.2007.894440.

[36]   A. Hooper, D. Bekaert, K. Spaans, and M. Arıkan, "Recent advances in SAR interferometry time series analysis for measuring crustal deformation," *Tectonophysics*, vol. 514–517, pp. 1–13, Jan. 2012, doi: 10.1016/j.tecto.2011.10.013.

[37]   P. Berardino, G. Fornaro, R. Lanari, and E. Sansosti, "A new algorithm for surface deformation monitoring based on small baseline differential SAR interferograms," *IEEE Trans. Geosci. Remote Sens.*, vol. 40, no. 11, pp. 2375–2383, Nov. 2002, doi: 10.1109/TGRS.2002.803792.

[38]   T. R. Lauknes, H. A. Zebker, and Y. Larsen, "InSAR Deformation Time Series Using an L_{1}-Norm Small-Baseline Approach," *IEEE Trans. Geosci. Remote Sens.*, vol. 49, no. 1, pp. 536–546, Jan. 2011, doi: 10.1109/TGRS.2010.2051951.

[39]   P. López-Quiroz, M.-P. Doin, F. Tupin, P. Briole, and J.-M. Nicolas, "Time series analysis of Mexico City subsidence constrained by radar interferometry," *J. Appl. Geophys.*, vol. 69, no. 1, pp. 1–15, Sep. 2009, doi: 10.1016/j.jappgeo.2009.02.006.

[40]   D. Sandwell, R. Mellors, X. Tong, M. Wei, and P. Wessel, "Open radar interferometry software for mapping surface Deformation," *Eos, Trans. Am. Geophys. Union*, vol. 92, no. 28, pp. 234–234, Jul. 2011, doi: 10.1029/2011EO280002.

[41]   P. Agram, R. Jolivet, and M. Simons, "Generic InSAR Analysis Toolbox (GIAnT) - User Guide," 2016. http://earthdef.caltech.edu/projects/giant/wiki (accessed Mar. 25, 2020).

[42]   S. V. Samsonov, W. Feng, A. Peltier, H. Geirsson, N. D'Oreye, and K. F. Tiampo, "Multidimensional Small Baseline Subset (MSBAS) for volcano monitoring in two dimensions: Opportunities and challenges. Case study Piton de la Fournaise volcano," *J. Volcanol. Geotherm. Res.*, vol. 344, pp. 121–138, Sep. 2017, doi: 10.1016/j.jvolgeores.2017.04.017.

[43]   "Python tool for InSAR Rate and Time-series Estimation." https://github.com/GeoscienceAustralia/PyRate (accessed Mar. 25, 2020).

[44]   Z. Yunjun, H. Fattahi, and F. Amelung, "Small baseline InSAR time series analysis: Unwrapping error correction and noise reduction," *Comput. Geosci.*, vol. 133, no. i, p. 104331, Dec. 2019, doi: 10.1016/j.cageo.2019.104331.

[45]   A. M. Guarnieri and S. Tebaldini, "On the Exploitation of Target Statistics for SAR Interferometry

Applications," *IEEE Trans. Geosci. Remote Sens.*, vol. 46, no. 11, pp. 3436–3443, Nov. 2008, doi: 10.1109/TGRS.2008.2001756.

[46]   A. Ferretti, A. Fumagalli, F. Novali, C. Prati, F. Rocca, and A. Rucci, "A New Algorithm for Processing Interferometric Data-Stacks: SqueeSAR," *IEEE Trans. Geosci. Remote Sens.*, vol. 49, no. 9, pp. 3460–3470, Sep. 2011, doi: 10.1109/TGRS.2011.2124465.

[47]   G. Fornaro, S. Verde, D. Reale, and A. Pauciullo, "CAESAR: An Approach Based on Covariance Matrix Decomposition to Improve Multibaseline–Multitemporal Interferometric SAR Processing," *IEEE Trans. Geosci. Remote Sens.*, vol. 53, no. 4, pp. 2050–2065, Apr. 2015, doi: 10.1109/TGRS.2014.2352853.

[48]   A. M. Guarnieri and S. Tebaldini, "Hybrid CramÉr–Rao Bounds for Crustal Displacement Field Estimators in SAR Interferometry," *IEEE Signal Process. Lett.*, vol. 14, no. 12, pp. 1012–1015, Dec. 2007, doi: 10.1109/LSP.2007.904705.

[49]   H. Ansari, F. De Zan, and R. Bamler, "Efficient Phase Estimation for Interferogram Stacks," *IEEE Trans. Geosci. Remote Sens.*, vol. 56, no. 7, pp. 4109–4125, Jul. 2018, doi: 10.1109/TGRS.2018.2826045.

[50]   S. Samiei-Esfahany, J. E. Martins, F. van Leijen, and R. F. Hanssen, "Phase Estimation for Distributed Scatterers in InSAR Stacks Using Integer Least Squares Estimation," *IEEE Trans. Geosci. Remote Sens.*, vol. 54, no. 10, pp. 5671–5687, Oct. 2016, doi: 10.1109/TGRS.2016.2566604.

[51]   M. Even and K. Schulz, "InSAR Deformation Analysis with Distributed Scatterers: A Review Complemented by New Advances," *Remote Sens.*, vol. 10, no. 5, p. 744, May 2018, doi: 10.3390/rs10050744.

[52]   M. C. Garthwaite, V. L. Miller, S. Saunders, M. M. Parks, G. Hu, and A. L. Parker, "A Simplified Approach to Operational InSAR Monitoring of Volcano Deformation in Low- and Middle-Income Countries: Case Study of Rabaul Caldera, Papua New Guinea," *Front. Earth Sci.*, vol. 6, no. January, Jan. 2019, doi: 10.3389/feart.2018.00240.

[53]   M. E. Pritchard *et al.*, "Towards coordinated regional multi-satellite InSAR volcano observations: results from the Latin America pilot project," *J. Appl. Volcanol.*, vol. 7, no. 1, p. 5, Dec. 2018, doi: 10.1186/s13617-018-0074-0.

[54]   P. Rosen, E. Gurrola, G. F. Sacco, and H. Zebker, "The InSAR Computing Environment," in *EUSAR 2012; 9th European Conference on Synthetic Aperture Radar*, 2012, pp. 730–733, [Online]. Available: http://medcontent.metapress.com/index/A65RM03P4874243N.pdf.

[55]   A. Pepe and R. Lanari, "On the Extension of the Minimum Cost Flow Algorithm for Phase Unwrapping of Multitemporal Differential SAR Interferograms," *IEEE Trans. Geosci. Remote*

Sens., vol. 44, no. 9, pp. 2374–2383, Sep. 2006, doi: 10.1109/TGRS.2006.873207.

[56]   D. Perissin and T. Wang, "Repeat-Pass SAR Interferometry With Partially Coherent Targets," *IEEE Trans. Geosci. Remote Sens.*, vol. 50, no. 1, pp. 271–280, Jan. 2012, doi: 10.1109/TGRS.2011.2160644.

[57]   A. Pepe, Y. Yang, M. Manzo, and R. Lanari, "Improved EMCF-SBAS Processing Chain Based on Advanced Techniques for the Noise-Filtering and Selection of Small Baseline Multi-Look DInSAR Interferograms," *IEEE Trans. Geosci. Remote Sens.*, vol. 53, no. 8, pp. 4394–4417, Aug. 2015, doi: 10.1109/TGRS.2015.2396875.

[58]   R. Tough, D. Blacknell, and S. Quegan, "A statistical description of polarimetric and interferometric synthetic aperture radar data," *Proc. R. Soc. London. Ser. A Math. Phys. Sci.*, vol. 449, no. 1937, pp. 567–589, Jun. 1995, doi: 10.1098/rspa.1995.0059.

[59]   M. S. Seymour and I. G. Cumming, "Maximum likelihood estimation for SAR interferometry," in *Proceedings of IGARSS '94 - 1994 IEEE International Geoscience and Remote Sensing Symposium*, vol. 4, pp. 2272–2275 vol.4.

[60]   R. B. Lohman and M. Simons, "Some thoughts on the use of InSAR data to constrain models of surface deformation: Noise structure and data downsampling," *Geochemistry, Geophys. Geosystems*, vol. 6, no. 1, Jan. 2005, doi: 10.1029/2004GC000841.

[61]   R. Jolivet *et al.*, "Shallow creep on the Haiyuan Fault (Gansu, China) revealed by SAR Interferometry," *J. Geophys. Res. Solid Earth*, vol. 117, no. B6, Jun. 2012, doi: 10.1029/2011JB008732.

[62]   R. Jolivet, R. Grandin, C. Lasserre, M.-P. Doin, and G. Peltzer, "Systematic InSAR tropospheric phase delay corrections from global meteorological reanalysis data," *Geophys. Res. Lett.*, vol. 38, no. 17, Sep. 2011, doi: 10.1029/2011GL048757.

[63]   M.-P. Doin, C. Lasserre, G. Peltzer, O. Cavalié, and C. Doubre, "Corrections of stratified tropospheric delays in SAR interferometry: Validation with global atmospheric models," *J. Appl. Geophys.*, vol. 69, no. 1, pp. 35–50, Sep. 2009, doi: 10.1016/j.jappgeo.2009.03.010.

[64]   E. A. Hetland, P. Musé, M. Simons, Y. N. Lin, P. S. Agram, and C. J. DiCaprio, "Multiscale InSAR Time Series (MInTS) analysis of surface deformation," *J. Geophys. Res. Solid Earth*, vol. 117, no. B2, Feb. 2012, doi: 10.1029/2011JB008731.

[65]   A. Hooper, "A multi-temporal InSAR method incorporating both persistent scatterer and small baseline approaches," *Geophys. Res. Lett.*, vol. 35, no. 16, p. L16302, Aug. 2008, doi: 10.1029/2008GL034654.

[66]   C. Loupasakis, V. Angelitsa, D. Rozos, and N. Spanou, "Mining geohazards—land subsidence caused by the dewatering of opencast coal mines: The case study of the Amyntaio coal mine, Florina,

Greece," *Nat. Hazards*, vol. 70, no. 1, pp. 675–691, Jan. 2014, doi: 10.1007/s11069-013-0837-1.

[67]   D. Raucoules, C. Colesanti, and C. Carnec, "Use of SAR interferometry for detecting and assessing ground subsidence," *Comptes Rendus - Geosci.*, vol. 339, no. 5, pp. 289–302, Apr. 2007, doi: 10.1016/j.crte.2007.02.002.

[68]   H. S. Jung, Z. Lu, J. S. Won, M. P. Poland, and A. Miklius, "Mapping Three-Dimensional Surface Deformation by Combining Multiple-Aperture Interferometry and Conventional Interferometry: Application to the June 2007 Eruption of Kilauea Volcano, Hawaii," *IEEE Geosci. Remote Sens. Lett.*, vol. 8, no. 1, pp. 34–38, Jan. 2011, doi: 10.1109/LGRS.2010.2051793.

[69]   H. Yue, "Coal mining induced land subsidence monitoring using multiband spaceborne differential interferometric synthetic aperture radar data," *J. Appl. Remote Sens.*, vol. 5, no. 1, p. 053518, Jan. 2011, doi: 10.1117/1.3571038.

[70]   D. Liu *et al.*, "Evaluation of InSAR and TomoSAR for Monitoring Deformations Caused by Mining in a Mountainous Area with High Resolution Satellite-Based SAR," *Remote Sens.*, vol. 6, no. 2, pp. 1476–1495, Feb. 2014, doi: 10.3390/rs6021476.

[71]   T. J. Wright, "Toward mapping surface deformation in three dimensions using InSAR," *Geophys. Res. Lett.*, vol. 31, no. 1, p. L01607, 2004, doi: 10.1029/2003GL018827.

[72]   J. Hu, Z. Li, J. Zhu, X. Ren, and X. Ding, "Inferring three-dimensional surface displacement field by combining SAR interferometric phase and amplitude information of ascending and descending orbits," *Sci. China Earth Sci.*, vol. 53, no. 4, pp. 550–560, Apr. 2010, doi: 10.1007/s11430-010-0023-1.

[73]   Z. Yang *et al.*, "Time-Series 3-D Mining-Induced Large Displacement Modeling and Robust Estimation from a Single-Geometry SAR Amplitude Data Set," *IEEE Trans. Geosci. Remote Sens.*, vol. 56, no. 6, pp. 3600–3610, 2018, doi: 10.1109/TGRS.2018.2802919.

[74]   J. Hu, Z. W. Li, X. L. Ding, J. J. Zhu, L. Zhang, and Q. Sun, "3D coseismic Displacement of 2010 Darfield, New Zealand earthquake estimated from multi-aperture InSAR and D-InSAR measurements," *J. Geod.*, vol. 86, no. 11, pp. 1029–1041, 2012, doi: 10.1007/s00190-012-0563-6.

[75]   J. Hu, Z. W. Li, X. L. Ding, J. J. Zhu, L. Zhang, and Q. Sun, "Resolving three-dimensional surface displacements from InSAR measurements: A review," *Earth-Science Rev.*, vol. 133, pp. 1–17, Jun. 2014, doi: 10.1016/j.earscirev.2014.02.005.

[76]   P. Bally, "Satellite earth observation for geohazard risk management," 2012. doi: 10.5270/esa-geo-hzrd-2012.

[77]   W. R. Paradella *et al.*, "Mapping surface deformation in open pit iron mines of Carajás Province (Amazon Region) using an integrated SAR analysis," *Eng. Geol.*, vol. 193, pp. 61–78, Jul. 2015, doi: 10.1016/j.enggeo.2015.04.015.

[78]   A. Pepe and F. Calò, "A Review of Interferometric Synthetic Aperture RADAR (InSAR) Multi-Track Approaches for the Retrieval of Earth's Surface Displacements," *Appl. Sci.*, vol. 7, no. 12, p. 1264, Dec. 2017, doi: 10.3390/app7121264.

[79]   X. Wang, A. Mueen, H. Ding, G. Trajcevski, P. Scheuermann, and E. Keogh, "Experimental comparison of representation methods and distance measures for time series data," *Data Min. Knowl. Discov.*, vol. 26, no. 2, pp. 275–309, Mar. 2013, doi: 10.1007/s10618-012-0250-5.

[80]   H. Sakoe and S. Chiba, "Dynamic programming algorithm optimization for spoken word recognition," *IEEE Trans. Acoust.*, vol. 26, no. 1, pp. 43–49, Feb. 1978, doi: 10.1109/TASSP.1978.1163055.

[81]   "European Union, Copernicus Land Monitoring Service, European Environment Agency (EEA)." https://land.copernicus.eu/pan-european/corine-land-cover (accessed Oct. 01, 2022).

[82]   F. Sica, A. Pulella, M. Nannini, M. Pinheiro, and P. Rizzoli, "Repeat-pass SAR interferometry for land cover classification: A methodology using Sentinel-1 Short-Time-Series," *Remote Sens. Environ.*, vol. 232, no. November 2018, p. 111277, Oct. 2019, doi: 10.1016/j.rse.2019.111277.

[83]   H.-W. Yun, J.-R. Kim, Y.-S. Choi, and S.-Y. Lin, "Analyses of Time Series InSAR Signatures for Land Cover Classification: Case Studies over Dense Forestry Areas with L-Band SAR Images," *Sensors*, vol. 19, no. 12, p. 2830, Jun. 2019, doi: 10.3390/s19122830.

[84]   S. Plank, J. Singer, and K. Thuro, "Persistent scatterer estimation using optical remote sensing data, land cover data and topographical maps," in *2012 IEEE International Geoscience and Remote Sensing Symposium*, pp. 3855–3858, doi: 10.1109/IGARSS.2012.6350571.

[85]   O. S. D. of L. G. Prokos, Anthony (Public Power Cooperation S.A, "Athens, Greece. Personal communication." Athens, Greece, 2019.

[86]   H. Fattahi, P. Agram, and M. Simons, "A Network-Based Enhanced Spectral Diversity Approach for TOPS Time-Series Analysis," *IEEE Trans. Geosci. Remote Sens.*, vol. 55, no. 2, pp. 777–786, Feb. 2017, doi: 10.1109/TGRS.2016.2614925.

[87]   J. J. Sousa, A. J. Hooper, R. F. Hanssen, L. C. Bastos, and A. M. Ruiz, "Persistent Scatterer InSAR: A comparison of methodologies based on a model of temporal deformation vs. spatial correlation selection criteria," *Remote Sens. Environ.*, vol. 115, no. 10, pp. 2652–2663, Oct. 2011, doi: 10.1016/j.rse.2011.05.021.

[88]   P. S. Agram and M. Simons, "A noise model for InSAR time series," *J. Geophys. Res. Solid Earth*, vol. 120, no. 4, pp. 2752–2771, Apr. 2015, doi: 10.1002/2014JB011271.

[89]   O. Mora, J. J. Mallorqui, and A. Broquetas, "Linear and nonlinear terrain deformation maps from a reduced set of interferometric sar images," *IEEE Trans. Geosci. Remote Sens.*, vol. 41, no. 10, pp. 2243–2253, Oct. 2003, doi: 10.1109/TGRS.2003.814657.

[90]   H. Ansari, F. De Zan, and R. Bamler, "Sequential Estimator: Toward Efficient InSAR Time Series Analysis," *IEEE Trans. Geosci. Remote Sens.*, vol. 55, no. 10, pp. 5637–5652, Oct. 2017, doi: 10.1109/TGRS.2017.2711037.

[91]   B. Wang, C. Zhao, Q. Zhang, Z. Lu, Z. Li, and Y. Liu, "Sequential Estimation of Dynamic Deformation Parameters for SBAS-InSAR," *IEEE Geosci. Remote Sens. Lett.*, pp. 1–5, 2019, doi: 10.1109/LGRS.2019.2938330.

[92]   M. Crosetto, O. Monserrat, M. Cuevas-González, N. Devanthéry, and B. Crippa, "Persistent Scatterer Interferometry: A review," *ISPRS J. Photogramm. Remote Sens.*, vol. 115, pp. 78–89, May 2016, doi: 10.1016/j.isprsjprs.2015.10.011.

[93]   J. R. Sabater, J. Duro, A. Arnaud, D. Albiol, and F. N. Koudogbo, "Comparative analyses of multifrequency PSI ground deformation measurements," in *SAR Image Analysis, Modeling, and Techniques XI*, 2011, vol. 8179, no. January, p. 81790M, doi: 10.1117/12.898916.

[94]   T. Zhang, W. Bin Shen, W. Wu, B. Zhang, and Y. Pan, "Recent surface deformation in the Tianjin area revealed by Sentinel-1A data," *Remote Sens.*, vol. 11, no. 2, pp. 1–25, 2019, doi: 10.3390/rs11020130.

[95]   "Advanced Rapid Imaging and Analysis (ARIA) Project for Natural Hazards." https://aria.jpl.nasa.gov/ (accessed Sep. 30, 2022).

[96]   "COMET-LiCS Sentinel-1 InSAR portal." https://comet.nerc.ac.uk/comet-lics-portal/ (accessed Mar. 25, 2020).

[97]   Y. Morishita, M. Lazecky, T. J. Wright, J. R. Weiss, J. R. Elliott, and A. Hooper, "LiCSBAS: An Open-Source InSAR Time Series Analysis Package Integrated with the LiCSAR Automated Sentinel-1 InSAR Processor," *Remote Sens.*, vol. 12, no. 3, p. 424, Jan. 2020, doi: 10.3390/rs12030424.

[98]   A. Burnol *et al.*, "Wavelet-based analysis of ground deformation coupling satellite acquisitions (Sentinel-1, SMOS) and data from shallow and deep wells in Southwestern France," *Sci. Rep.*, vol. 9, no. 1, p. 8812, Dec. 2019, doi: 10.1038/s41598-019-45302-z.

[99]   L. van der Maaten and G. Hinton, "Visualizing Data using t-SNE," *J. Mach. Learn. Res.*, vol. 9, pp. 2579–2605, 2008, [Online]. Available: http://www.jmlr.org/papers/v9/vandermaaten08a.html.

[100] F. Pedregosa *et al.*, "Scikit-learn: Machine Learning in Python," *J. Mach. Learn. Res.*, vol. 12, pp. 2825–2830, 2011.

[101] L. McInnes, J. Healy, and S. Astels, "hdbscan: Hierarchical density based clustering," *J. Open Source Softw.*, vol. 2, no. 11, p. 205, Mar. 2017, doi: 10.21105/joss.00205.

[102] A. Grinsted, J. C. Moore, and S. Jevrejeva, "Application of the cross wavelet transform and wavelet coherence to geophysical time series," *Nonlinear Process. Geophys.*, vol. 11, no. 5/6, pp. 561–566,

Nov. 2004, doi: 10.5194/npg-11-561-2004.

[103] K. Karamvasis, "Exploring Driving Factors Of Ground Deformation Using Wavelet Analysis Case Study Of Kastoria Lake," 2021. https://www.youtube.com/watch?v=zt2IjzAjbx4 (accessed Oct. 25, 2022).

[104] A. Grinsted, "Cross Wavelet and Wavelet Coherence Toolbox." https://grinsted.github.io/wavelet-coherence/ (accessed Oct. 25, 2022).

[105] C. Gianneli, K. Voudouris, and G. Soulios, "Water resources in Korisos basin, NW Greece: interactions between surface and ground water," *Int. J. Water*, vol. 6, no. 1/2, p. 57, 2011, doi: 10.1504/IJW.2011.043317.

[106] J. Dong *et al.*, "Mapping landslide surface displacements with time series SAR interferometry by combining persistent and distributed scatterers: A case study of Jiaju landslide in Danba, China," *Remote Sens. Environ.*, vol. 205, no. August 2017, pp. 180–198, 2018, doi: 10.1016/j.rse.2017.11.022.

[107] A. Hooper, D. Bekaert, K. Spaans, E. Hussain, and M. Arikan, "StaMPS - Stanford Method for Persistent Scatterers," 2014. https://github.com/dbekaert/StaMPS (accessed Oct. 29, 2022).

[108] C. C. Aggarwal, Y. Zhao, and P. S. Yu, "Outlier detection in graph streams," in *2011 IEEE 27th International Conference on Data Engineering*, 2011, pp. 399–409, doi: 10.1109/ICDE.2011.5767885.

[109] A. Berg and J. Sheffield, "Climate Change and Drought: the Soil Moisture Perspective," *Curr. Clim. Chang. Reports*, vol. 4, no. 2, pp. 180–191, Jun. 2018, doi: 10.1007/s40641-018-0095-0.

[110] A. Srivastava, P. M. Saco, J. F. Rodriguez, N. Kumari, K. P. Chun, and O. Yetemen, "The role of landscape morphology on soil moisture variability in semi-arid ecosystems," *Hydrol. Process.*, vol. 35, no. 1, pp. 0–3, Jan. 2021, doi: 10.1002/hyp.13990.

[111] T. E. Jordan *et al.*, "Surface materials and landforms as controls on InSAR permanent and transient responses to precipitation events in a hyperarid desert, Chile," *Remote Sens. Environ.*, vol. 237, no. August 2019, p. 111544, Feb. 2020, doi: 10.1016/j.rse.2019.111544.

[112] Q. Gao, M. Zribi, M. Escorihuela, and N. Baghdadi, "Synergetic Use of Sentinel-1 and Sentinel-2 Data for Soil Moisture Mapping at 100 m Resolution," *Sensors*, vol. 17, no. 9, p. 1966, Aug. 2017, doi: 10.3390/s17091966.

[113] A. Balenzano *et al.*, "Sentinel-1 soil moisture at 1 km resolution: a validation study," *Remote Sens. Environ.*, vol. 263, no. December 2020, p. 112554, Sep. 2021, doi: 10.1016/j.rse.2021.112554.

[114] J. Peng *et al.*, "A roadmap for high-resolution satellite soil moisture applications – confronting product characteristics with user requirements," *Remote Sens. Environ.*, vol. 252, p. 112162, Jan. 2021, doi: 10.1016/j.rse.2020.112162.

[115] P. M. Bürgi and R. B. Lohman, "High-Resolution Soil Moisture Evolution in Hyper-Arid Regions: A Comparison of InSAR, SAR, Microwave, Optical, and Data Assimilation Systems in the Southern Arabian Peninsula," *J. Geophys. Res. Earth Surf.*, vol. 126, no. 12, pp. 1–16, 2021, doi: 10.1029/2021JF006158.

[116] S. Ranjbar, M. Akhoondzadeh, B. Brisco, M. Amani, and M. Hosseini, "Soil Moisture Change Monitoring from C and L-band SAR Interferometric Phase Observations," *IEEE J. Sel. Top. Appl. Earth Obs. Remote Sens.*, vol. 14, pp. 7179–7197, 2021, doi: 10.1109/JSTARS.2021.3096063.

[117] N. C. Mira, J. Catalao, G. Nico, and P. Mateus, "Soil Moisture Estimation Using Atmospherically Corrected C-Band InSAR Data," *IEEE Trans. Geosci. Remote Sens.*, vol. 60, pp. 1–9, 2022, doi: 10.1109/TGRS.2021.3109450.

[118] S. Zwieback, S. Hensley, and I. Hajnsek, "Soil Moisture Estimation Using Differential Radar Interferometry: Toward Separating Soil Moisture and Displacements," *IEEE Trans. Geosci. Remote Sens.*, vol. 55, no. 9, pp. 5069–5083, Sep. 2017, doi: 10.1109/TGRS.2017.2702099.

[119] F. De Zan, A. Parizzi, P. Prats-Iraola, and P. Lopez-Dekker, "A SAR Interferometric Model for Soil Moisture," *IEEE Trans. Geosci. Remote Sens.*, vol. 52, no. 1, pp. 418–425, Jan. 2014, doi: 10.1109/TGRS.2013.2241069.

[120] S. Zwieback, S. Hensley, and I. Hajnsek, "Assessment of soil moisture effects on L-band radar interferometry," *Remote Sens. Environ.*, vol. 164, pp. 77–89, 2015, doi: 10.1016/j.rse.2015.04.012.

[121] F. De Zan and G. Gomba, "Vegetation and soil moisture inversion from SAR closure phases: First experiments and results," *Remote Sens. Environ.*, vol. 217, no. March, pp. 562–572, Nov. 2018, doi: 10.1016/j.rse.2018.08.034.

[122] R. J. Michaelides, "Quantifying Permafrost Processes and Soil Moisture with Interferometric Phase and Closure Phase," Stanford University, 2020.

[123] C. P. Scott, R. B. Lohman, and T. E. Jordan, "InSAR constraints on soil moisture evolution after the March 2015 extreme precipitation event in Chile," *Sci. Rep.*, vol. 7, no. 1, p. 4903, Dec. 2017, doi: 10.1038/s41598-017-05123-4.

[124] Y. Shao, K. Fraedrich, and M. Ishizuka, "Modelling Soil Moisture in Hyper-Arid Conditions," *Boundary-Layer Meteorol.*, vol. 179, no. 2, pp. 169–186, 2021, doi: 10.1007/s10546-020-00596-9.

[125] H. A. Zebker and J. Villasenor, "Decorrelation in interferometric radar echoes," *IEEE Trans. Geosci. Remote Sens.*, vol. 30, no. 5, pp. 950–959, 1992, doi: 10.1109/36.175330.

[126] A. K. Hoskera, G. Nico, M. Irshad Ahmed, and A. Whitbread, "Accuracies of Soil Moisture Estimations Using a Semi-Empirical Model over Bare Soil Agricultural Croplands from Sentinel-1 SAR Data," *Remote Sens.*, vol. 12, no. 10, p. 1664, May 2020, doi: 10.3390/rs12101664.

[127] Y. Morishita and R. F. Hanssen, "Temporal Decorrelation in L-, C-, and X-band Satellite Radar

Interferometry for Pasture on Drained Peat Soils," *IEEE Trans. Geosci. Remote Sens.*, vol. 53, no. 2, pp. 1096–1104, Feb. 2015, doi: 10.1109/TGRS.2014.2333814.

[128]   M. Hallikainen, F. Ulaby, M. Dobson, M. El-rayes, and L. Wu, "Microwave Dielectric Behavior of Wet Soil-Part 1: Empirical Models and Experimental Observations," *IEEE Trans. Geosci. Remote Sens.*, vol. GE-23, no. 1, pp. 25–34, Jan. 1985, doi: 10.1109/TGRS.1985.289497.

[129]   "Optimization   and   Root   Finding,"   2022. https://docs.scipy.org/doc/scipy/reference/optimize.minimize-slsqp.html (accessed Aug. 31, 2022).

[130]   D. Coppernoll-Houston and C. Potter, "Field Measurements and Satellite Remote Sensing of Daily Soil Surface Temperature Variations in the Lower Colorado Desert of California," *Climate*, vol. 6, no. 4, p. 94, Nov. 2018, doi: 10.3390/cli6040094.

[131]   H. West, N. Quinn, M. Horswell, and P. White, "Assessing Vegetation Response to Soil Moisture Fluctuation under Extreme Drought Using Sentinel-2," *Water*, vol. 10, no. 7, p. 838, Jun. 2018, doi: 10.3390/w10070838.

[132]   J. Muñoz-Sabater *et al.*, "ERA5-Land: a state-of-the-art global reanalysis dataset for land applications," *Earth Syst. Sci. Data*, vol. 13, no. 9, pp. 4349–4383, Sep. 2021, doi: 10.5194/essd-13-4349-2021.

[133]   N. C. Mira, J. Catalão, G. Nico, A. Militar, A. Conde, and C. Guimarães, "Soil Moisture Variation Impact on Decorrelation Phase Estimated By Sentinel-1 Insar Data," in *IGARSS 2022-2022 IEEE International Geoscience and Remote Sensing Symposium*, 2022, no. 1, pp. 5792–5795.

[134]   G. L. Schaefer, M. H. Cosh, and T. J. Jackson, "The USDA Natural Resources Conservation Service Soil Climate Analysis Network (SCAN)," *J. Atmos. Ocean. Technol.*, vol. 24, no. 12, pp. 2073–2077, Dec. 2007, doi: 10.1175/2007JTECHA930.1.

[135]   W. A. Dorigo *et al.*, "The International Soil Moisture Network: a data hosting facility for global in situ soil moisture measurements," *Hydrol. Earth Syst. Sci.*, vol. 15, no. 5, pp. 1675–1698, May 2011, doi: 10.5194/hess-15-1675-2011.

[136]   W. Dorigo *et al.*, "The International Soil Moisture Network: serving Earth system science for over a decade," *Hydrol. Earth Syst. Sci.*, vol. 25, no. 11, pp. 5749–5804, Nov. 2021, doi: 10.5194/hess-25-5749-2021.

[137]   J. M. Costa-Saura, Á. Balaguer-Beser, L. A. Ruiz, J. E. Pardo-Pascual, and J. L. Soriano-Sancho, "Empirical Models for Spatio-Temporal Live Fuel Moisture Content Estimation in Mixed Mediterranean Vegetation Areas Using Sentinel-2 Indices and Meteorological Data," *Remote Sens.*, vol. 13, no. 18, p. 3726, Sep. 2021, doi: 10.3390/rs13183726.

[138]   B. Liu and T. J. Coulthard, "Mapping the interactions between rivers and sand dunes: Implications for fluvial and aeolian geomorphology," *Geomorphology*, vol. 231, pp. 246–257, 2015, doi:

10.1016/j.geomorph.2014.12.011.

[139] F. Arenas-Díaz *et al.*, "Dust and aerosols in the Atacama Desert," *Earth-Science Rev.*, vol. 226, no. February 2021, p. 103925, Mar. 2022, doi: 10.1016/j.earscirev.2022.103925.

[140] T. Hengl *et al.*, "SoilGrids250m: Global gridded soil information based on machine learning," *PLoS One*, vol. 12, no. 2, p. e0169748, Feb. 2017, doi: 10.1371/journal.pone.0169748.

[141] D. Palmisano, G. Satalino, A. Balenzano, and F. Mattia, "Coherent and Incoherent Change Detection for Soil Moisture Retrieval From Sentinel-1 Data," *IEEE Geosci. Remote Sens. Lett.*, vol. 19, no. c, pp. 1–5, 2022, doi: 10.1109/LGRS.2022.3154631.

[142] Z. Chen *et al.*, "InSAR Monitoring of Arctic Landfast Sea Ice Deformation Using L-Band ALOS-2, C-Band Radarsat-2 and Sentinel-1," *Remote Sens.*, vol. 13, no. 22, p. 4570, Nov. 2021, doi: 10.3390/rs13224570.

[143] M. Wei and D. T. Sandwell, "Decorrelation of L-band and C-band interferometry over vegetated areas in California," *IEEE Trans. Geosci. Remote Sens.*, vol. 48, no. 7, pp. 2942–2952, 2010, doi: 10.1109/TGRS.2010.2043442.

[144] R. Hakimdavar *et al.*, "Monitoring water-related ecosystems with earth observation data in support of Sustainable Development Goal (SDG) 6 reporting," *Remote Sens.*, vol. 12, no. 10, 2020, doi: 10.3390/rs12101634.

[145] L. Alfieri, L. Feyen, and G. Di Baldassarre, "Increasing flood risk under climate change: a pan-European assessment of the benefits of four adaptation strategies," *Clim. Change*, vol. 136, no. 3–4, pp. 507–521, 2016, doi: 10.1007/s10584-016-1641-1.

[146] F. Cian, M. Marconcini, and P. Ceccato, "Normalized Difference Flood Index for rapid flood mapping: Taking advantage of EO big data," *Remote Sens. Environ.*, vol. 209, no. February, pp. 712–730, 2018, doi: 10.1016/j.rse.2018.03.006.

[147] C. Di Mauro *et al.*, "Assimilation of probabilistic flood maps from SAR data into a coupled hydrologic--hydraulic forecasting model: a proof of concept," *Hydrol. Earth Syst. Sci.*, vol. 25, no. 7, pp. 4081–4097, 2021, doi: 10.5194/hess-25-4081-2021.

[148] D. C. Alberto Refice, Annarita D'Addabbo, *Springer Remote Sensing/Photogrammetry*. 2018.

[149] L. Cenci *et al.*, "An evaluation of the potential of Sentinel 1 for improving flash flood predictions via soil moisture-data assimilation," *Adv. Geosci.*, vol. 44, pp. 89–100, 2017, doi: 10.5194/adgeo-44-89-2017.

[150] X. Tong *et al.*, "An approach for flood monitoring by the combined use of Landsat 8 optical imagery and COSMO-SkyMed radar imagery," *ISPRS J. Photogramm. Remote Sens.*, vol. 136, no. February, pp. 144–153, 2018, doi: 10.1016/j.isprsjprs.2017.11.006.

[151] S. I. Khan *et al.*, "Satellite remote sensing and hydrologic modeling for flood inundation mapping

in lake victoria basin: Implications for hydrologic prediction in ungauged basins," *IEEE Trans. Geosci. Remote Sens.*, vol. 49, no. 1 PART 1, pp. 85–95, 2011, doi: 10.1109/TGRS.2010.2057513.

[152]   L. Giustarini, R. Hostache, P. Matgen, G. J. P. Schumann, P. D. Bates, and D. C. Mason, "A change detection approach to flood mapping in Urban areas using TerraSAR-X," *IEEE Trans. Geosci. Remote Sens.*, vol. 51, no. 4, pp. 2417–2430, 2013, doi: 10.1109/TGRS.2012.2210901.

[153]   A. Twele, W. Cao, S. Plank, and S. Martinis, "Sentinel-1-based flood mapping: a fully automated processing chain," *Int. J. Remote Sens.*, vol. 37, no. 13, pp. 2990–3004, 2016, doi: 10.1080/01431161.2016.1192304.

[154]   R. Manavalan, "SAR image analysis techniques for flood area mapping - literature survey," *Earth Sci. Informatics*, vol. 10, no. 1, 2017, doi: 10.1007/s12145-016-0274-2.

[155]   D. Bonafilia, B. Tellman, T. Anderson, and E. Issenberg, "Sen1Floods11: A georeferenced dataset to train and test deep learning flood algorithms for sentinel-1," *IEEE Comput. Soc. Conf. Comput. Vis. Pattern Recognit. Work.*, vol. 2020-June, pp. 835–845, 2020, doi: 10.1109/CVPRW50498.2020.00113.

[156]   D. Amitrano *et al.*, "Modeling watershed response in semiarid regions with high-resolution synthetic aperture radars," *IEEE J. Sel. Top. Appl. Earth Obs. Remote Sens.*, vol. 7, no. 7, pp. 2732–2745, 2014, doi: 10.1109/JSTARS.2014.2313230.

[157]   H. Cao, H. Zhang, C. Wang, and B. Zhang, "Operational flood detection using Sentinel-1 SAR data over large areas," *Water (Switzerland)*, vol. 11, no. 4, 2019, doi: 10.3390/w11040786.

[158]   M. Chini, R. Hostache, L. Giustarini, and P. Matgen, "A hierarchical split-based approach for parametric thresholding of SAR images: Flood inundation as a test case," *IEEE Trans. Geosci. Remote Sens.*, vol. 55, no. 12, pp. 6975–6988, 2017, doi: 10.1109/TGRS.2017.2737664.

[159]   B. Brisco, "Early Applications of Remote Sensing for Mapping Wetlands," in *Remote Sensing of Wetlands*, no. August, Boca Raton: CRC Press, 2015, pp. 86–97.

[160]   S. Martinis, S. Plank, and K. Ćwik, "The use of Sentinel-1 time-series data to improve flood monitoring in arid areas," *Remote Sens.*, vol. 10, no. 4, 2018, doi: 10.3390/rs10040583.

[161]   D. Amitrano, G. Di Martino, A. Iodice, D. Riccio, and G. Ruello, "Unsupervised Rapid Flood Mapping Using Sentinel-1 GRD SAR Images," *IEEE Trans. Geosci. Remote Sens.*, vol. 56, no. 6, pp. 3290–3299, 2018, doi: 10.1109/TGRS.2018.2797536.

[162]   B. DeVries, C. Huang, J. Armston, W. Huang, J. W. Jones, and M. W. Lang, "Rapid and robust monitoring of flood events using Sentinel-1 and Landsat data on the Google Earth Engine," *Remote Sens. Environ.*, vol. 240, no. August 2019, p. 111664, 2020, doi: 10.1016/j.rse.2020.111664.

[163]   P. Matgen, R. Hostache, G. Schumann, L. Pfister, L. Hoffmann, and H. H. G. Savenije, "Towards an automated SAR-based flood monitoring system: Lessons learned from two case studies," *Phys.*

Chem. Earth, vol. 36, no. 7–8, pp. 241–252, 2011, doi: 10.1016/j.pce.2010.12.009.

[164]   K. Karamvasis and V. Karathanassi, "FLOMPY: An Open-Source Toolbox for Floodwater Mapping Using Sentinel-1 Intensity Time Series," *Water*, vol. 13, no. 21, p. 2943, Oct. 2021, doi: 10.3390/w13212943.

[165]   K. Karamvasis, "Flood Mapping Python Toolbox (FLOMPY)," 2021. https://github.com/kleok/FLOMPY (accessed Oct. 10, 2022).

[166]   "ESA - Sentinel Application Platform (SNAP)." https://step.esa.int/main/toolboxes/snap/ (accessed Oct. 01, 2022).

[167]   F. Filipponi, "Sentinel-1 GRD Preprocessing Workflow," *Proceedings*, vol. 18, no. 1, p. 11, Jun. 2019, doi: 10.3390/ECRS-3-06201.

[168]   G. Kaplan, L. Fine, V. Lukyanov, V. S. Manivasagam, J. Tanny, and O. Rozenstein, "Normalizing the Local Incidence Angle in Sentinel-1 Imagery to Improve Leaf Area Index, Vegetation Height, and Crop Coefficient Estimations," *Land*, vol. 10, no. 7, p. 680, Jun. 2021, doi: 10.3390/land10070680.

[169]   J. Xue and Y. Zhang, "Ridler and Calvard's, Kittler and Illingworth's and Otsu's methods for image thresholding," *Pattern Recognit. Lett.*, vol. 33, no. 6, pp. 793–797, Apr. 2012, doi: 10.1016/j.patrec.2012.01.002.

[170]   L. Landuyt, A. Van Wesemael, G. J. P. Schumann, R. Hostache, N. E. C. Verhoest, and F. M. B. Van Coillie, "Flood Mapping Based on Synthetic Aperture Radar: An Assessment of Established Approaches," *IEEE Trans. Geosci. Remote Sens.*, vol. 57, no. 2, pp. 722–739, 2019, doi: 10.1109/TGRS.2018.2860054.

[171]   J. B. Freeman and R. Dale, "Assessing bimodality to detect the presence of a dual cognitive process," *Behav. Res. Methods*, vol. 45, no. 1, pp. 83–97, Mar. 2013, doi: 10.3758/s13428-012-0225-x.

[172]   J. Kittler and J. Illingworth, "Minimum error thresholding," *Pattern Recognit.*, vol. 19, no. 1, pp. 41–47, Jan. 1986, doi: 10.1016/0031-3203(86)90030-0.

[173]   P. K. Sahoo, S. Soltani, and A. K. C. Wong, "A survey of thresholding techniques," *Comput. Vision, Graph. Image Process.*, vol. 41, no. 2, pp. 233–260, 1988, doi: https://doi.org/10.1016/0734-189X(88)90022-9.

[174]   N. Otsu, "A threshold selection method from gray-level histograms," *IEEE Trans. Syst. Man. Cybern.*, vol. 9, no. 1, pp. 62–66, 1979.

[175]   V. W. Berger and Y. Zhou, "Kolmogorov–Smirnov Test: Overview," in *Wiley StatsRef: Statistics Reference Online*, Atlanta, GA, USA: Wiley, 2014.

[176]   S. J. Kim, A. Magnani, and S. P. Boyd, "Robust Fisher discriminant analysis," *Adv. Neural Inf. Process. Syst.*, vol. 1, pp. 659–666, 2005.

[177] R.   Davies,   "Greece—Evacuations   after   Floods   in   Thessaly,"   2018. http://floodlist.com/europe/greece-floods-thessaly-february-march-2018 (accessed Jun. 21, 2021).

[178] I. Zotou, V. Bellos, A. Gkouma, V. Karathanassi, and V. A. Tsihrintzis, "Using Sentinel-1 Imagery to Assess Predictive Performance of a Hydraulic Model," *Water Resour. Manag.*, vol. 34, no. 14, pp. 4415–4430, 2020, doi: 10.1007/s11269-020-02592-7.

[179] "COPERNICUS Emergency Management Service - Mapping, EMSR271: Floods in Central Greece." https://emergency.copernicus.eu/mapping/list-of-components/EMSR271 (accessed Oct. 10, 2022).

[180] G. Papaioannou *et al.*, "A Flood Inundation Modeling Approach for Urban and Rural Areas in Lake and Large-Scale River Basins," *Water*, vol. 13, no. 9, p. 1264, Apr. 2021, doi: 10.3390/w13091264.

[181] G. D. Bathrellos, H. D. Skilodimou, K. Soukis, and E. Koskeridou, "Temporal and spatial analysis of flood occurrences in the drainage basin of Pinios River (Thessaly, Central Greece)," *Land*, vol. 7, no. 3, pp. 1–18, 2018, doi: 10.3390/land7030106.

[182] "Maximum   floodwater   depth   at   50-year   time." https://floods.ypeka.gr/index.php?option=com_content&view=article&id=225&Itemid=710 (accessed Oct. 05, 2021).

[183] "Online   Manual   for   EMS   Rapid   Mapping   Products." https://emergency.copernicus.eu/mapping/ems/online-manual-rapid-mapping-products   (accessed Oct. 10, 2022).

[184] G. M. Foody, "Status of land cover classification accuracy assessment," *Remote Sens. Environ.*, vol. 80, no. 1, pp. 185–201, Apr. 2002, doi: 10.1016/S0034-4257(01)00295-4.

[185] "COPERNICUS Emergency Management Service - Mapping, EMSR504: Floods, Australia." https://emergency.copernicus.eu/mapping/list-of-components/EMSR504/ALL/EMSR504_AOI03 (accessed Oct. 10, 2022).

[186] R. Pelich, M. Chini, R. Hostache, P. Matgen, L. Pulvirenti, and N. Pierdicca, "Mapping Floods in Urban Areas From Dual-Polarization InSAR Coherence Data," *IEEE Geosci. Remote Sens. Lett.*, pp. 1–5, 2021, doi: 10.1109/LGRS.2021.3110132.

[187] O. Gounari, A. Falagas, K. Karamvasis, V. Tsironis, V. Karathanassi, and K. Konstantinos, "Floodwater mapping & Extraction of Flood-Affected agricultural Fields," in *Living Planet Symposium 2022 European Space Agency*, 2022.

[188] L. Yan and D. P. Roy, "Automated crop field extraction from multi-temporal Web Enabled Landsat Data," *Remote Sens. Environ.*, vol. 144, pp. 42–64, Mar. 2014, doi: 10.1016/j.rse.2014.01.006.

[189] M. Resing, "Automatic Delineation of Agricultural Fields from Sentinel-2 Images," 2021. https://github.com/resingm/field-boundary-delineation (accessed Oct. 10, 2022).

[190] HEC-RAS, "HEC-RAS River Analysis System Hydraulic Reference Manual," 2016.

[191] I. Zotou, K. Karamvasis, V. Karathanassi, and V. Tsihrintzis, "Sensitivity of a coupled 1D/2D model in input parameter variation exploiting Sentinel-1-derived flood map," in *7th IAHR Europe Congress*, 2022, pp. 247–248.

[192] "Copernicus Emergency Management Service - EMS." https://emergency.copernicus.eu/mapping (accessed Oct. 15, 2022).

[193] M. Barker *et al.*, "Introducing the FAIR Principles for research software," *Sci. Data*, vol. 9, no. 1, p. 622, Oct. 2022, doi: 10.1038/s41597-022-01710-x.

[194] Y. Li, S. Martinis, and M. Wieland, "Urban flood mapping with an active self-learning convolutional neural network based on TerraSAR-X intensity and interferometric coherence," *ISPRS J. Photogramm. Remote Sens.*, vol. 152, no. December 2018, pp. 178–191, Jun. 2019, doi: 10.1016/j.isprsjprs.2019.04.014.

[195] J. Zhao *et al.*, "Urban-Aware U-Net for Large-Scale Urban Flood Mapping Using Multitemporal Sentinel-1 Intensity and Interferometric Coherence," *IEEE Trans. Geosci. Remote Sens.*, vol. 60, pp. 1–21, 2022, doi: 10.1109/tgrs.2022.3199036.

[196] M. Helleis, M. Wieland, C. Krullikowski, S. Martinis, and S. Plank, "Sentinel-1-Based Water and Flood Mapping: Benchmarking Convolutional Neural Networks Against an Operational Rule-Based Processing Chain," *IEEE J. Sel. Top. Appl. Earth Obs. Remote Sens.*, vol. 15, pp. 2023–2036, 2022, doi: 10.1109/JSTARS.2022.3152127.

[197] O. L. Stephenson *et al.*, "Deep Learning-Based Damage Mapping with InSAR Coherence Time Series," *IEEE Trans. Geosci. Remote Sens.*, vol. 60, 2022, doi: 10.1109/TGRS.2021.3084209.

7   LIST OF FIGURES

8   LIST OF TABLES